University of Pardubice

Faculty of Chemical Technology

Department of Inorganic Technology

NMR Spectroscopy of Cations in Extra-framework Sites in Zeolites

Petr Klein

Doctoral Thesis

2018

I hereby confirm that I have written this doctoral thesis independently. All the reference literature and information used in the thesis are quoted in the list of reference literature.
I hereby acknowledge that all the rights and duties resulting from Act N. 121/2000 Sb., the Copyright Act, apply to my written work, especially that the University of Pardubice has the right to make a license agreement of use of this written work as a school work pursuant to § 60 section 1 of the Copyright Act. On the condition that the written work shall be used by me or a license shall be provided to another subject for the use hereof, the University of Pardubice shall have the right to require from me a relevant contribution to reimburse the costs incurred for the making of such work including all relevant costs and total overall expenditure and expenses incurred.

I express my consent with making the work accessible in the University Library.

Dated in Prague on 27th September 2018

Petr Klein

I would like to thank my supervisor Mgr. Jiří Dědeček, CSc., DSc. for his scientific help and support, Dr. Štěpán Sklenák for running quantum chemical calculations and all my colleagues, who helped me with my work. I would like to acknowledge my friend and colleague Ing. Libor Kobera, PhD., for acquisition of ultra-high field NMR spectra and his help with experimental settings. My thanks go to Dr. Jiří Brus, head of the Joint laboratory of solid-state NMR, for his advices and fruitful discussions as well as to Ing. Martina Čubová Urbanová, PhD. for help with measurements.

Many thanks go to my family, especially to my beloved girlfriend and my daughter Rozárka, who let me discover the true meaning of life.

Annotation

This thesis deals with the application of advanced methods of solid-state nuclear magnetic resonance (NMR) spectroscopy to determine the crystallographic positions of extra-framework cations in zeolites. The dehydrated lithium and sodium forms of zeolites ferrierites have been investigated using various single- and two-dimensional NMR techniques to distinguish individual cationic positions. Lithium, sodium and potassium forms of the zeolite chabazite were examined in both the hydrated and dehydrated state to investigate the effect of the cation on the NMR spectrum of framework aluminium. The experimental data have been interpreted using results of quantum chemical calculations.

Keywords

zeolite, solid-state NMR spectroscopy, framework Al site, extra-framework cations, ferrierite, chabazite, heterogeneous catalysis

Název

NMR spektroskopie kationtů v mimomřížkových polohách zeolitů

Anotace

Tato práce se zabývá aplikací pokročilých metod spektroskopie nukleární magnetické rezonance (NMR) pevné fáze pro určení krystalografických poloh mimomřížkových kationtů v zeolitech. Dehydratované lithné a sodné formy zeolitů ferrieritů byly zkoumány pomocí různých jedno- a dvoudimenzionálních NMR experimentů za účelem rozlišení jednotlivých kationtových poloh. Lithné, sodné a draselné formy zeolitu strukturního typu CHA byly zkoumány v hydratovaném i dehydratovaném stavu pro zjištění vlivu kationtu na NMR spektrum skeletálního hliníku. Pro interpretaci naměřených dat byly použity výsledky kvantově chemických výpočtů.

Klíčová slova

zeolit, NMR spektroskopie pevné fáze, mřížková poloha Al, mimomřížkové kationty, ferrierit, chabazit, heterogenní katalýza

Souhrn

Tato práce se zabývá aplikací pokročilých metod spektroskopie nukleární magnetické rezonance (NMR) pevné fáze pro určení mimomřížkových poloh vybraných jednomocných kationtů alkalických kovů v zeolitech.

Jedním z cílů bylo vytvoření postupu pro rozlišení jednotlivých krystalografických poloh kationtů Li^+ a Na^+ v zeolitech s vysokým obsahem křemíku, včetně ověření možnosti interpretace NMR spekter pomocí kvantově chemických výpočtů. Jako modelový systém byl zvolen zeolit strukturního typu FER. Na základě komplexní analýzy sady syntetických FER zeolitů pomocí ^{27}Al NMR, ^{29}Si NMR a UV-Vis spektroskopie byly vybrány tři vzorky s rozdílnou distribucí Al ve skeletu. Jejich dehydratované lithné a sodné formy byly následně zkoumány pomocí NMR technik pevné fáze za rotace vzorku pod magickým úhlem (MAS). Pro rozlišení neekvivalentních krystalografických poloh Li^+ v úzkém rozsahu chemických posunů byl poprvé použit dvourozměrný ^{7}Li-^{7}Li výměnný korelační (EXSY) NMR experiment. Relativní zastoupení Li^+ v jednotlivých polohách bylo následně určeno pomocí dekonvoluce jednorozměrného ^{7}Li MAS NMR spektra. Pro rozlišení kvadrupolárně rozšířených signálů jednotlivých poloh Na^+ bylo nutné souběžně analyzovat jednorozměrná ^{23}Na MAS NMR a dvourozměrná vícekvantová (MQ) MAS NMR spektra změřená na dvou různých magnetických polích (vysokém a ultra-vysokém). Pro interpretaci NMR spekter byly použity kvantově-chemické výpočty. Vypočtené NMR parametry byly v dobrém souladu s experimentálními hodnotami, avšak podobnost vypočtených parametrů některých kationtových poloh neumožnila jejich dostatečné rozlišení bez znalosti distribuce Al ve skeletu.

Dalším z cílů bylo ověření možnosti analýzy struktury kationtové polohy nepřímo pomocí ^{27}Al MAS NMR s využitím vlivu kationtu na koordinaci Al v dehydratovaném zeolitu. K tomu byl vybrán zeolit strukturního typu CHA, který obsahuje pouze jednu mřížkovou polohu Al. Jeho lithné, sodné a draselné formy byly zkoumány v hydratovaném i dehydratovaném stavu pomocí ^{27}Al MAS a MQMAS NMR experimentů. Bylo zjištěno znatelné rozšíření Al spekter dehydratovaných vzorků v závislosti na iontovém poloměru mimomřížkového kationtu. Analýza tohoto rozšíření přináší další strukturní informace o mimomřížkových polohách kationtů v zeolitech, a to včetně K^+, které je obtížně měřitelné. Teoretické výpočty prokázaly, že příčinou rozšíření je především deformace AlO_4^-, která je způsobena navázáním kationtu.

Table of Content

List of Abbreviations

1D	one-dimensional
2D	two-dimensional
3D	three-dimensional
A	anisotropy
BTOP	benzene to phenol
CBU	composite building unit
CP	cross-polarization
CT	central transition
CS	chemical shielding
CSA	chemical shielding anisotropy
DFT	density functional theory
EFG	electric field gradient
EXSY	exchange spectroscopy
FAU	faujasite
FCC	fluid catalytic cracking
FER	ferrierite
FID	free induction decay
FT	Fourier transformation
FTIR	Fourier-transform infrared spectroscopy
HD	high definition
hpdec	high-power decoupling
HR	high resolution
MAS	magic angle spinning
MQMAS	multiple quantum magic angle spinning
MTG	methanol to gasoline
MTO	methanol to olefins
NMR	nuclear magnetic resonance
NOESY	nuclear Overhauser effect spectroscopy
o.d.	outer diameter
PAS	principal axis system
PBU	primary building unit
ppm	parts per million (of resonance frequency)
QIS	quadrupolar induced shift
rf	radio-frequency
SBU	secondary building unit
SOD	sodalite
ssNMR	solid state nuclear magnetic resonance
Si/Al	silicon to aluminium ratio
S/N	signal to noise ratio
ST	satellite transition
UC	unit cell
US	ultra-stabilized
UV-Vis	ultraviolet-visible spectroscopy
WB	wide bore
XRD	X-ray diffraction
ZSM-5	Zeolite Socony Mobile #5

List of Symbols

α, β	energy state labels
α, β, γ	unit cell angles
γ	gyromagnetic ratio
δ	chemical shift
$\varDelta$	difference
Δ	anisotropy of CS
η	asymmetry of chemical shielding
η_q	asymmetry of the electric field gradient tensor
θ_rf	tip angle
θ, ϕ	polar angles
μ	nuclear spin magnetic moment
ν_0	Larmor frequency (Hz)
ν_rot	frequency of rotation (Hz)
σ	chemical shielding
$\sigma_{11}, \sigma_{22}, \sigma_{33}$	principal components of the nuclear shielding tensor
σ_iso	isotropic chemical shielding
τ	time
τ_rf	length of applied radio-frequency pulse
ω_0	Larmor frequency ($\mathrm{rad.s^{-1}}$)
ω_1	nutation frequency ($\mathrm{rad.s^{-1}}$)
ω_rf	radio-frequency transmitter frequency
a, b, c	unit cell dimensions
B_0	magnitude of the applied external magnetic field
B_1	magnitude of the applied radio frequency field
B_eff	effective magnetic field
B_loc	magnitude of the local magnetic field
C_Q	quadrupolar coupling constant
d_1	interscan (recycle) delay
d_D	dipolar-coupling constant
E	energy
h	Planck's constant
$\hbar$	reduced Planck's constant (Planck's constant divided by 2π)
$\hat{\mathrm{H}}$	interaction Hamiltonian
I, S	nuclear spins
$\mathbf{I}, \mathbf{S}$	nuclear spin vectors
$\mathbf{M}_0$	net magnetization vector
N	population
p_1	length of applied pulse
P_q	quadrupolar product
Q	nuclear electric quadrupole moment
T_1	spin-lattice relaxation time constant
T_2	transverse relaxation time constant
V_{11}, V_{22}, V_{33}	principal components of the gradient of the electric field vector

List of Figures

List of Tables

1 Introduction

Zeolites are microporous crystalline aluminosilicates with three-dimensional framework. These few words describe a unique combination of properties that nominate zeolites to play an important role in modern chemistry and technology. The term zeolite was originally introduced in 1756 by Swedish mineralogist Axel Fredrik Cronstedt, who observed large amounts of steam produced by heating the mineral stilbite. Zeolites occur as natural minerals, but more important are zeolites synthetized by researchers or produced industrially. Because of the regular microporous structure leading to large surface area, well organized micropore channel system, presence of exchangeable cationic species and high chemical and thermal stability, zeolites are used in a variety of applications with a global market of several million tones per year.[1] There are three main commercial applications of zeolites: in detergents, in separation and absorption, and in catalysis. The largest application in volume is in detergents, but with respect to financial market and industrial impact, catalysis is the largest application of zeolites.[1] In the case of catalysis mostly synthetic ones are used, since their properties for the specific reactions and processes can be controlled by tuning synthesis parameters. The knowledge of the relationship between chemical composition, structural parameters and chemical and physical properties of the material in a particular process is essential for design, development and application of zeolite materials for the new generation of highly effective and environmentally friendly catalytic processes. Solid-state nuclear magnetic resonance (ssNMR) represents one of the most powerful analytical methods for determining the structural properties at the atomic scale. This method allows a unique view of coordinating state and chemical environment of individual atoms. My work deals with the applications of ssNMR supported by quantum chemical calculations for the analysis of crystallographic positions of extra-framework cations in zeolites. Aims have been focused on alkali metal cations in silicon-rich zeolites with low relative concentration of aluminium in the framework. In presented thesis, impact of zeolites on catalysis and methods for analysis of extra-framework cations in zeolites are briefly introduced, followed by description of zeolite structure and chemical composition in Chapter 2. Solid-state NMR spectroscopy and its application for characterization of zeolites are described in Chapter 3. Aim of study with main goals is pointed out in Chapter 4 and materials and methods that helped to achieve them are described in Chapter 5. Results are shown and discussed in Chapter 6 and concluded in Chapter 7.

1.1 Zeolites in Heterogeneous Catalysis

In zeolite catalyst, chemical reactions take place within the internal channels and cavities. The isomorphous substitution of Si^{IV} atoms by the Al^{III} ones introduces negative charge into the silicate framework, which has to be compensated by positively charged ions or protons. These cationic species occupy extra-framework positions in the zeolite channels and can play a role of reaction/sorption centers (active sites) accessible for various molecules through channel system. Well-defined microporous structure (see Figure 1) with pore sizes of molecular dimension provides shape-selectivity where the shape and size of a particular pore system has a steric influence on the reaction, its transition-states[2] and controlling the access of reactants and products.

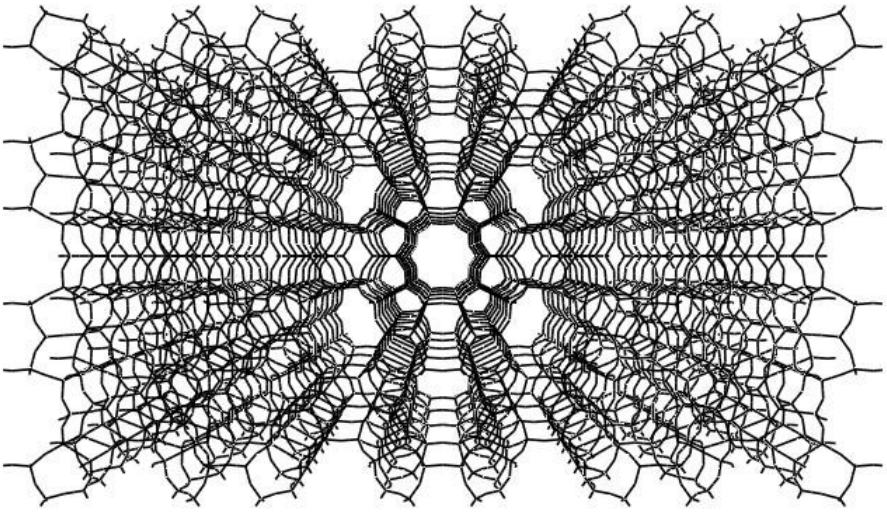

Figure 1. 3D structure of FER framework type viewed along 10-ring channel [001]

Due to flexible chemical composition is possible to control the type (whether acid, base or redox), number and strength of active sites as well as the adsorption properties. There are concentration effects due to high adsorption capacity leading to high reaction rates. Silicon-rich zeolites have outstanding thermal and hydrothermal stability making their regeneration easy and repeatable.

Aluminum-rich zeolites (Si/Al 1 - 4) with faujasite (FAU) structure are the most common zeolites used in heterogeneous catalysis. Nevertheless, in recent thirty years, the application of silicon-rich zeolites (Si/Al > 6) arises of which ZSM-5, beta zeolite, MCM-22, mordenite and ferrierite exhibit the highest industrial impact.[3,4] An important class of reactions are that catalyzed by protonic form of zeolites, whose framework-bound protons give rise to very high acidity. This is utilized in many industrial application in oil refining and petrochemistry, including crude oil cracking (fluid catalytic cracking - FCC, hydrocracking), isomerization and alkylation of paraffins/olefins, and conversion of methanol to hydrocarbons (methanol to gasoline - MTG, methanol to light olefins – MTO).[3,5-8]

Zeolitic materials where Al is replaced by other isomorphously substituted metal exhibit unique properties as demonstrated in the use of titanium silicate TS-1 in the production of caprolactam,[9] propylene epoxidation, phenol hydroxylation, cyclohexanone ammoximation,[10] and in the oxidation of benzene to phenol by nitrous oxide (BTOP reaction).[11,12] Zeolite-based catalysts with transition metal ions in extra-framework positions exhibiting unique redox properties have found applications in the abatement of NO_x from diesel engine exhaust gases and in nitric acid plants.[13-15] There are also many promising application in hydrocarbon syntheses, synthesis of fine chemicals,[16,17] biomass conversion,[18] the conversion of methane to form more valuable products (such as methanol and benzene)[19] and carbon dioxide utilization and abatement.[20] Zeolites are frequently referred as “green catalysts”.[17]

These developments and related successes have only been possible by our increased knowledge and related technological advances in the tailoring of zeolite-based catalysts. In the last decade, we have seen an expanding scientific base, often obtained by a synergistic approach between experiment and theory, for the advanced synthesis and use of zeolites. The design of advanced catalytic systems exhibiting high activity and selectivity and meeting requirements on industrial applications represents a complex process, which can hardly be finalized without the detailed knowledge of the structure of the active sites and their distribution in the molecular sieve.

1.2 Analysis of Cation Siting in Si-rich Zeolites

The physico-chemical properties of zeolites are strongly related to the crystal structure. The key information is not only in the structure type, but also in the distribution of the aluminium and derived distribution of the cations in extra-framework positions in the zeolite cavities and channels. Since the distribution of the cations controls the electric fields, the characterization of the cation sites is a prerequisite for understanding of the physical properties of zeolites.[21] To describe methods for characterization of zeolites is far beyond the scope of this thesis.

Basic spectroscopic method for analysis of structure parameters and cation siting is X-ray diffraction (XRD). In aluminium-rich zeolites extra-framework sites of different cations (except lithium) are very well described by XRD in the number of publications and are compiled by Mortier[22] for the most common structure types.

Contrary to Al-rich zeolites, publications on cation siting in Si-rich zeolites are less numerous. Diffraction studies of cations in extra-framework positions in silicon-rich zeolites meet extreme difficulties due to the low concentration of active sites, large unit cells with a low symmetry, and a high number of different local structures accommodating cationic sites and often having several close structures. In pioneer work by Olson et al.[23], synchrotron diffraction was used to characterize Cs^+ in ZSM-5. Mentzen[24] analyzed H-, Li-, Na-, K-, Rb-, and Tl-ZSM-5 using synchrotron a neutron diffraction. Dalconi and co-workers identified only 3 different cobalt sites in dehydrated ferrierite (Co-FER with Si/Al 8,5) by XRD and EXAFS[25] and 4 cationic sites in dehydrated zeolite Ni-FER with the Si/Al 8,5 by powder XRD.[26] Seff[27] characterized Cs^+ sites in single crystal of ZSM-5 using synchrotron diffraction. Dědeček et al.[28,29] analyzed Co^{2+} siting in hydrated and dehydrated Si-rich zeolites by a UV-Vis diffuse reflectance spectroscopy. Analysis of accessibility and nature of active sites by adsorption of probe molecules and monitored using combination of FTIR and DFT calculations was reviewed by Nachtigall.[30] An important method for characterization of cations and adsorbed molecules in zeolites reveals solid-state NMR spectroscopy.

2 Zeolites - Structure and Chemical Composition

Zeolite framework can be described is as regular 3D network of TO_4 tetrahedra linked together by their corners, whereas T represents Si and Al atoms. The variability in organization of building tetrahedra and in chemical composition results in almost infinite possible arrangements of both channel system and local structure of the zeolite walls. Apart from regular framework, zeolites can contain impurities, inhomogeneity, disordered parts, terminating Si-OH groups, octahedral extra-framework aluminium species, bulky silanol nests etc., which can influence zeolite properties.

The rigid TO_4 tetrahedron represents the primary building unit (PBU) of the zeolite framework. The O-T-O angle is 109° 28‘ for a geometrically perfect tetrahedron and deviations of more than a few degrees are not frequent.[31] The T-O bond length depends on the particular T-atom. To build zeolite frameworks the tetrahedra are connected by shared oxygen. The T-O-T bond angle is quite flexible, in contrast to the rigid O-T-O one. The flexibility of the T-O-T angle is very important since it allows the formation of the great variety of zeolite frameworks without strong thermodynamic barrier.[32] The flexibility of the T-O-T angle allows the formation of rings and other more complex building units. It has be mentioned that T-O-T angle depends also on the nature of the T-atom and replacement of Si by Al atom results in significant angle deformation due to the difference in the bond length.

By linking groups of PBUs together, secondary building units (SBUs) can be formed. The simplest examples of SBUs are rings. In general, a ring containing *n* tetrahedra is called an *n* -ring. The most common rings contain 4, 5, 6, 8, 10, or 12 tetrahedra, but materials with rings formed of 14, 18, up to 20 tetrahedra have been prepared.[33] Materials with 3-, 7- or 9-rings, are rare.[34] When a ring defines the face of a polyhedral unit, it is also called a window. Although the rings are sometimes planar, more often they have more complicated shape and geometry.

At the next level of complexity is obtained by constructing larger composite building units (CBUs) from *n*-rings giving rise to a diverse and interesting set of structures, such as double *n*-rings, polyhedral units and chains. By combination of CBUs together any zeolite structure with channels (and cavities) can be build. A channel is a pore that is infinitely extended in one dimension with a minimum aperture size (*n*-ring) that allows guest molecules to diffuse along the pore. In many zeolites the channels intersect forming two- and three-dimensional channel systems. The dimensions of the pore are one of the critical properties of zeolite materials since this dimension determines the maximum size of the molecules that can enter from the exterior of the zeolite crystal into its micropores. CBU, framework structure and channel system of various framework structures are shown in Figure 2.

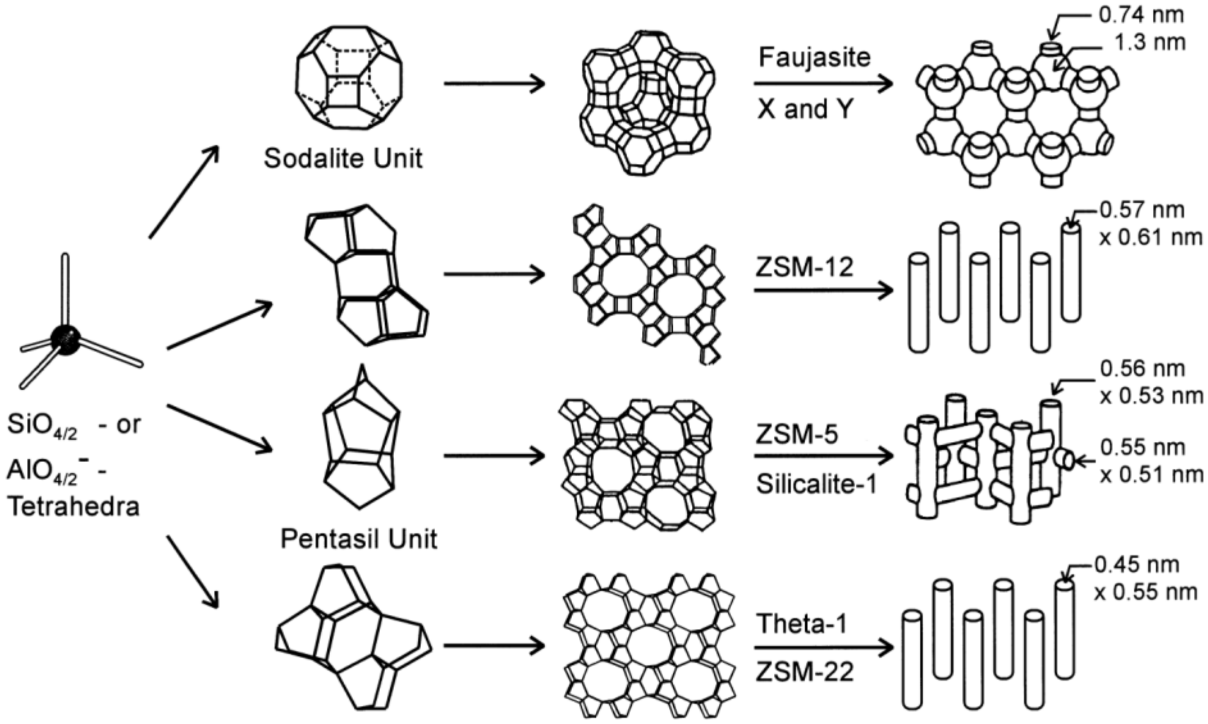

Figure 2. Structures of four selected zeolites (from top to bottom: faujasite or zeolites X, Y; zeolite ZSM-12; zeolite ZSM-5 or silicalite-1; zeolite Theta-1 or ZSM-22) and their micropore systems and dimensions[35]

Zeolites as any crystalline material can be described by Unit Cell (*UC*). This is the smallest building "block" when periodically repeated the whole structure can be build. *UC* is given by its lattice parameters, which are the length of the cell edges and the angles between them, number of T-atoms and their topology and framework density (number of T-atoms per 1000 Å^3).

2.1 Framework Structure Types

On contrary to infinite possible arrangements, over 230 framework structures with different framework topology are now recognized by the Structure Commission of the International Zeolite Association.[36] In accordance with the IUPAC recommendations on the chemical nomenclature of zeolites and related materials, topologically distinct framework types are represented by a mnemonic code consisting of three capital letters. Generally, these codes derived from the name of the type materials for example FAU for faujasite, SOD for sodalite and FER for ferrierite. These symbols only describe and define the network and the topology of the corner sharing tetrahedrally coordinated framework atoms (T-atoms), irrespective of composition, distribution of the T-atoms (Si, Al, P, Ga, Ge, B, Be, etc.), cell dimensions or symmetry. In this work, zeolites of FER and CHA framework type were investigated.

2.1.1 Ferrierite (FER)

Zeolites of the FER structure are important group of silicon-rich zeolites. Crystal structure of the framework type was first described by Vaughan[37] on the material with chemical formula:

$$|Mg^{2+}{}_2Na^{+}{}_2\,(H_2O)_{18}|\ [Al_6Si_{30}\,O_{72}]\text{-}\mathbf{FER}$$

However, chemical composition is highly variable and ferrierites are synthesized in a wide range of Si/Al ratios as from about 5 up to all-silica materials. Crystal unit cell of FER is orthorhombic (a = 19.0180 Å, b = 14.3030 Å, c = 7.5410Å; $\alpha = \beta = \gamma = 90.000°$) with framework density of 17.6 T-atoms/1000 Å^3 and accessible volume of 10 %. Framework structure (see Figure 3) contains four different T-atoms connected into 5-, 6-, 8- and 10-rings. The two-dimensional channel system is formed by 10-ring channels in [001] plane with free diameter of 4.2 x 5.4 Å interconnected with 8-ring channels in [010] plane with free diameter of 3.5 x 4.8 Å.

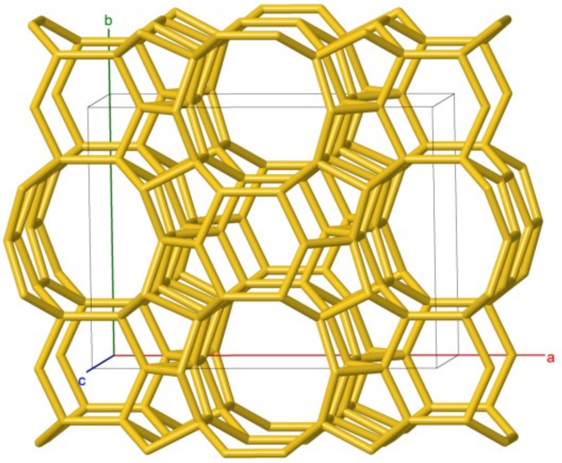

Figure 3. Structure of FER framework unit cell, viewed along [001]

2.1.2 Chabazite (CHA)

Unit cell of CHA framework type is trigonal (*a* = 13.6750 Å, *b* = 13.6750 Å, *c* = 14.7670 Å; α = 90.000°, β = 90.000°, γ = 120.000°) with framework density of 15.1 T/1000 Å^3 and accessible volume of 17.3 %. CHA structure with one T-atom forming 4-, 6- and 8-rings can be viewed as a sequence of double 6-rings forming 3D system of 8-ring channels with free diameter of 3.8 Å with big cavities at intersection. Type material of CHA framework is Al-rich zeolite chabazite with chemical formula:

$$|Ca^{2+}_{6}\,(H_2O)_{40}|\ \mathbf{[}Al_{12}Si_{24}\,O_{72}\mathbf{]\text{-}CHA}$$

Many other related materials differ in chemical composition and unit cell dimensions including Si-rich zeolite SSZ-13, all-silica chabazites, and number of aluminophosphates and silicoaluminophosphates.

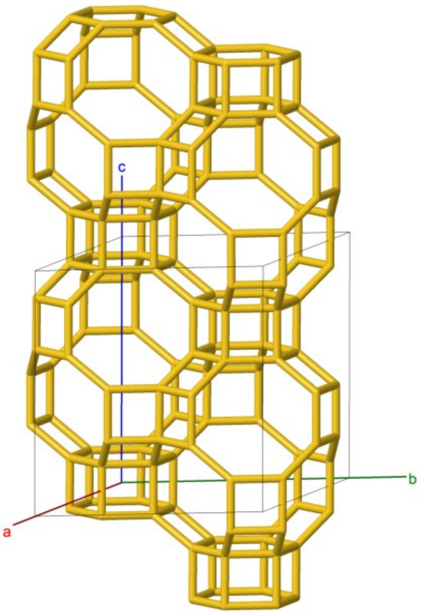

Figure 4. Structure of CHA framework unit cell

2.2 Role of Aluminium in Zeolite Framework

Since Al governs the location of cationic species in the zeolite channel/cavity system as well as their local arrangement (coordination to individual rings) and nature (monovalent species can balance both isolated or close Al atoms, while polyvalent species requires high local framework charge resulting from presence of close Al atoms), description of Al arrangement in the zeolite framework is of high interest. The low content of isomorphously substituted Al in the Si-rich zeolites (Si/Al > 8) provides a wide variety of mutual arrangements of Al atoms in the framework. Al arrangement can be described by two parameters: *distribution* and *siting*. Al distribution describes distances between Al atoms and their positions in n-ring, while siting represents location of Al atoms in crystallographic positions.

2.2.1 Al Distribution

There is only one known empirical rule for the aluminum distribution in the zeolite framework, the Loewenstein rule,[38] excluding two neighboring AlO_4 tetrahedra. Thus, Al-O-Al sequences are not present in the zeolite framework. The absence of other rules governing the mutual arrangement of Al atoms in the framework, establish conditions such that all the $Al\text{-}O\text{-}(Si\text{-}O)_n\text{-}Al$ sequences are allowed in the frameworks of Si-rich zeolites (see Figure 5).[4]

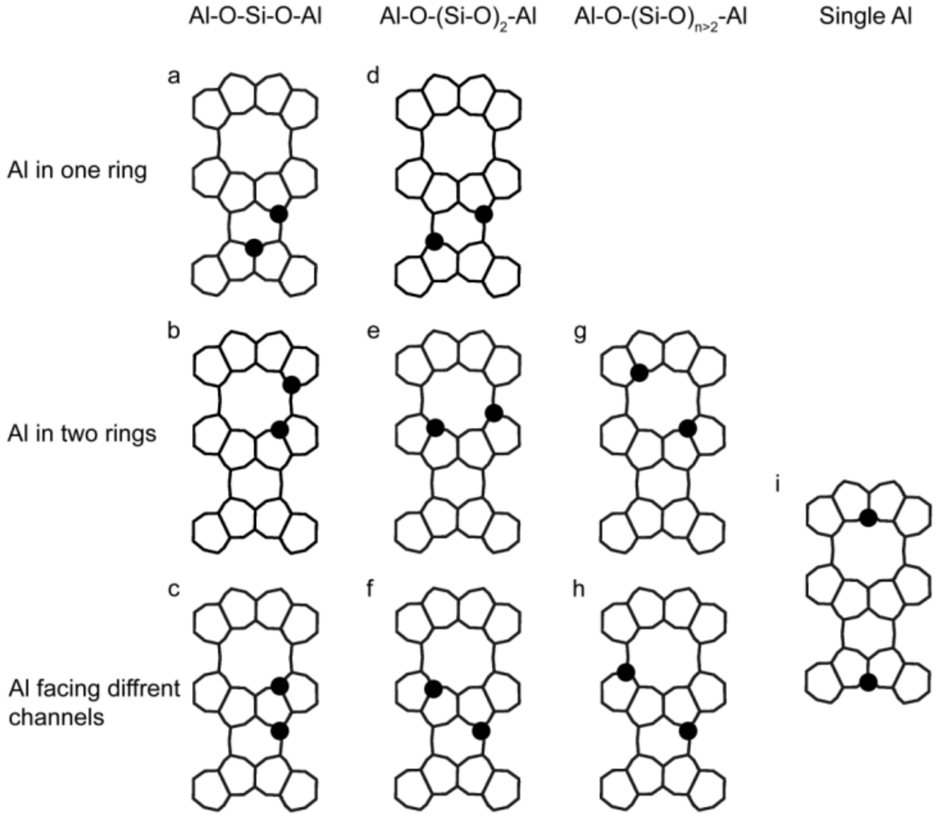

Figure 5. Arrangement of Al distribution in Si-rich zeolites[4]

The term "close Al atoms" is introduced for Al atoms, which participate on the charge balance of the hexaaquo divalent complex in hydrated zeolites. The close Al atoms are represented by Al-O-(Si-O)$_{1,2}$-Al sequences in one ring (and Al-O-(Si-O)$_3$-Al in mordenite), and Al-O-(Si-O)$_{1,2,3}$-Al sequences with Al atoms in different rings in close geometric distance under conditions that the hexaaquo comlex of the divalent ion can cooperate with both these Al atoms (see below the visible distance of Al atoms).

The closest Al atoms present in the zeolites, Al-O-Si-O-Al sequences, are well-known for Al-rich materials (e.g. LTA, FAU topologies). They can be readily detected using standard ^{29}Si MAS NMR analysis. However, these Al sequences are very rare in Si-rich frameworks (for illustration see Figure 5 a, b, c). On the other hand, close Al atoms of Al-O-(Si-O)$_2$-Al sequences in one ring in Si-rich zeolites represent substantial and, in some Si/Al compositions, the predominant fraction of Al atoms. The Al atoms in Al-O-(Si-O)$_2$-Al sequences located in one six-member ring of cationic site (denoted further Al pairs, Al$_2$Al) are of specific importance and occur frequently (as an example see Figure 5 d). The Al-O-(Si-

$O)_3$-Al sequence in an 8-MR was reported only in mordenite. It would behave similarly as the Al-O-$(Si\text{-}O)_2$-Al sequences in 6-MRs and they will accordingly be discussed together. When occupied by the above sequences, the described 6- and 8-MRs represent cationic sites for bare divalent cations bound exclusively to framework oxygen atoms in dehydrated zeolites.[4]

Al-O-$(Si\text{-}O)_n$-Al with n = 2 or 3 with Al atoms located in different rings is also a possibility for Al distribution (Figure 5 e, f). This is the only condition for these Al atoms, albeit there is no way of differentiating amongst the numbers of $(Si\text{-}O)_n$ groups. If close enough, the Al-O-$(Si\text{-}O)_{2.3}$-Al sequences with Al atoms in the different rings can balance the charge of the divalent hexaaquo complex in hydrated zeolites, whereas they are unable to coordinate bare divalent cations in dehydrated zeolites.[4]

2.2.2 Al Siting

Crystallographically different TO_4 tetrahedra units forming the frameworks in Si-rich zeolites consist of at least one unit in zeolite SSZ-13 of CHA structure up to 24 units in monoclinic ZSM-5 or TNU-9. This leads, together with the low Al content (Si/Al > 8), to high variability in the siting of Al atoms, i.e., occupation of the individual framework T-sites, and different populations of Al atoms in these sites. The siting of Al atoms in the individual framework T-sites represents a basic parameter which governs the derived distribution of Al atoms. The parameters describing the Al siting can be suggested as siting of Al atoms in the individual framework rings (essential for the location of protons and location and coordination of metal ions) and siting of Al atoms with respect to the structural channel/cavity system, which thereafter controls the accessibility of charge balancing metal ions or protons for reactants or guest molecules, and the formation of various types of reaction intermediates in the surrounding void volume of the counter ions. Thus the negatively charged AlO_4 tetrahedra in the framework determine the distribution of the local negative charges and derived distribution of active sites.

Recently, it has been shown that the Al siting and distribution in silicon-rich zeolites is not random and depends on the conditions of the zeolite synthesis.[18,39-42] Therefore, the determination of the Al siting in the framework is the first and essential step in the synthesis of zeolites with the defined Al distribution. Nevertheless, Al siting in zeolites with isolated Al atoms can be monitored by solid-state NMR spectroscopy, the presence of close Al structures can dramatically affect ^{27}Al chemical shift, making analysis complicated. Thus, complementary method is needed.

2.3 Cations in Extra-Framework Positions in Si-rich Zeolites

Extra-framework cations play an important role in determining the catalytic properties of zeolites. Positively charged counter ions in the cationic sites bound via framework oxygen atoms neighboring to the framework T-sites occupied by Al atoms. In the exchange of di- or poly-valent cations, a sufficient local negative charge balancing the charges of the cations is required. Thus the siting and distribution of Al atoms in the framework of the zeolite controls the location of the exchanged protons and bare cations, and the structure of metal-ion complexes and their distances in the zeolite structure. This implies an essential importance of the siting and distribution of Al atoms in the zeolite framework for the catalytic properties of zeolite catalysts. Typical positions of divalent cations (denoted as α, β and γ) in the pentasil zeolites are depicted in Figure 6. Specific ionic capacity varies with the structure of the zeolite and the exchanged cation. It has to be mentioned, that in the Si-rich zeolites divalent (or trivalent) cations can occupy only position where are two (or three, respectively) close Al atoms. It leads to the fact, that Al distribution can affect structure of the active sites. It was demonstrated by Dědeček et al.[43] on the set of Cu-ZSM-5s with different Si/Al and Cu loading. Monovalent cations indicate the location of the Al atoms in the individual framework rings and channels, to ensure charge balance.

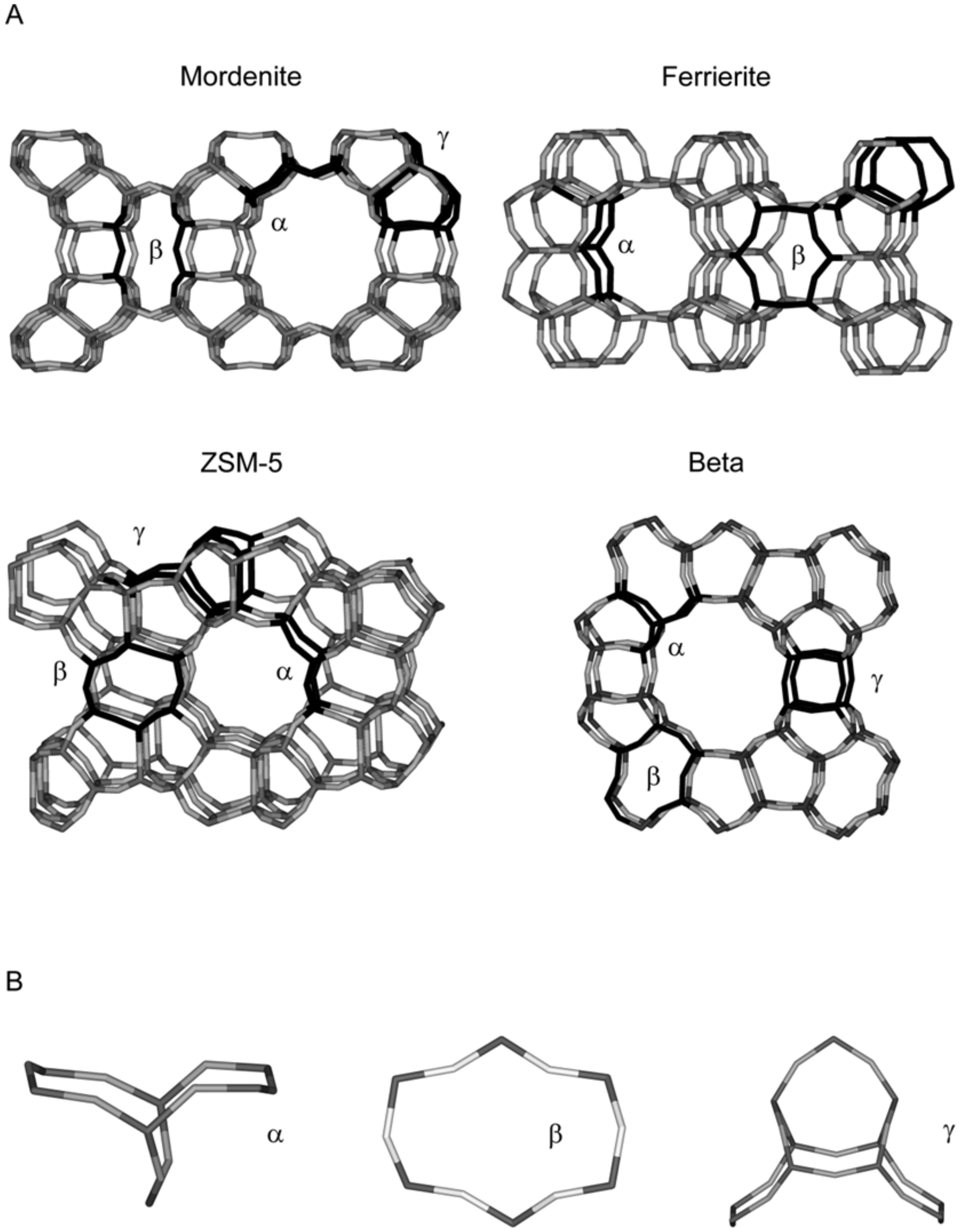

Figure 6. (A) The rings of the α-, β- and γ-type sites in the framework of mordenite, ferrierite, ZSM-5 and beta zeolites, and (B) detail of the α-type site in mordenite, β-type site in the beta zeolite, and γ-type site in ferrierite. (with permission from Ref.[4])

Position of the Cs^+ ion provides evidence only for the location of the Al atoms in the walls of the channels. Thus the location of the Cs^+ ions obtained by XRD for Cs-ZSM-5 indicates only Al atoms located in one T site of the main channels and two T sites are located in the sinusoidal channel.[23] Siting of Al atoms on the intersection of the main and sinusoidal channels results from location of Na^+, K^+, Rb^+ and Tl^+ in the ZSM-5 channel system according to the study of Mentzen et al.[24] Moreover, siting of Al atoms in the T_1 or T_{10}, T_4 or T_7, and T_{10} was suggested using Li^+ ion as a probe monitored by neutron powder diffraction in this study. The discrepancies in the cation and Al siting in different crystallographic studies should reflect variability of Al siting in Si-rich zeolites, clearly evidenced by ^{27}Al MAS NMR studies. The Cu^{II} ions coordinated to four framework oxygens of the α- or β-type cationic sites containing Al-O-$(Si\text{-}O)_2$-Al sequences represent the most active sites in decane-SCR-NO_x (see Figure 7a). On contrary, the Cu^I ions coordinated to two or three framework oxygens and located at the channel intersection adjacent to the single Al atoms in the α- or β-site control predominantly reaction of NO decomposition (see Figure 7b).

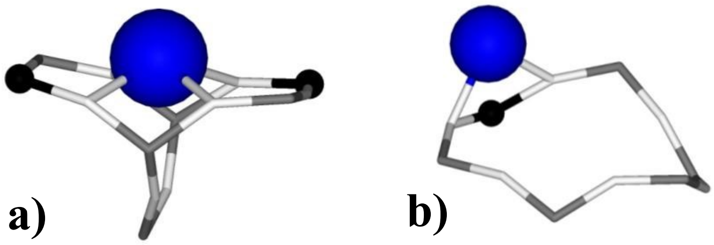

Figure 7. a) Cu ion (blue) balanced by two Al atoms (black) and preferring divalent state – active center for decane SCR-NO_x under water presence. b) Easy reducible Cu ion balanced by isolated Al atom – active center for NO decomposition[43]

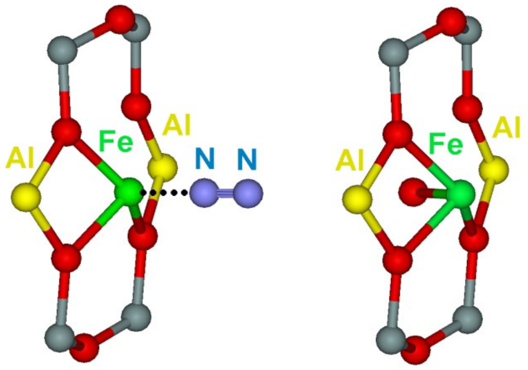

Figure 8. Two Fe^{2+} ions in defined distance and each balanced by two Al atoms – active center for N_2O decomposition in Fe-FER[44]

Sklenák et al.[44] found that active site for N_2O decomposition in pentasil zeolites (ferrierite, ZMS-5 and beta) is formed by two Fe^{2+} ions in defined distance and each balanced by two Al atoms (see Figure 8).

These few examples demonstrates that analysis of cation siting together with Al siting is of the highest interest since not all of the extra-framework species form suitable active sites in particular catalytic processes.

3 Solid-state NMR Spectroscopy – Concepts and Techniques

High-resolution solid-state NMR spectroscopy is a powerful tool for a structural characterization which is not affected by the issues causing difficulties in diffraction studies as discussed above. A high sensitivity of ssNMR techniques for chemical bonds in the local structure of the resonating nuclei is utilized for characterization of framework atoms, extra-framework species, surface sites, and adsorbate complexes in zeolites with great success. Many atoms occurring in zeolites possess isotopes with a nuclear spin, which makes these isotopes NMR active. ^{11}B, ^{17}O, ^{27}Al, ^{29}Si, ^{31}P, ^{51}V, ^{67}Zn, and ^{71}Ga isotopes are accessible for NMR spectroscopy and contribute to the framework of zeolites in a broad manner. ^{1}H, ^{7}Li, ^{23}Na, and ^{133}Cs isotopes are interesting for the characterization of surface OH groups and extra-framework species, such as extra-framework cations.[45]

NMR spectroscopy is described in a number of texts.[46-51] Therefore, this section briefly introduces basic NMR principles and focuses on the mechanisms responsible for the broadening of solid-state NMR signals and line narrowing techniques, which allows acquisition of highly resolved solid-state NMR spectra.

3.1 NMR Principles

"NMR active nuclei," which are observable by NMR, possess a spin-angular momentum defined by the nuclear spin number *I*. The nuclear spin is an intrinsic property of the nucleus. The nuclear magnetic dipole moment **μ** depends on the nuclear spin-angular momentum, defined by the vector **I**:

$$\boldsymbol{\mu} = \gamma \hbar \mathbf{I}$$

where γ is the gyromagnetic ratio and $\hbar$ is reduced Planck's constant (i.e. Planck's constant divided by 2π). The gyromagnetic ratio is unique for each isotope of each element and a very important quantity in NMR, since NMR spectroscopy is based on the precession of the nucleus in a magnetic field. The rate of this precession is known as the Larmor frequency, ω_0, in angular units (rad.s^{-1}) given by:

$$\omega_0 = \gamma B_0$$

where B_0 is the magnetic flux density of the external applied magnetic field.

3.2 NMR Interactions

There are two types of NMR interactions: internal and external. The external interactions depend on B_0, and the oscillating field B_1 induced by a radiofrequency (rf) pulse and solenoidal coil. The internal interactions arise from the magnetic and/or electronic chemical environment of the nucleus, such as chemical shielding, direct and indirect dipolar coupling, quadrupolar coupling, paramagnetic interaction etc. and are described in detail elsewhere.[46-48,50,52] Here, we focus on dominant interactions relevant to this work. These NMR interactions are described by the total Hamiltonian:[52,53]

$$\hat{\mathrm{H}} = \hat{\mathrm{H}}_{\mathrm{Z}} + \hat{\mathrm{H}}_{\mathrm{rf}} + \hat{\mathrm{H}}_{\mathrm{CS}} + \hat{\mathrm{H}}_{\mathrm{D}} + \hat{\mathrm{H}}_{\mathrm{Q}}$$

where $\hat{\mathrm{H}}_{\mathrm{Z}}$, $\hat{\mathrm{H}}_{\mathrm{rf}}$, $\hat{\mathrm{H}}_{\mathrm{CS}}$, $\hat{\mathrm{H}}_{\mathrm{D}}$ and $\hat{\mathrm{H}}_{\mathrm{Q}}$ are the Hamiltonians of the Zeeman interaction, radiofrequency interaction, chemical shielding interaction, dipolar interaction and quadrupolar interaction, respectively.

3.2.1 External Interactions

3.2.1.1 Zeeman Interaction

NMR spectroscopy is based on the interaction of the nuclear spin with the applied external magnetic field B_0. This interaction is known as Zeeman interaction and it is represented as its Hamiltonian form as:[54]

$$\hat{\mathrm{H}}_{\mathrm{Z}} = -\hbar\gamma B_0 \mathbf{I}_{\mathrm{z}}$$

where $\mathbf{I}_{\mathrm{z}}$ is the projection of the nuclear spin angular momentum along the z-axis in the direction of B_0. In an external magnetic field the spin of an NMR active nucleus will precess about the z-axis in one of the $2I + 1$ possible orientations. These orientations or energy levels are described by different values of the nuclear spin magnetic quantum number m_{I}, where $m_{\mathrm{I}} = I, I\text{-}1\ldots, \text{-}I$. In the case of spin I=1/2 , the spin precesses with one of the two energy levels, $m_{\mathrm{I}} = +1/2$ (α state), or $m_{\mathrm{I}} = -1/2$ (β state) (see Figure 9). The difference in energy between these levels (i.e., from α to β) depends on both B_0 and γ:[51,55]

$$\Delta E = \hbar\gamma B_0 = \hbar\omega_0$$

If ΔE increases as the result of increasing in B_0 or γ, the population difference between the energy levels increase.

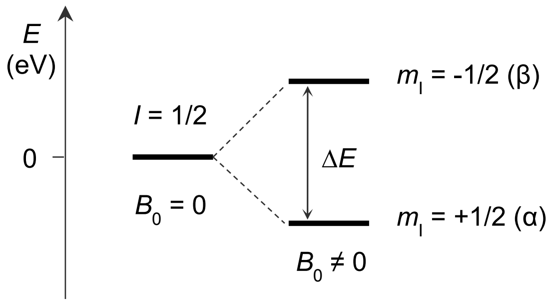

Figure 9. Splitting of energy levels of nucleus with spin $I = 1/2$ in the presence of static magnetic field.

At thermodynamic equilibrium, the non-degenerate energy states are not equally populated, and the ratio of the population between adjacent energy levels is described by the Maxwell-Boltzmann distribution as:[51]

$$\frac{N_\beta}{N_\alpha} = e^{-\frac{\Delta E}{kT}}$$

where N_β and N_α represent the populations of higher (β) and lower (α) energy levels (when $\gamma > 0$), respectively, and k is the Boltzmann constant. As a consequence of longitudinal relaxation, at equilibrium, there are slightly more spins in the α state than in the β state, and as a consequence, there is a bulk magnetization, $\mathbf{M}_0$, directed along the direction of B_0. The difference between spin state populations is relatively small, compared to other forms of spectroscopy, because of the small energy difference between the levels. As a result, NMR is an insensitive technique in terms of the attainable signal-to-noise ratio (S/N).

3.2.1.2 Radiofrequency Interaction

An application of an rf field, B_1, in the direction perpendicular to the static external magnetic field, B_0, induces a spin transition (the change of spin state from α to β or in the opposite direction). The rf Hamiltonian describes the interaction between the nuclear spin and B_1:

$$\hat{\mathrm{H}}_{\mathrm{rf}} = -B_1(t)\cos[\omega_{\mathrm{rf}}t + \varphi(t)]\sum_i \gamma_n^i I_x^i$$

where ω_{rf} is the applied rf and φ is its phase. The nuclear spins interact with B_1 similarly as with B_0, although, B_0 is static and B_1 oscillates in the lab frame in time. An oscillation of B_1 can be visualized as two component vector rotating around B_0 in opposite direction (Figure 10).

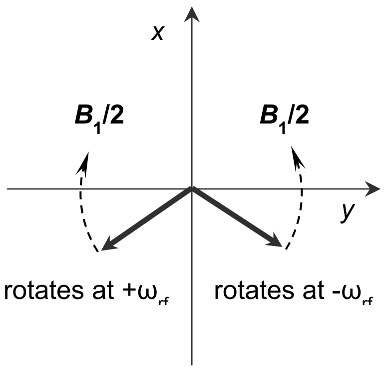

Figure 10. The two vector components of the B_1 field in the *xy*-plane.

The effect of the oscillating B_1 field can be understood by transforming this system into a rotating frame of reference which rotates at the rf transmitter frequency, ω_{rf}. In this rotating frame, the effect of the $\mathbf{B_0}$ field is depleted and the oscillating magnetic field, $\mathbf{B_1}$, appears stationary and has a similar effect on the bulk magnetization as $\mathbf{B_0}$ does in the lab frame (i.e., the magnetization precesses about $\mathbf{B_1}$ for an on-resonance pulse). In the absence of an rf pulse, the bulk magnetization, $\mathbf{M_0}$, precesses along $\mathbf{B_0}$ at a ω_0. When an rf pulse is applied along the *x*-axis of the rotating frame, the bulk magnetization, $\mathbf{M_0}$, rotates counterclockwise by an angle θ_{rf} about the *x*-axis. The angle θ_{rf} is called the tip angle and it is defined by:

$$\theta_{\mathrm{rf}} = \gamma B_1 \tau_{\mathrm{rf}} = \omega_1 \tau_{\mathrm{rf}}$$

where ω_1 is called the nutation frequency and τ_{rf} is the length of applied rf pulse. If the applied pulse is on resonance (i.e., $\omega_0 = \omega_{rf}$), then the bulk magnetization, $\mathbf{M_0}$, appears stationary in the rotating frame and $\mathbf{B_0}$ appears to be absent. The only remaining field is $\mathbf{B_1}$, around which the magnetization precesses. In most NMR experiments, pulses are not applied on resonance. In such cases, the Larmor frequency is then reduced from ω_0 to $(\omega_0 - \omega_{rf})$ and the field along B_0 does not vanish (as it is the case for an on resonance pulse). Thus, in this case there exist two fields, one along the *z*-axis with magnitude equal to $B_0(1 - \omega_{rf}/\omega_0)/\gamma$ and the second of magnitude B_1 along the *x*-axis. The resultant effective field is the vectorial sum of the two components and is denoted as $\mathbf{B_{tot}}$ (Figure 11) around which the nuclear spin magnetization precesses.

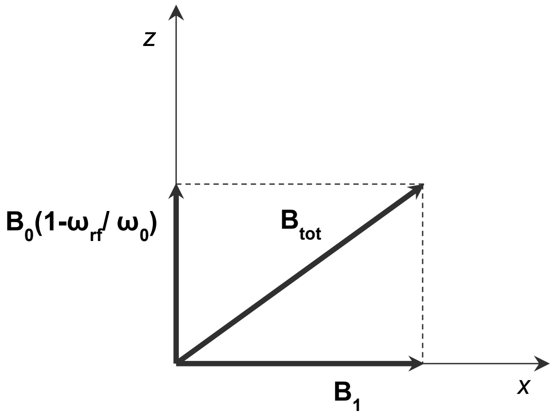

Figure 11. The magnetic fields present in the rotating frame. In the case of an on-resonance pulse ($\omega_0 = \omega_{rf}$), only B_1 remains.

The allowed NMR spin transitions are defined by $\Delta m = \pm 1$. By application of an rf pulse, the energy is absorbed causing spin transitions between two different energy levels, and the population of the two levels become equal, this phenomenon is called saturation. Once the pulse is turned off, the magnetization returns to thermal equilibrium. The system reaches the equilibrium by releasing the acquired energy to the surroundings via a phenomenon called relaxation. There are two fundamental spin relaxation processes. Longitudinal or spin-lattice relaxation, whose time constant is denoted by T_1, is the process by which the magnetization returns back to the initial state of thermal equilibrium (along the z-axis), and transverse or spin-spin relaxation, denoted by T_2, is the magnetization dephasing or loss of phase coherence in the xy-plane.

3.2.2 Internal Interactions

3.2.2.1 Chemical Shielding Interaction

Circulation of the electrons surrounding nucleus in the static external magnetic field generate small local magnetic fields, B_{loc}. Interaction of these fields with nuclear spins is call chemical shielding. Induced local fields change the net magnetic field at the nucleus, leading to changes in its Larmor frequency. The degree of change of the precession frequency reflects the value of the chemical shielding which depends on the total effective magnetic field, B_{eff}, experienced by the nucleus:

$$\vec{B}_{\text{eff}} = \vec{B}_0 + \vec{B}_{\text{loc}} = \vec{B}_0 - \sigma\vec{B}_0 = (1-\sigma)\vec{B}_0$$

The magnitudes of these local magnetic fields depend on the strength of the external applied magnetic field B_0, but more importantly, upon the nature of the orbitals within the atom or molecule. The latter is what makes chemical shielding a sensitive probe of subtle changes in molecular structure. The nuclear shielding Hamiltonian is expressed as:[53]

$$\hat{\mathrm{H}}_{\mathrm{Z}} = -\gamma\hbar\mathbf{I}_{\mathrm{z}}\ddot{\sigma}\mathbf{B}_0$$

where $\ddot{\sigma}$ is the chemical shielding non-symmetric second-rank tensor.

$$\ddot{\sigma} = \begin{pmatrix} \sigma_{\mathrm{xx}} & \sigma_{xy} & \sigma_{xz} \\ \sigma_{yx} & \sigma_{\mathrm{yy}} & \sigma_{yz} \\ \sigma_{zx} & \sigma_{zy} & \sigma_{\mathrm{zz}} \end{pmatrix}$$

σ_{xx}, σ_{xy}, etc. are the electric field vector components in an arbitrary reference frame. This tensor can be diagonalized by transformation into its own principal axis system (PAS), which is fixed in orientation with respect to the molecule:

$$\ddot{\sigma}_{\mathrm{PAS}} = \begin{pmatrix} \sigma_{11} & 0 & 0 \\ 0 & \sigma_{22} & 0 \\ 0 & 0 & \sigma_{33} \end{pmatrix}$$

where σ_{11}, σ_{22} and σ_{33} are the principal components of the chemical shielding tensor (Figure 12) and $\sigma_{11} \leq \sigma_{22} \leq \sigma_{33}$.

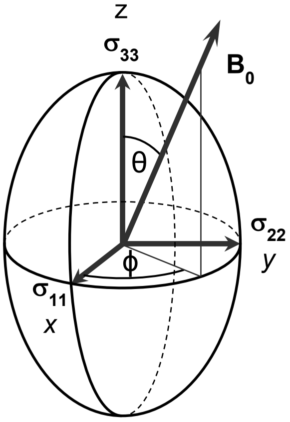

Figure 12. An ellipsoid depicting the three principal components (σ_{11}, σ_{22}, σ_{33}) of the chemical shielding tensor and polar angles (θ, ϕ) describing the direction of the external magnetic field (B_0)

These values are frequently expressed as the isotropic value of chemical shielding σ_{iso}, the anisotropy Δ, and the asymmetry η as follows:[50]

$$\sigma_{\mathrm{iso}} = \frac{(\sigma_{11} + \sigma_{22} + \sigma_{33})}{3}$$

$$\Delta = \sigma_{33} - \sigma_{\mathrm{iso}}$$

$$\eta = \frac{(\sigma_{11} - \sigma_{22})}{\sigma_{33} - \sigma_{\mathrm{iso}}}$$

The direction of $\mathbf{B}_0$ in PAS of the chemical shielding tensor is described by polar angles θ and ϕ (see Figure 12 for definition). The contribution to the spectral frequency from the chemical shielding ω_{cs} in absolute value for given orientation of shielding tensor is expressed as:[47]

$$\omega_{\mathrm{cs}}(\theta, \phi) = -\omega_0\sigma_{\mathrm{iso}} - \frac{1}{2}\omega_0\Delta[(3\cos^2\theta - 1) + \eta(\sin^2\theta\cos 2\phi)]$$

where the quantity - $\omega_{cs}\sigma_{iso}= \omega_{iso}$ is the isotropic chemical shift frequency, relative to bare nucleus. This equation indicates that chemical shielding depends on the orientation of molecules with respect to the applied magnetic field. The orientation dependence of the chemical shielding is referred to as chemical shielding anisotropy (CSA). In solution, sharp peaks representing the average shielding are observed, due to the fast isotropic reorientation of molecules. In microcrystalline or powder sample, all orientations of crystallites or molecules are present and all values of θ and ϕ are possible. Each different orientation implies different orientation of PAS with respect to $\mathbf{B}_0$ and thus a different chemical shielding. The spectrum will cover a range of frequencies from the different orientations, yielding NMR powder pattern. Overlapping lines form continuous lineshape, where the intensity at a given frequency is proportional to the number of molecular orientations with particular chemical shielding. This means that the powder pattern lineshape depends on the symmetry of the shielding tensor and thus on the site symmetry at the nucleus. Principal components of chemical shielding tensor can be obtained from discontinuities and shoulders of powder pattern influenced only by CSA. Three different orientations of chemical shielding tensor and corresponding shielding values in powder pattern are depicted in Figure 13.

The shielding tensor components determine the shape of the powder pattern. The effect of anisotropy and asymmetry of the chemical shielding tensor on the powder pattern lineshape is shown in Figure 14. The anisotropy determines the breath of the lineshape, while the asymmetry its shape.

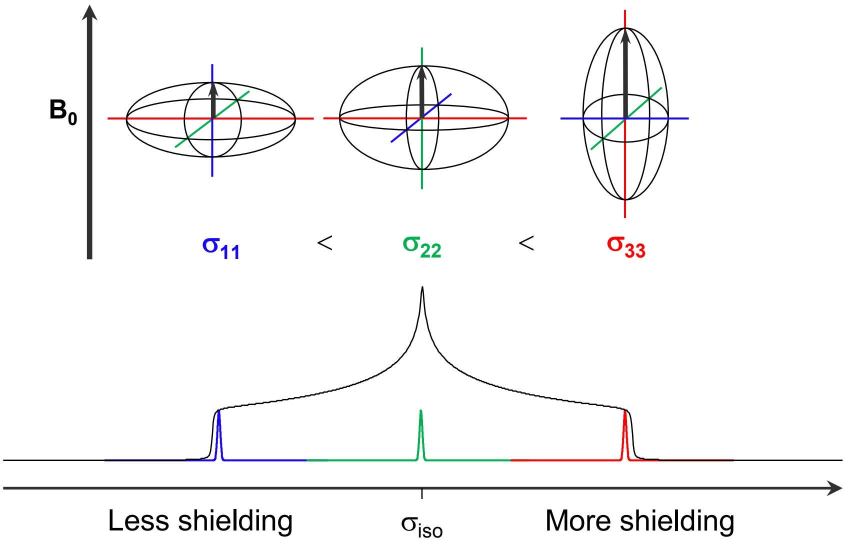

Figure 13. CSA powder pattern with principal values of chemical shielding tensor. Different tensor orientations with respect to the external magnetic field lead to different chemical shielding

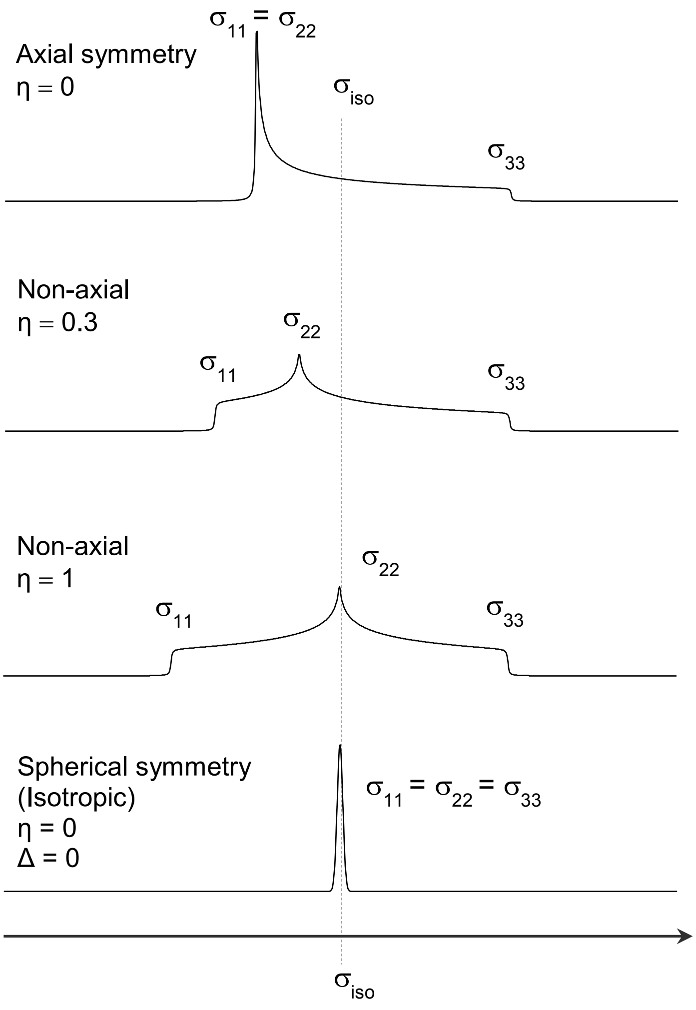

Figure 14. The effect of asymmetry of the chemical shielding tensor on the static powder pattern lineshape

The total spectral frequency in absolute units is the Larmor frequency plus the chemical shielding contribution:[54]

$$\omega = \omega_0 + \omega_{cs}(\theta, \varphi)$$

In NMR experiment absolute frequencies are not measured directly, rather frequencies of lines relative to a specific line in the spectrum of reference compound are measured and quoted as chemical shift with respect to that compound. The chemical shift δ is reported in parts per million of resonance frequency and is defined as

$$\delta(\text{ppm}) = \frac{\nu_{\text{sample}} - \nu_{\text{ref}}}{\nu_{\text{ref}}} \times 10^6$$

where ν_{sample} (Hz) is the spectral frequency of the signal for the spin of interest and ν_{ref} is the resonance frequency of the same spin in reference compound. The chemical shielding and chemical shift are related by:

$$\delta = \frac{\sigma_{\text{ref}} - \sigma_{\text{sample}}}{1 - \sigma_{\text{ref}}} \approx \sigma_{\text{ref}} - \sigma_{\text{sample}}$$

where σ_{ref} is the chemical shielding of the spin in reference compound and σ_{sample} is the chemical shielding of the spin of interest.

3.2.2.2 Direct Dipolar Interaction

The direct dipolar interaction, as known as the dipole-dipole interaction or dipolar coupling, is the through-space interaction between the magnetic moments of two nuclear spins separated by a distance r. It is caused by interaction of local magnetic fields around nuclei and is independent on the B_0. The interaction Hamiltonian for dipolar coupling between spins I and S in angular frequency units (rad.s^{-1}) is given by:[54]

$$\hat{\text{H}}_{\text{D}} = -\left(\frac{\mu_0}{4\pi}\right)\frac{\gamma_{\text{I}}\gamma_{\text{S}}\hbar}{r^3}\left[\mathbf{I}\cdot\mathbf{S} - 3\frac{(\mathbf{I}\cdot\mathbf{r})(\mathbf{S}\cdot\mathbf{r})}{r^2}\right]$$

$$d_{\text{D}} = \left(\frac{\mu_0}{4\pi}\right)\frac{\gamma_{\text{I}}\gamma_{\text{S}}\hbar}{r^3}$$

where μ_0 is the magnetic constant (permeability of vacuum), $\mathbf{r}$ is a vector joining two dipoles, r is the distance between them and d_{D} is the *dipolar-coupling constant* in units rad.s^{-1}. The dipolar interaction depends on the gyromagnetic ratios of the nuclei and is inversely proportional to the cube of their distance; therefore, this interaction is more important for nuclei with larger magnetic moments and for nuclei which are relatively close in space.

The dipolar coupling of spins is either between same species (homonuclear dipolar coupling) or between two different nuclei (heteronuclear dipolar coupling). The homonuclear dipolar coupling Hamiltonian is expressed as [54]:

$$\hat{\mathrm{H}}_{\mathrm{D}}^{\mathrm{homo}} = -d_{\mathrm{D}}\frac{1}{2}(3\cos^2\theta_{\mathrm{IS}} - 1)[3I_zS_z - \mathbf{I}\cdot\mathbf{S}]$$

and the heteronuclear dipolar coupling Hamiltonian as [54]:

$$\hat{\mathrm{H}}_{\mathrm{D}}^{\mathrm{hetero}} = -d_{\mathrm{D}}(3\cos^2\theta_{\mathrm{IS}} - 1)I_zS_z$$

where θ_{IS} is the angle between vector $\mathbf{r}$ and $\mathbf{B_0}$. In liquids the dipolar interaction is averaged by molecular tumbling, while in solids line broadening can occur and can be removed by magic angle spinning (MAS – see chapter 3.3.1).

3.2.2.3 Quadrupolar Interaction

Quadrupolar nuclei (i.e. nuclei with spins I > ½) have a non-spherical positive charge distribution which gives rise to a nuclear electric quadrupole moment. The electric quadrupole moment is defined by a scalar value, Q, and is unique for each quadrupolar nucleus. The quadrupolar interaction is the interaction between the nuclear electric quadrupolar moment and the local electric field gradient (EFG) around the nucleus. The EFG is caused by the electronic charge distribution around nucleus (i.e. electrons, atoms bonds, etc.); therefore, the EFG is very sensitive to small structural changes. The Hamiltonian of the quadrupolar interaction in angular frequency units is expressed by [54]:

$$\hat{\mathrm{H}}_{\mathrm{Q}} = \frac{eQ}{2I(2I-1)\hbar}\mathbf{I}\cdot\ddot{\mathbf{V}}\cdot\mathbf{I}$$

where $\mathbf{I}$ is the nuclear spin operator, and $\ddot{\mathbf{V}}$ is the EFG second-rank tensor:

$$\ddot{\mathrm{V}} = \begin{pmatrix} V_{xx} & V_{xy} & V_{xz} \\ V_{yx} & V_{yy} & V_{yz} \\ V_{zx} & V_{zy} & V_{zz} \end{pmatrix}$$

where V_{xx}, V_{xy}, etc. represent the gradient of the electric field vector components in an arbitrary reference frame. This tensor can be diagonalized by transformation into its PAS:[16]

$$\ddot{\mathrm{V}}_{\mathrm{PAS}} = \begin{pmatrix} V_{11} & 0 & 0 \\ 0 & V_{22} & 0 \\ 0 & 0 & V_{33} \end{pmatrix}$$

PAS components of the gradient of the electric field vector are defined as $|V_{33}| \geq |V_{22}| \geq |V_{11}|$ and this tensor is symmetric and traceless ($V_{11} + V_{22} + V_{33} = 0$). Information about the spherical and axial symmetry of the EFG tensor can be obtain by the measurement of the nuclear quadrupolar coupling constant (C_{Q}) and the asymmetry parameter (η_{Q}). The C_{Q} is defined as:

$$C_{\mathrm{Q}} = \frac{eQV_{33}}{\mathrm{h}}$$

and asymmetry parameter as:

$$\eta_{\mathrm{Q}} = \frac{V_{11} - V_{22}}{V_{33}}$$

where η_{Q} is dimensionless and varies from 0 to 1 and C_{Q} is reported in MHz. When $V_{11} = V_{22}$, $\eta_{\mathrm{Q}} = 0$ and the EFG tensor is axially symmetric, while if $V_{11} = V_{22} = V_{33} = 0$, C_{Q} is equal to zero and the nucleus is located in a site with spherical symmetry. To describe quadrupolar interaction the quadrupolar product (P_{Q}) can be used:

$$P_{\mathrm{Q}} = C_{\mathrm{Q}}\left(1 + \eta_{\mathrm{Q}}{}^{2/3}\right)^{1/2}$$

The quadrupolar Hamiltonian can be written as:

$$\hat{\mathrm{H}}_{\mathrm{Q}} = \hat{\mathrm{H}}_{\mathrm{Q}}{}^{1} + \hat{\mathrm{H}}_{\mathrm{Q}}{}^{2} + \ \ldots$$

where $\hat{\mathrm{H}}_{\mathrm{Q}}{}^{1}$ and $\hat{\mathrm{H}}_{\mathrm{Q}}{}^{2}$ represents the first- and second-order quadrupolar Hamiltonians, respectively. Mostly, the spectra of quadrupolar nuclei are affected only by first- and second-order quadrupolar interaction, thus, we neglect higher then second-order terms in this work.

Both, the first- and second-order quadrupolar interactions cause large energy shifts in Zeeman levels. In the case of spin I = 3/2 quadrupolar nuclei, four ($2I + 1$) quantized energy levels exist (see Figure 15). The transition from -1/2 to +1/2 is called the central transition (CT) and all others are satellite transitions (ST).

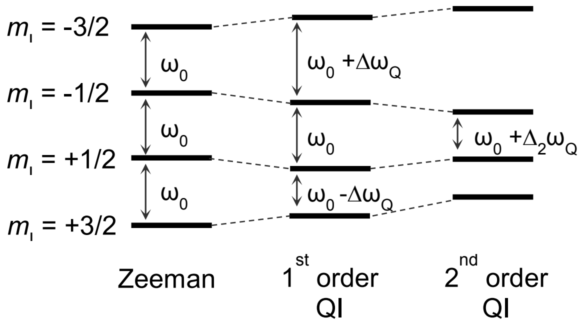

Figure 15. The energy levels of spin I = 3/2 nuclei under Zeeman, first- and second- order quadrupolar interaction (QI).

The first-order quadrupolar interaction affect only satellite transitions while the second-order quadrupolar interaction affect both CT and STs. For this reason, the CT is observed in most of the NMR studies.

In solution, the first-order quadrupolar interaction averages to zero, and has no influence on the frequency of the observed resonances. However, in the solid state, the quadrupolar interaction affect the NMR spectra, and can lead to broadening of powder pattern. The C_Q describes the magnitude of the quadrupolar interaction and determines the breadth of the NMR pattern, while η_Q has influence on its shape. The effect of C_Q and η_Q on static ssNMR powder pattern is shown in Figure 16.

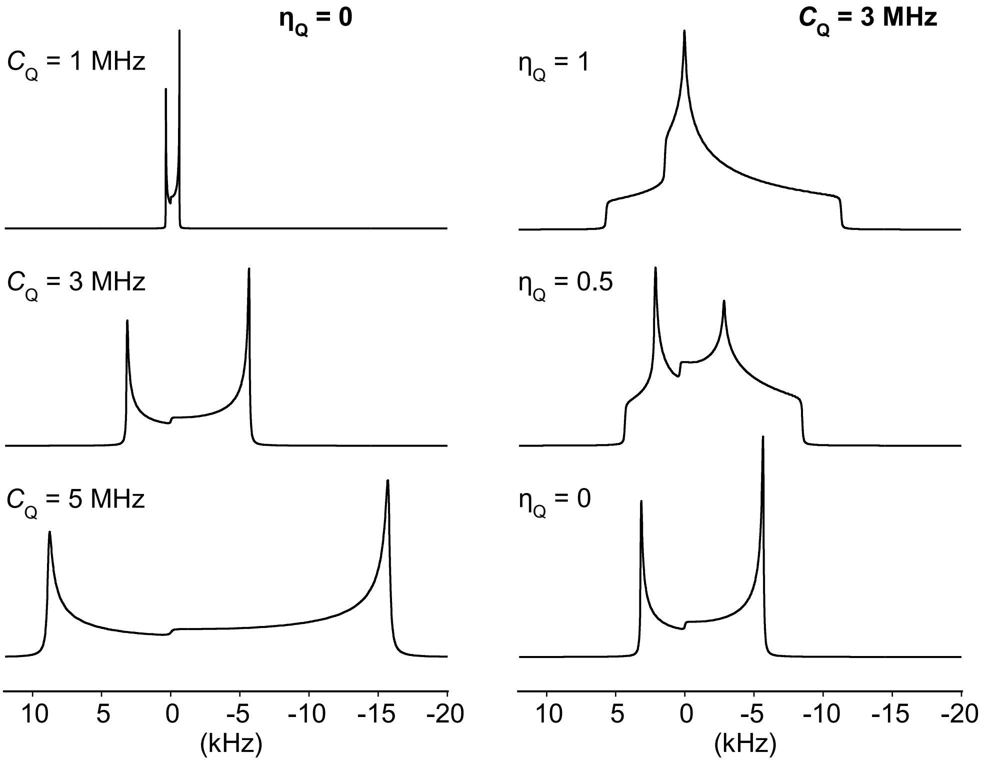

Figure 16. The effect of C_Q and η_Q on static ssNMR powder pattern

3.3 Solid-State NMR Techniques

Depending on the nuclear spin I responsible for the magnetic dipole moment, different line narrowing techniques are required to obtain highly resolved solid-state NMR spectra of zeolites. In the case of spin $I = 1/2$, the application of the conventional magic angle spinning (MAS) technique leads to an averaging of the most important nuclear interactions, such as anisotropic chemical shielding and dipolar interactions. Isotopes with nuclear spin $I > 1/2$ are additionally characterized by an electric quadrupole moment. These nuclei are involved in quadrupolar interactions and often require more sophisticated solid-state NMR techniques, such as high-field MAS NMR, and multiple-quantum magic angle spinning (MQMAS) NMR spectroscopy making their investigation complicated.[45] Hereafter, ssNMR techniques employed in this work are described.

3.3.1 Magic Angle Spinning (MAS)

The most important technique for averaging nuclear interactions in solids, i.e., for the narrowing of solid-state NMR signals, is magic angle spinning (MAS). This experimental technique was introduced in 1958 by Andrew et al.[49] In MAS, the sample is spun rapidly around an axis in an angle θ_m to the external magnetic field $\mathbf{B}_0$ (Figure 17). The maximum line narrowing effect is reached for the "magic" angle of $\theta_m = 54.74°$.

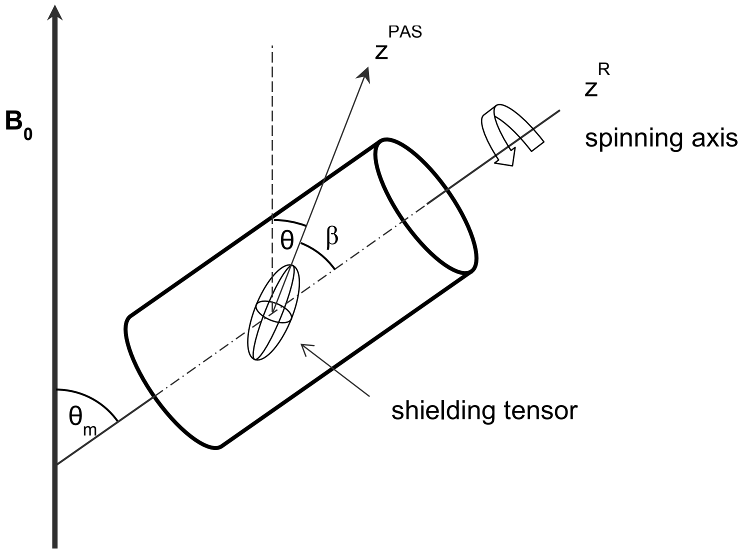

Figure 17. Position of CS tensor and NMR rotor during MAS experiment

The principle of MAS is that first-order interaction Hamiltonians (CS, dipolar and quadrupolar) contain the geometric term ($3\cos^2\theta - 1$), where θ is the angle between the z-axis of NMR interaction tensor and the static magnetic field $\mathbf{B}_0$. If we spin the sample, the orientation of the tensor with respect to the magnetic field varies with time and the average of ($3\cos^2\theta - 1$) becomes:

$$\langle 3\cos^2\theta - 1\rangle = \frac{1}{2}(3\cos^2\theta_m - 1)(3\cos^2\beta - 1)$$

where the angles θ_m and χ are defined in the Figure 17. If we set θ_m to 54.74°, then ($3\cos^2\theta_m - 1) = 0$, and so the average $<3\cos^2\theta - 1>$ is also zero. Therefore, if the spinning rate is fast so that θ is averaged rapidly compared with the anisotropy of interaction, then the first-order NMR interactions are averaged to zero.

CSA can be averaged out completely by MAS when the spinning speed is larger around a factor 3 or 4 than the CSA measured in Hz. In this case, only the isotropic peak is observed. However, when the spinning speed is slower, the NMR pattern will be divided into spikelets known as spinning sidebands. They are set at distances equal to the spinning frequency and radiate out from the line at isotropic chemical shift. Spinning sidebands arise because of the refocusing of the magnetization after each rotor period. After the dephasing of the magnetization, the spins go back to their original positions after each rotor cycle leading to the formation of what are called “rotational echoes” in the frequency spectrum.

Both homonuclear and heteronuclear dipolar interactions can be completely averaged to zero by MAS provided that the spinning frequency is larger than the strength of the dipolar coupling.

In the case of quadrupolar interactions, the first-order Hamiltonian, $\hat{H}_Q{}^1$, contains only the geometric term $(3\cos^2\theta - 1)$ that can be averaged by MAS, while a significant residual line broadening remains due to the second-order quadrupolar effect on central transition. The second-order Hamiltonian, $\hat{H}_Q{}^2$, contains three polynomials of which only two can be averaged by MAS. The third polynomial contains geometric term $(35\cos^4\theta - 30\cos^2\theta + 3)$, which can only be zero either at 30.56° or at 70.12°. Thus, there is not a single value of θ which averages all terms to zero simultaneously, therefore, the linewidth of quadrupolar powder pattern can be reduced under MAS, but an anisotropic powder pattern remains.

Nowadays, the fast spinning of samples is performed using small turbines with gas bearing systems and rotors consisting of zirconia tubes. Standard MAS NMR probes reach sample spinning rates of 5-40 kHz using rotors with outer diameters of 7.0-2.5 mm. Recently, spinning rates above 100 kHz can be reach using special probes and 0.7 mm o.d. rotors.

3.3.2 Heteronuclear Decoupling

Single pulse excitation of nucleus under study represents a basic NMR technique (see Figure 18). The rf pulse (p_1) excites the spin S nuclei, which relax during acquisition time (τ_{ac}). Precession of the nuclear spin induces oscillating voltage, giving an NMR signal as the exponentially decaying sine wave termed free-induction decay (FID). After the rf pulse, the nuclear spins do not return to equilibrium instantly, but relax according to a time constant T_1, which depends on the nucleus, its environment, temperature, etc. Therefore, relaxation delay d_1 (longer than T_1) have to be applied prior to the next scan. Typically, ten to thousand scans have to be applied to get signals with high signal to noise ratio. In some cases, sensitivity can decrease, when less abundant spin *S* nucleus under study is coupled with spin *I* nucleus. To increase signal intensity nucleus *I* is irradiated by broad rf pulse to be decoupled from spin *S* nucleus. The scheme of high power decoupling pulse sequence (hpdec) with single pulse excitation of nucleus *S* and decoupling of spin *I* is shown in Figure 18.

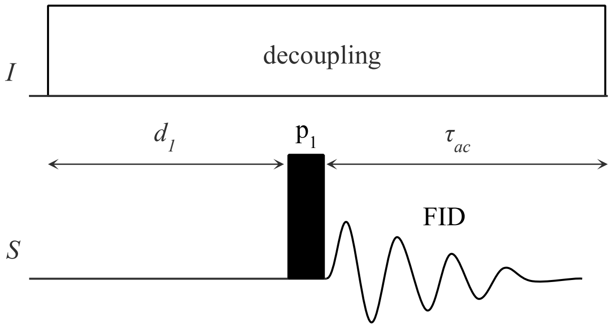

Figure 18. The hpdec pulse sequence with single pulse excitation of nucleus S and decoupling of nucleus I. d_1 - relaxation delay, p_1 – excitation *rf* pulse, τ_{ac} – acquisition time.

3.3.3 Spin-Echo

Broad lineshapes arising from NMR interactions such as chemical shift anisotropy, quadrupolar coupling, etc. have usually rapidly decaying FIDs. Due to the ‘ringing’ in the coil that measures the FID, there is a short period of time after each pulse, when a signal is not detected. When induction decays rapidly, a significant part of the FID is not recorded, leading to severely distorted lineshapes after Fourier transformation. This problem can be overcome using spin-echo pulse sequence (Figure 19) discovered and described by Erwin Hahn[56] in 1950.

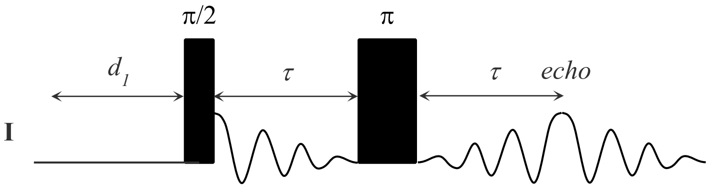

Figure 19. The Hahn-echo pulse sequence

After initial π/2 pulse, magnetization components dephase during the first τ period. The subsequent π pulse rotates the magnetization components 180° about the y axis so the components refocus after a second τ period and start dephasing again. The τ period should be long enough to include the dead time.[54]

3.3.4 Multi-Quantum Magic Angle Spinning (MQMAS)

The two-dimensional echo experiment on half-integer quadrupole spin, which combines the excitation of invisible multiple-quantum transitions with MAS to remove the anisotropic term of the second-order quadrupolar broadening, was introduced by Frydman and Hardwood in 1995.[57,58] This technique is the multiple-quantum (MQ) MAS NMR spectroscopy. In typical MQMAS NMR experiments, a pulse sequence is applied with a strong first pulse, which excites the invisible multiple-quantum coherence. The second pulse and the possibly weaker third pulse convert the coherence back to the observable single-quantum level. The scheme and coherence pathway of z-filtered 3QMAS pulse sequence[59] is shown in Figure 20. Going from the multiple-quantum to the single-quantum level, the sign of the phase development of the coherence is inverted.

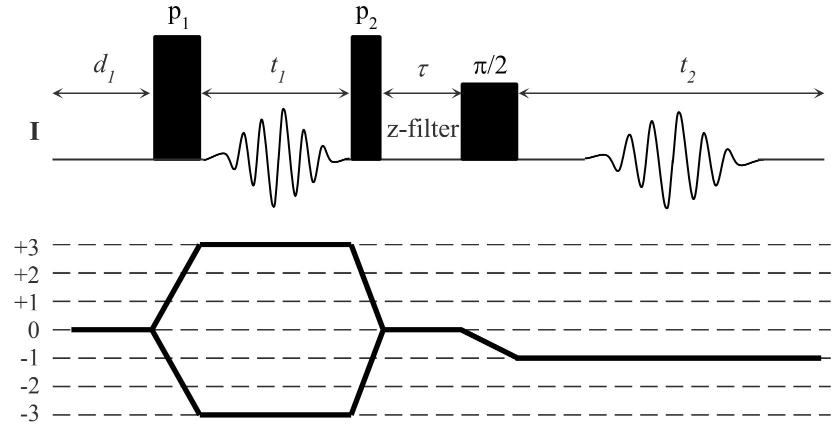

Figure 20. The scheme of z-filtered 3QMAS NMR pulse sequence and coherence transfer pathway. d_1 - relaxation delay, p_1 - excitation pulse, p_2 – conversion pulse, π/2 – selective pulse, τ – z-filter duration, t_2 - acquisition time

The two-dimensional MQMAS NMR spectrum is obtained after a two-dimensional Fourier transformation with respect to t_2 and t_1 leading to the F_2 and F_1 dimensions, respectively. After application of an isotropic shearing transformation, the F_1 projection of the two-dimensional MQMAS NMR spectrum yields signals free of anisotropic broadening. MQMAS

NMR is not quantitative, since the efficiency of the excitation and subsequent conversion of the multi-quantum coherence is heavily influenced by the magnitude of quadrupole interaction, the pulse length and the radiofrequency amplitude.

NMR spectroscopic parameters can be obtained by simulating the lineshape of slices of the F_2 projection[60] or by two-dimensional simulation using special software (e.g. dmfit[61] or SIMPSON[62]), that allows to take the distribution of the interaction parameters into account. The second method is based on a computational estimation of the isotropic chemical shift and the quadrupolar coupling constant via the simultaneous decomposition of both MAS and MQMAS spectra and provides more accurate results when spectrum consists of close overlapping resonances.

3.3.5 Homonuclear correlation experiments

Two-dimensional nuclear magnetic resonance spectroscopy (2D NMR) is a set of nuclear magnetic resonance spectroscopy (NMR) methods which give data plotted in a space defined by two frequency axes. Types of 2D NMR include correlation spectroscopy (COSY), J-spectroscopy, exchange spectroscopy (EXSY), and nuclear Overhauser effect spectroscopy (NOESY). Two-dimensional NMR spectra provide more information about molecules than one-dimensional NMR spectra and are especially useful in determining the structure of a molecule, particularly for molecules that are too complicated to work with using one-dimensional NMR.

Almost all two-dimensional experiments have four stages: the preparation period, where a magnetization coherence is created through a set of RF pulses; the evolution period, a determined length of time during which no pulses are delivered and the nuclear spins are allowed to freely precess (rotate); the mixing period, where the coherence is manipulated by another series of pulses into a state which will give an observable signal; and the detection period, in which the free induction decay signal from the sample is observed as a function of time, in a manner identical to one-dimensional FT-NMR.

In NOESY, the nuclear Overhauser cross relaxation between nuclear spins during the mixing period is used to establish the correlations. The spectrum obtained is similar to COSY, with diagonal peaks and cross peaks, however the cross peaks connect resonances from nuclei that are spatially close rather than those that are through-bond coupled to each other. 2D EXSY NMR provides off-diagonal responses for spins which exchange slowly with one another (either conformationally or chemically). The NOESY and EXSY pulse sequences are identical.

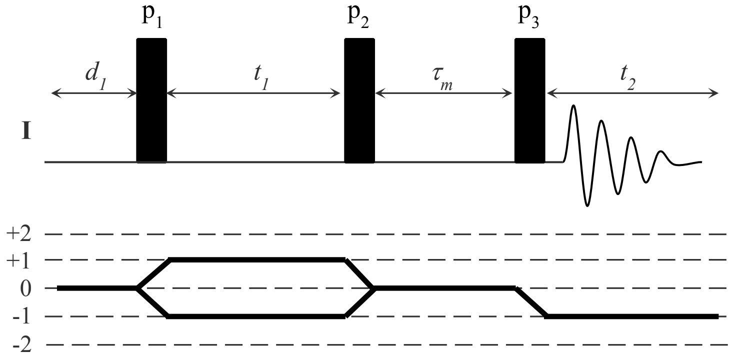

Figure 21. The scheme of 2D EXSY (NOESY-type) pulse sequence and coherence transfer pathway. d_1 - relaxation delay, τ_m – mixing time

3.3.6 Ab Initio NMR Calculations

Simulations of site arrangements using quantum chemistry methods followed by predictions of NMR parameters of the involved atoms represent an essential part of the interpretation of ssNMR spectra as there is not empiric method of the interpretation of the NMR results at an atomic level. Experimental NMR spectra can provide the NMR tensor components; however, they don't provide information about the orientation of these components with respect to molecular structures. A variety of methods, such as Hartree-Fock (HF), density functional theory (DFT) and the gauge-including projector augmented-wave (GIPAW) have been used to predict the NMR tensor parameters.[63,64]

Generally, at first the probable position of given species have to be find (or defined). In the case of Al, the position in given T site is known from XRD measurements. For cations, extra-framework position has to be calculated by molecular dynamics using density function theory (DFT). Subsequently, the local structure of the given species has to be optimized by periodic DFT or in some cases by quantum mechanics/molecular mechanics approach (QM/MM). Afterwards NMR parameters for optimized structure are calculated and therefore individual resonances in the NMR spectrum can by assigned to given species.

3.4 Application of ssNMR for characterization of zeolites

3.4.1 Investigation of Framework Species

For proper characterization of active sites analysis of framework species is necessary since both ^{29}Si and ^{27}Al NMR provides information about distribution and siting of Al in the framework governing derived distribution and siting of extra-framework cations.

3.4.1.1 ^{29}Si NMR

As already mentioned, the basic unit of the zeolite framework is TO_4 tetrahedron with silicon (or aluminium) atom at the central T-position. Some of these T-positions may be occupied by other metal atoms, such as aluminum, boron, gallium, iron, titanium etc. Depending on the amount of metal atoms, which are incorporated in the second coordination sphere of the silicon atoms at T-positions, the SiO_4 units (Q^4) are characterized by up to five different environments denoted as Si(nT) with n = 0, 1, 2, 3, and 4. In the case of aluminum atoms incorporated at T-positions, each type of Si(nAl) species yields a characteristic ^{29}Si MAS NMR signal in a well-defined range of chemical shifts.[65] This allows calculate framework Si/Al ratio and quantify the presence of Al-O-Si-O-Al sequences.

3.4.1.2 ^{27}Al NMR

^{27}Al is half integer nuclei (spin $I = 5/2$) with 100% natural abundance, moderate quadrupolar moment ($Q = 14.66 \times 10^{-30}$ m^2) and good sensitivity. According to Loewenstein's rule,[38] the formation of Al–O–Al bonding in the framework of zeolites is forbidden and exclusively Al(4Si) units exist. Therefore, the ^{27}Al NMR spectra of tetrahedrally coordinated framework aluminum (Al^{IV}) in hydrated zeolites consist, in general, of a single signal in the chemical shift range of 55–70 ppm (referenced to 0.1 M aqueous $Al(NO_3)_3$ solution).[65] Extra-framework aluminum species in hydrated zeolites obtained in result of dealumination by calcination, steaming or acid leaching are octahedrally coordinated aluminum species (Al^{VI}) causing a narrow ^{27}Al NMR signal at around 0 ppm. If extra-framework aluminum species exist as polymeric aluminum oxide in zeolite cages or pores, quadrupolar line broadening may occur owing to distortions of the octahedral symmetry of the AlO_6 units. Broad ^{27}Al MAS NMR signals at 30–50 ppm may be caused by aluminum species in a disturbed tetrahedral coordination (Al^{IV}) or by penta-coordinated species (Al^{V}). Generally, quantitatively reliable ^{27}Al MAS NMR spectra of hydrated zeolites containing framework as well as non-framework aluminum atoms can be obtained in high magnetic fields, with fast magic angle spinning, and using a short excitation pulses.[66]

Significant progress in determining aluminium distribution in silicon-rich matrices was achieved by application of ^{27}Al MQMAS NMR combined with quantum mechanics calculation[39] However, presence of Al-O-(Si-O)$_2$-Al sequences[67] in these materials significantly affects both aluminium geometry and NMR parameters.[68]

3.4.2 Investigation of Extra-Framework Cations

Lithium and sodium are important extra-framework species in zeolites. Solid-state NMR spectroscopy is the suitable method for investigating the distribution and coordination of lithium and sodium cations in zeolites. Although these nuclei have a spin $I > 1/2$ (^{6}Li: spin I = 1; ^{7}Li: spin I = 3/2; ^{23}Na: spin I = 3/2), only the quadrupolar interaction of ^{23}Na nuclei causes a dominating line broadening effect.[45]

3.4.2.1 Lithium ssNMR

Lithium exchanged zeolites represent promising material for CO_2 capture. Thanks to its small diameter it is promising probe for Al siting in zeolites. Both the lithium nuclides ^{6}Li and ^{7}Li are useable for NMR spectroscopy. In the most cases of the investigation of lithium-exchanged zeolites by solid-state NMR spectroscopy, the spin I = 3/2 ^{7}Li nucleus is studied, since it has a significantly higher natural abundance in comparison with the spin I = 3/2 ^{6}Li nucleus (^{6}Li: 7.42%, ^{7}Li: 92.58%) and favorable receptivity. In some cases ^{6}Li spectra can be useful. Because of the weak quadrupole moment of ^{7}Li nuclei ($Q = -4.01 \times 10^{-30}$ m^2), the ^{7}Li MAS NMR spectra of lithium cations in hydrated as well as dehydrated zeolites consist of narrow isotropic lines.[45] However, individual resonances of lithium are in the small range of chemical shifts, making analysis of Li$^+$ siting in Si-rich zeolites with number of distinguishable T-atoms complicated. Thus, it is necessary to setup experiments for maximal possible resolution.

3.4.2.2 Sodium ssNMR

Due to the large quadrupole moment of ^{23}Na nuclei ($Q = 10.4 \times 10^{-30}$m^2),[69] the MAS NMR spectra of sodium cations in dehydrated zeolites are dominated by broad quadrupolar patterns.

The overlap of the ^{23}Na MAS NMR signals of sodium cations located on crystallographically non-equivalent extra-framework positions makes the separation and assignment of the corresponding signals difficult and requires field-dependent experiments[70,71] or application of MQMAS techniques.[21,58,72-74] Utilizing the above-mentioned experimental techniques, the quadrupole coupling constant C_Q, the asymmetry parameter η_Q, and the isotropic chemical shift δ can be obtained.[45]

4 Aim of Study

The aim of this study is to employ techniques of solid-state NMR spectroscopy for analysis of crystallographic positions of extra-framework monovalent cations in zeolites with focus on following objectives:

- Development of methods and methodology to increase the resolution of NMR experiments necessary for the analysis of cation siting in silicon-rich zeolites.
- Verification of reliability of quantum chemical calculation of NMR parameters of non-relativistic nuclei of monovalent cations in cationic sites in zeolites.
- Analysis of siting and coordination of Li^+ and Na^+ ions in zeolite of selected structure.
- Application of monovalent cations monitored by NMR as supplementary method for the analysis of Al siting in silicon-rich zeolites.
- To test possibility of indirect characterization of siting of monovalent cations including “NMR invisible” in zeolites via analysis of local arrangement of framework Al atoms in dehydrated zeolites.

5 Materials and Methods

5.1 Samples

As a model material for testing and verification of methods and procedures suitable for analysis of extra-framework sites in silicon-rich zeolites, FER framework type was chosen. One of the reasons is presence of four framework T sites, which one of the lowest number among silicon-rich structures. Moreover, it is available in a range of Si/Al ratios and it can be synthetized by different routes. In a preliminary study,[75] 5 zeolites of FER structure with different Si/Al were analyzed. Complex multi-spectroscopic approach using ^{29}Si NMR and UV-Vis spectroscopy and ^{27}Al MQMAS NMR interpreted by periodic DFT allowed determination of aluminium siting in the FER framework. Three of them containing mostly isolated Al atom were used for further analysis of extra-framework sites.

To elucidate an effect of cation on ^{27}Al NMR spectra of zeolites, zeolite of CHA framework were investigate, as it contains only one framework T site and low Si/Al ratio allow acquisition of Al NMR spectra in reasonable timescale.

5.1.1 Parent zeolites

The parent FER/20 sample with Si/Al of 20 was purchased from Unipetrol, a.s., Czech Republic (FER/A in Ref.[75]).

The parent FER/27 sample (Si/Al 30), FER/B in Ref.[75]) was synthetized using pure silica (Cab–O–Sil M5), sodium and aluminum sulfate and NaOH. Pyridine served as the structure directing agent.

The parent FER/30 sample (Si/Al 30, FER/C in Ref.[75]) was purchased from Zeolyst International, Inc.

The parent CHA sample with Si/Al of 2.2 was prepared according to the procedure described in Ref.[76]

5.1.2 Cationic forms of zeolites

The parent samples were ion-exchanged with 0.5 M NH_4NO_3 twice for 24 hours to obtain the NH_4-forms. Then the NH_4-forms of parent zeolites were exchanged into the M-CHA (M = Li, Na, and K) and M-FER (M = Li, Na) forms by repeated (3× 24 hours) M^+ ion-exchange using 0.5 M solution of MNO_3 (50 ml per 1 g of a zeolite) at 70°C for Li^+ and at room temperature for Na^+ and K^+. Subsequently, samples were filtered, thoroughly washed with distilled water and then equilibrated on air at room temperature to guarantee their full hydration.

5.1.3 Dehydration

For analysis of cations in extra-frameworks positions, cationic forms of zeolites were dehydrated to enable coordination of cations to the zeolite framework. Prior to the dehydration, hydrated samples were packed into the ZrO_2 MAS NMR rotors and dried overnight in the oven at 100 °C to remove excess water. The dehydrated samples for the NMR experiments were prepared *"in situ"* using instrumental setup developed in this work to allow dehydration and subsequent sealing of the cooled samples in NMR rotors under vacuum. Samples were dehydrated at 450°C under dynamic vacuum of $p = 1.10^{-1}$ Pa for 3 hours with a heating ramp of 3°C min^{-1}. Subsequently to the dehydration, the samples were cooled down at room temperature and airtight-sealed with Kel-F cups. Sealed rotors were immediately transferred into the glass tubes, which were evacuated and heat-sealed to prevent rehydration of the samples before NMR measurements.

5.2 Solid-State NMR experiments

Solid-state NMR experiments were carried out in the Joint Laboratory of Solid-State NMR, Institute of Macromolecular Chemistry, AS CR and Jaroslav Heyrovský Institute of Physical Chemistry, AS CR on a Bruker Avance III HD 500 WB/US three-channel NMR spectrometer equipped with a wide bore ultra-stabilized magnet charged to 11.7 T ($\nu_0(^1H) = 500$ MHz) adapted for measuring of high resolution NMR spectra of solid samples. An external cooling unit and set of NMR probe-heads allow performing NMR experiments under wide range of experimental conditions. In this work, solid state NMR spectra were measured using either 4 mm (PH MAS WVT 500 WB BL4 N-P/H-F CP/MAS) or 3.2 (PH MAS WVT 500 WB BL3.2 N-P/H-F CP/MAS) double resonance probe-heads. Samples packed in the ZrO_2 rotors with outer diameter of either 4 mm or 3.2 mm and sealed with Kel-F caps were spun under magic angle at spinning frequencies of 7-22 kHz.

A set of dehydrated Na-FER samples were measured on a Bruker Avance II 4-channel NMR spectrometer equipped with a narrow bore ultra-stabilized 21.1 T ($\nu_0(^1H)$ = 900.08 MHz) magnet using a 4 mm double-resonance MAS probe-head (Bruker, 4 mm, 18 kHz MAS, 1H/13C/15N, CP/MAS, VT) at the National Ultrahigh-Field NMR Facility for Solids in Ottawa, Canada.

Analytical simulations of NMR spectra were performed using dmfit[61] program. This program allows modeling of powder patterns of a broad range of NMR active nuclei in various types of experiments using a set of model functions and thus allows obtaining NMR parameters of individual resonances. Details of particular simulations are described and discussed in Chapter 6.

5.2.1 Lithium ssNMR

^{6}Li ssNMR experiment was carried out at Larmor frequency $\nu_0(^6Li)$ = 73.6 MHz in 3.2 mm double-resonance MAS probe at spinning frequency ν_{rot} = 20 kHz. The one-dimensional ^{6}Li MAS NMR spectrum was acquired using one pulse sequence with a proton decoupling. Experiment was conducted with an excitation pulse width of 2.4 μs, a recycle delay of 30s and number of scans of 1844.

^{7}Li ssNMR spectra were acquired at Larmor frequency $\nu_0(^7Li)$ = 194.37 MHz using either a 4 mm or a 3.2 mm double-resonance MAS probes at spinning frequencies of ν_{rot} = 12 kHz and ν_{rot} = 20 kHz, respectively.

The one-dimensional ^{7}Li MAS NMR spectra were acquired using either the Hahn-echo sequence or one pulse sequence with an optional proton decoupling. For Hahn-echo sequence, an optimized selective $\pi/2$ pulse width of 2.9 μs followed by π pulse delayed by 6 μs was applied. The number of scans was set to 64. For one pulse sequence with an optional proton decoupling (hpdec), an excitation pulse widths ranging from 0.8 to 2.9 μs were applied. The number of scans ranged from 16 to 512. In all one-dimensional ^{7}Li MAS NMR experiments, recycle delay of 4 s, spectral width of 39 kHz and transmitter frequency offsets of 9 kHz was set.

The two-dimensional single quantum ^{7}Li 2D EXSY MAS NMR spectra were recorded using the NOESY-type three-pulse sequence with $\pi/2$ pulse widths of 2.9 μs. Duration of the spin-exchange period between the second and third pulse ranged from 10 μs to 100 ms. Spectral width in both frequency dimensions was rotor-synchronized to be 15-22 kHz. The transmitter frequency offsets were set to 9 kHz. The indirect detection period t1 ranged from 320 to 1024 increments, each made of 8-40 scans.

The ^{6}Li and ^{7}Li chemical shifts were referenced externally to a 1M solution of LiCl (δ_{iso} = 0.0 ppm) by using a signal of solid LiCl at -1.04 ppm.

5.2.2 Sodium SSNMR

Experiments at 11.7 T. ^{23}Na NMR spectra were acquired at Larmor frequency $\nu_0(^{23}Na)$ = 132,3 MHz using either a 4 mm double-resonance MAS probe or a 3.2 mm double-resonance MAS probe at spinning frequencies of ν_{rot} = 12 kHz and ν_{rot} = 20 kHz, respectively.

The one-dimensional ^{23}Na MAS NMR single pulse spectra were collected using hpdec pulse sequence with a single pulse excitation and high power proton decoupling. An optimized pulse width ranging from 2.3 μs to 4.4 μs and recycle delay of 4 s were used with number of scans ranging from 2560 to 3072 and spectral widths ranging from 40 to 55 kHz.

The two-dimensional ^{23}Na MQMAS NMR spectra were recorded using three-pulse z-filtered sequence with selective, excitation and conversion pulse widths of 6.8, 2.1 and 35 μs for 4 mm probe and 5, 2 and 18 for 3.2 probe, respectively. Number of increments in indirect dimension was set to 254 each made by 1024-2048 scans.

Experiments at 21.1 T. ^{23}Na NMR spectra were measured at Larmor frequency $\nu_0(^{23}Na)$ = 238,1 MHz using a 4 mm double-resonance MAS probe. Dehydrated samples were spun in 4 mm o.d. ZrO_2 rotors at frequency ν_{rot} = 10 kHz.

The one-dimensional ^{23}Na MAS NMR single pulse spectra were collected after 2048 scans using a single pulse excitation with optimized pulse width of 1 μs and relaxation delay of 1 s.

The two-dimensional ^{23}Na MQMAS NMR spectra were recorded using three-pulse z-filtered sequence with selective, excitation and conversion pulse widths of 5.2, 2.1 and 20 μs, respectively. Number of increments in indirect dimension was of 512, each made by 576 scans.

The ^{23}Na chemical shifts were referenced externally to 1M solution of NaCl (δ_{iso} = 0.0 ppm) by the signal of a solid NaCl at 7.2 ppm.

5.2.3 Aluminium ssNMR

^{27}Al MAS NMR single pulse spectra were recorded using hpdec pulse sequence with a $\pi/12$ excitation pulse of 0.8 μs and a 2s repetition delay at the rotation frequency of 12 kHz and 20 kHz for the hydrated and dehydrated samples, respectively. A low temperature experiment with the K-CHA sample was performed at temperature of 190 K employing an attached external cooling unit.

The two-dimensional triple-quantum ^{27}Al 3Q MAS NMR spectra of the dehydrated M-CHA samples were recorded using a three-pulse sequence with excitation, conversion, and selective pulse lengths of 4.2, 1.5, and 43 μs respectively. The conversion and selective pulses were spaced using a *z*-filter of 20 μs in length. The rotation frequency was of 20 kHz.

The ^{27}Al chemical shifts are referenced to the 1M solution of $Al(NO_3)_3$ in D_2O (δ_{iso} = 0.0 ppm)

6 Results and Discussion

6.1 Lithium ssNMR of Li-FER samples

6.1.1 ^{6}Li and ^{7}Li MAS NMR Experiments

To investigate lithium environment in three dehydrated Li-FER samples ^{7}Li MAS NMR experiments were conducted using a single-pulse excitation with proton decoupling during data acquisition (hpdec pulse sequence). Resulting spectra collected using the calibrated 90° pulse, under MAS rate of 11 kHz, are shown in Figure 22. Temperature of the samples was of 303 K, due to the friction heating. An excellent signal to noise ratio was achieved after 8 minutes and 128 scans.

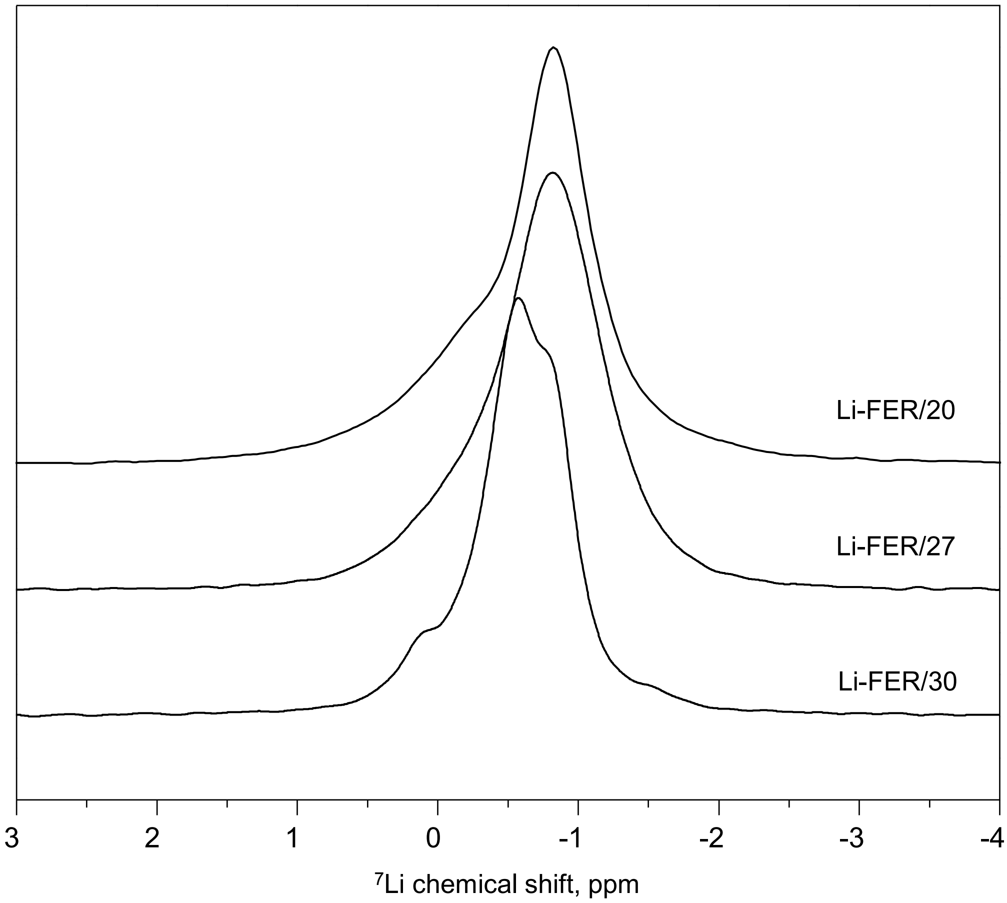

Figure 22. ^{7}Li MAS NMR spectra of dehydrated Li-FER samples, $\nu_{rot} = 11$ kHz, T = 303 K

It is clearly visible that the spectra consist of at least two overlapping resonances at approximately -0.2 ppm and -0.8. The differences between the spectra evidence presence of several distinguishable Li^+ cations in the samples reflecting different siting of Al atoms in the framework T sites. However, a detailed analysis of these spectra is limited due to the narrow range of the ^{7}Li chemical shifts (ca. 2 ppm) of overlapping resonances and relatively low resolution of ^{7}Li MAS NMR spectra with respect to width of signals. In the attempt to increase spectral resolution ^{7}Li MAS MAS experiment with Hahn-echo pulse sequence was performed on the sample Li-FER/20 under the same conditions as hpdec spectra. Spectrum is shown and compared with hpdec ^{7}Li MAS NMR spectrum in Figure 23.

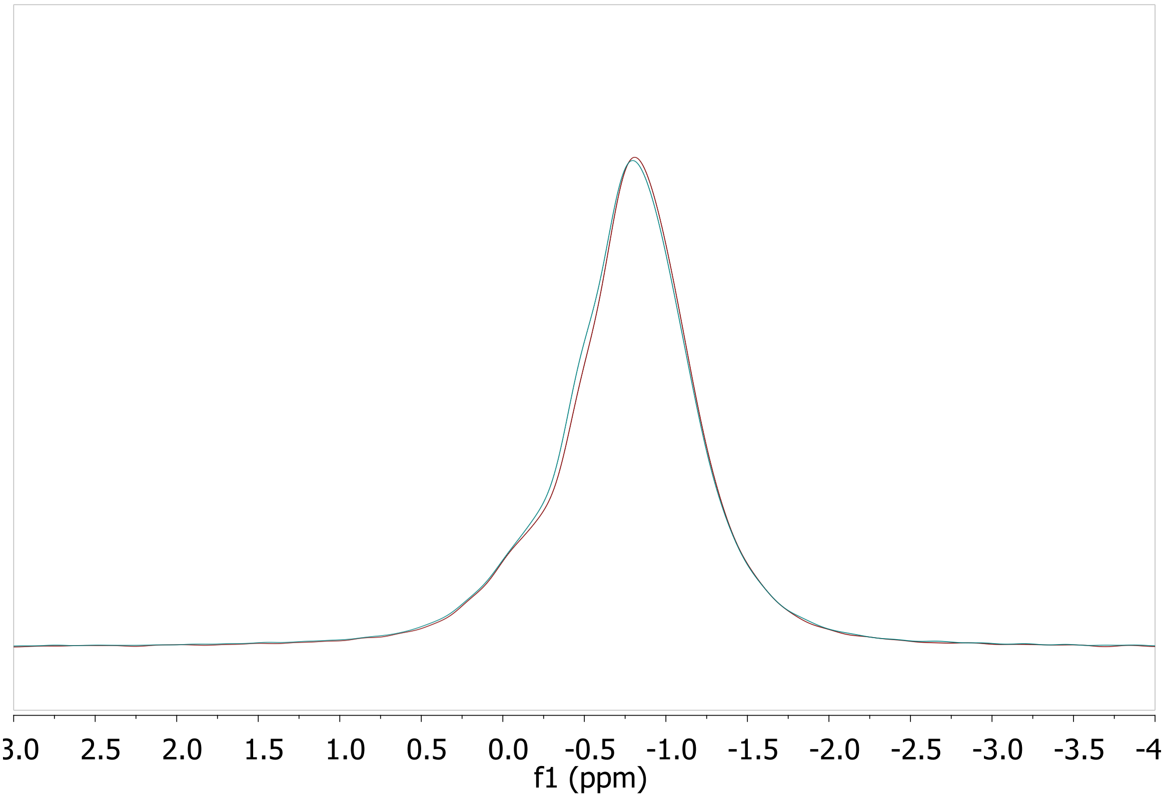

Figure 23. Comparison of 1D ^{7}Li MAS NMR pulse sequences. Hpdec (green), Hahn-echo (brown)

It is clearly visible that there is no remarkable improvement on the resolution of the ^{7}Li MAS NMR spectra using Hahn-echo and both pulse sequences provide the same results. For further investigation of lithium we focus on ^{6}Li nuclide. Comparisons of ^{6}Li and ^{7}Li hpdec MAS NMR spectra of Li-FER/20 sample acquired at the same conditions are shown in Figure 24.

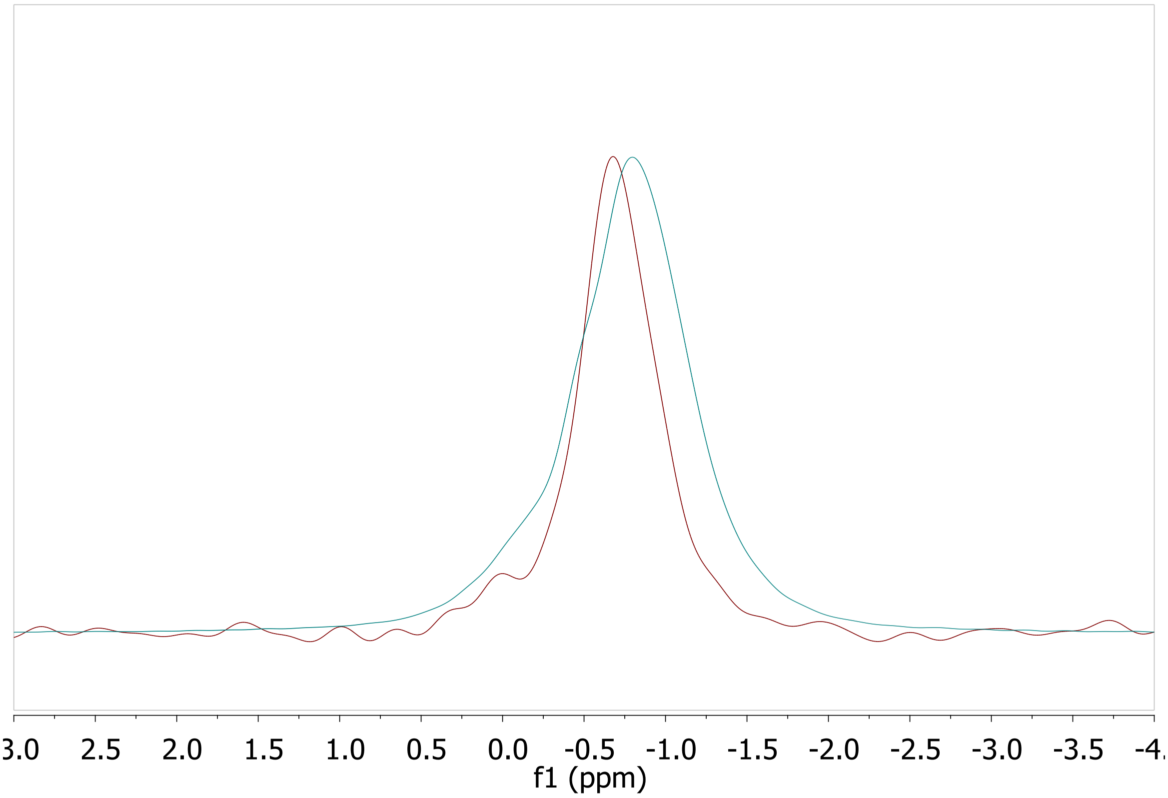

Figure 24. Comparison of ^{6}Li (brown) and ^{7}Li (green) hpdec MAS NMR spectra

^{6}Li pattern exhibits similar featurures as ^{7}Li pattern, i.e. main peak from -0.5 to -1.0 ppm with shoulder on the left. One can observe ^{6}Li pattern breadth is smaller than ^{7}Li pattern and the maximum is shifted to the left of about 0.2 ppm. Subtle differences between ^{6}Li and ^{7}Li chemical shifts of the same chemical entities are common and reported e.g. by Gee et al.[77] The fact, that the main peak is not symmetrical confirms presence of multiple overlapping resonances, bun resolution is not sufficient to resolve them. Moreover, due to the low natural abundance of ^{6}Li nuclide and low concentration of Li in the sample, ^{6}Li experiment suffers by enormous acquisition time of 18 hours and low signal to noise ratio of 50, in contrast to ^{7}Li experiments with acquisition time of 8 minutes and signal to noise ratio of 1000. Therefore, ^{7}Li MAS NMR experiment with hpdec sequence revealed to be the most suitable method for acquisition of one dimensional quantitative spectra of Li-FER. In next steps, effect of rotation frequency and temperature on hpdec ^{7}Li MAS NMR spectrum was studied on the sample FER/20 (Figure 25 and Figure 26, respectively).

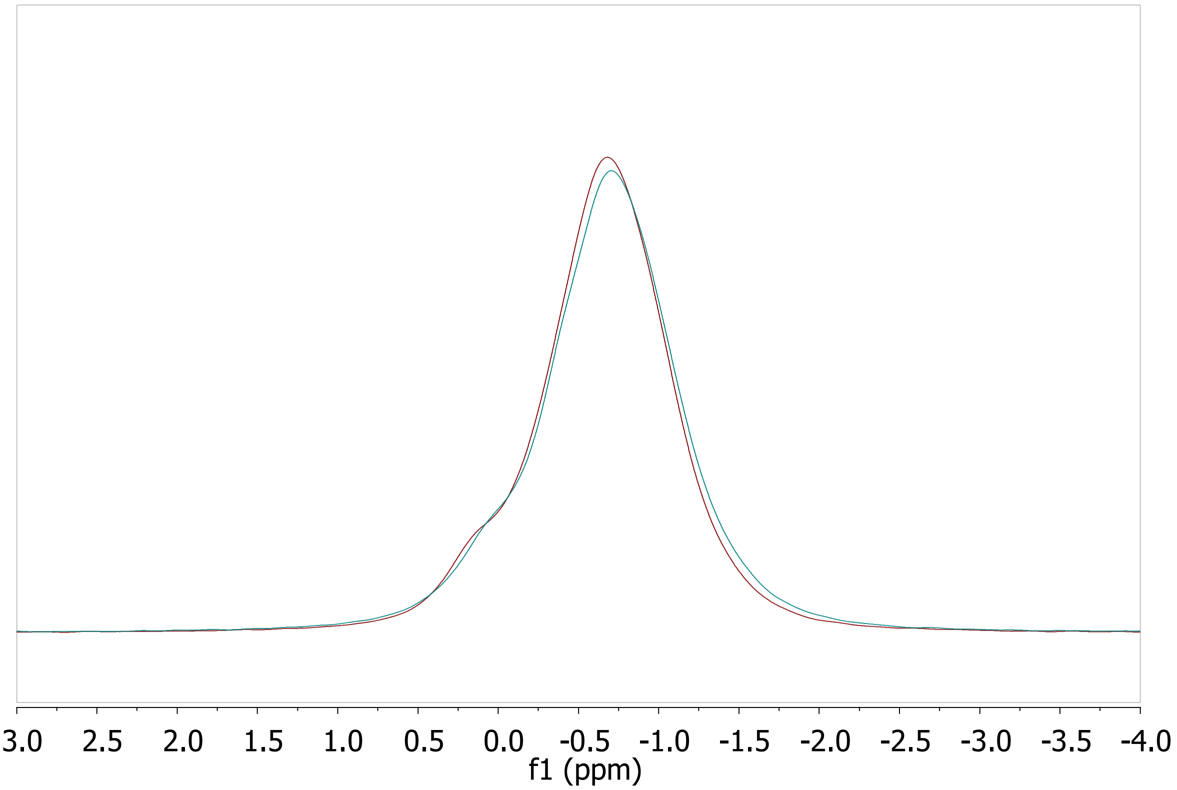

Figure 25. Effect of spinning frequency on ^{7}Li hpdec MAS NMR: 11 kHz (green), 20 kHz (brown)

Only subtle changes of the spectrum can be observed during rotation of the sample at different frequencies and. More pronounced effect can be seen with change of the temperature (Figure 26). Broadening of the powder pattern recorded at 260 K can be explained by a systematic linear change of chemical shifts of individual resonances.

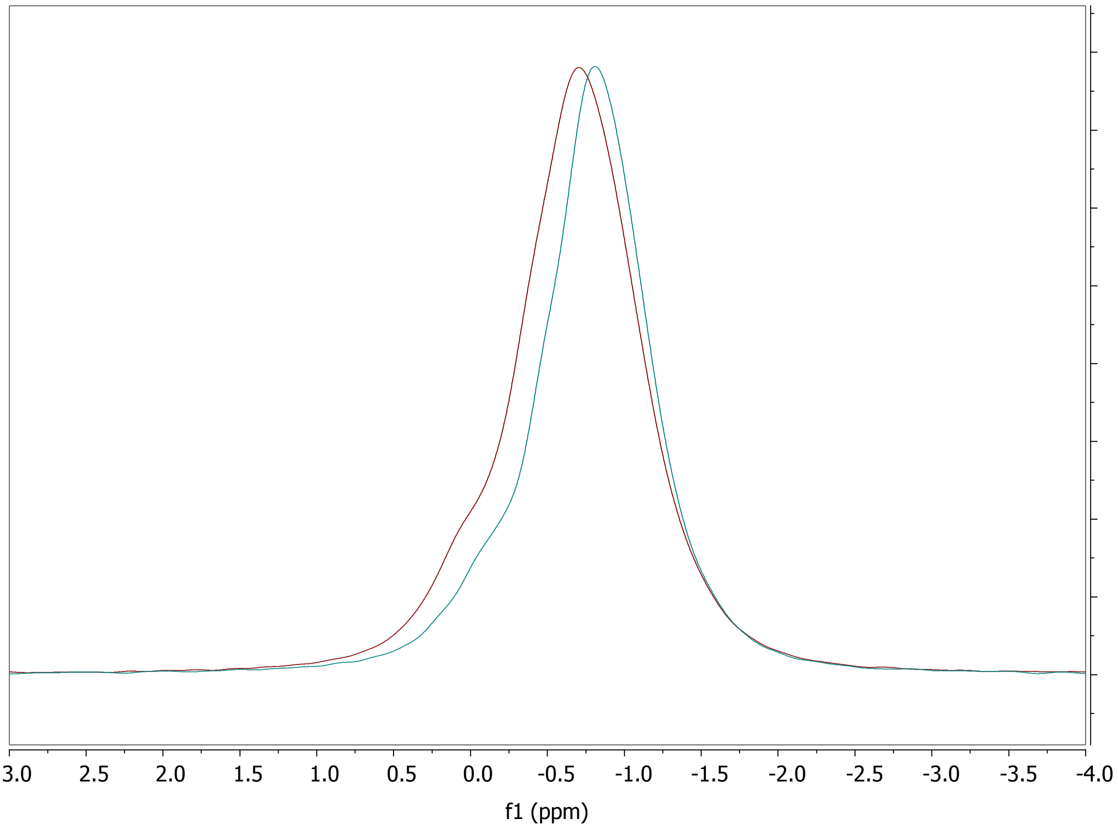

Figure 26. Effect of temperature ^{7}Li hpdec MAS NMR: 303 K (green), 260 K (brown)

All one dimensional experiments performed indicate presence of multiple overlapping resonances without observable quadrupolar broadening. As the best options reveals to be ^{7}Li hpdec MAS NMR experiment at temperature of 260 K and spinning rate of 20 kHz. However, the spectral resolution on given instrumentation is not sufficient to provide their proper identification and more complex approach has to be developed.

6.1.2 2D ^{7}Li-^{7}Li Correlation NMR Experiments

For better resolution and identification of close lithium resonances and thus more detailed analysis of lithium siting, two dimensional homo-nuclear ^{7}Li 2D EXSY NMR experiment using NOESY-type pulse sequence was employed. For this purpose MQMAS cannot be used due to the negligible quadrupolar broadening. Better resolution of individual resonances in 2D EXSY NMR spectrum is achieved by diagonal position of peaks and by presence of cross-peaks of correlating resonances. ^{7}Li 2D EXSY NMR spectra of sample Li-FER/20, recorded with t_1 spin-exchange period of 1, 10 and 50 ms are shown in Figure 27. Acquisition time of single ^{7}Li 2D EXSY NMR NMR experiment was of approximately 5 hours.

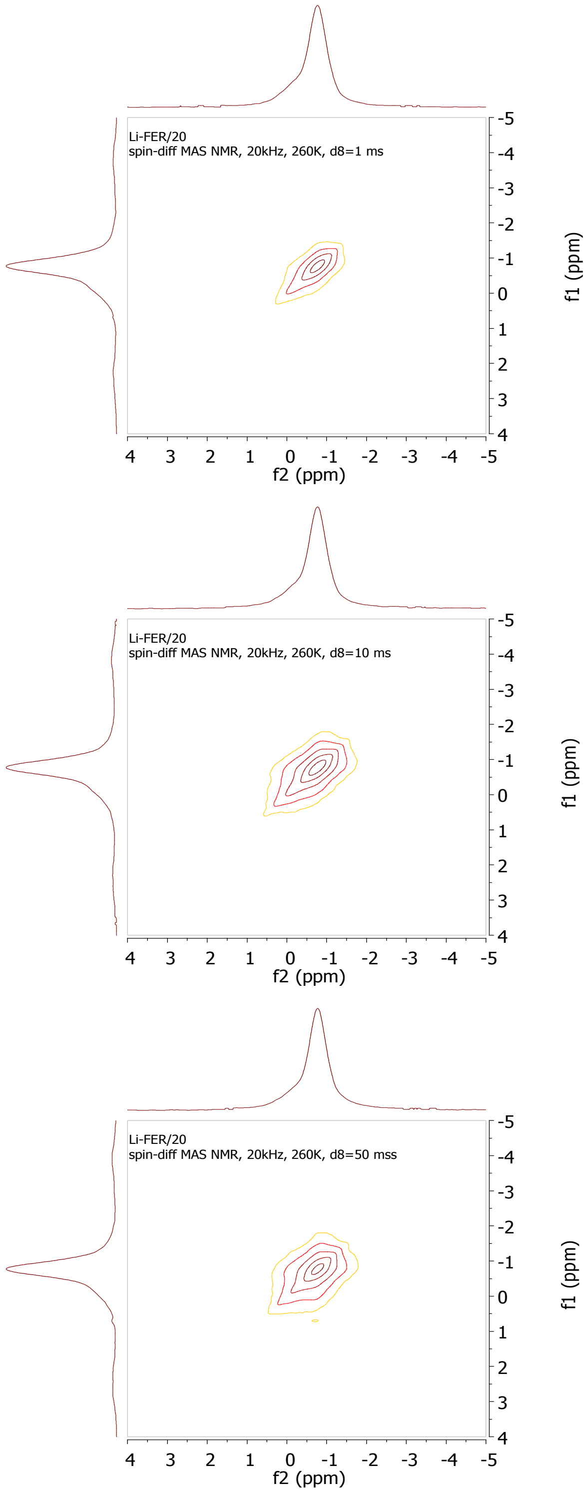

Figure 27. ^{7}Li 2D EXSY NMR spectra of sample Li-FER/20 with spin-exchange period of 1 ms (top), 10 ms (middle) and 50 ms (bottom)

With increasing spin-exchange period a 2D lineshape of ^{7}Li-^{7}Li correlation spectrum becomes "wider". It indicates stronger magnetization transfer between Li nuclei in spatial proximity during longer spin-exchange period. Although cross-peaks are not fully resolved, due to the low concentration of lithium in the sample, the analysis of the 2D signal indicates their positions and thus positions of correlating diagonal peaks. ^{7}Li 2D EXSY NMR spectra of samples Li-FER/20, Li-FER/27 and Li-FER/30 recorded with spin-exchange period of 10 ms are shown in Figure 28, Figure 29 and Figure 30, respectively.

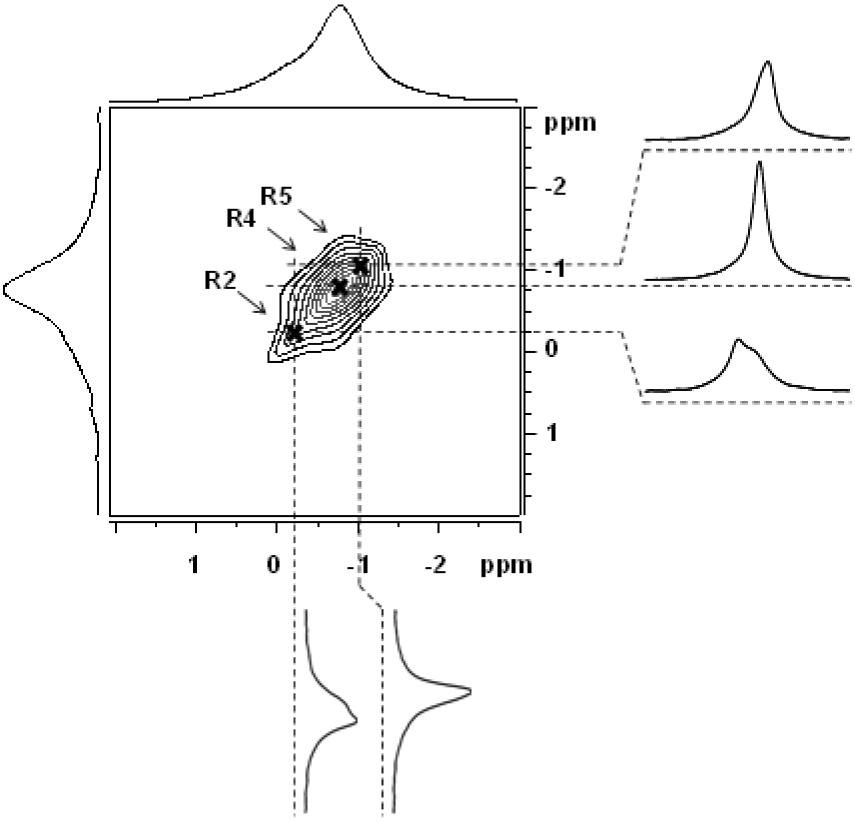

Figure 28. ^{7}Li 2D EXSY NMR spectrum of sample Li-FER/20 with spin-exchange period of 10 ms with skyline projections, selected cross-sections and marked resonances[78]

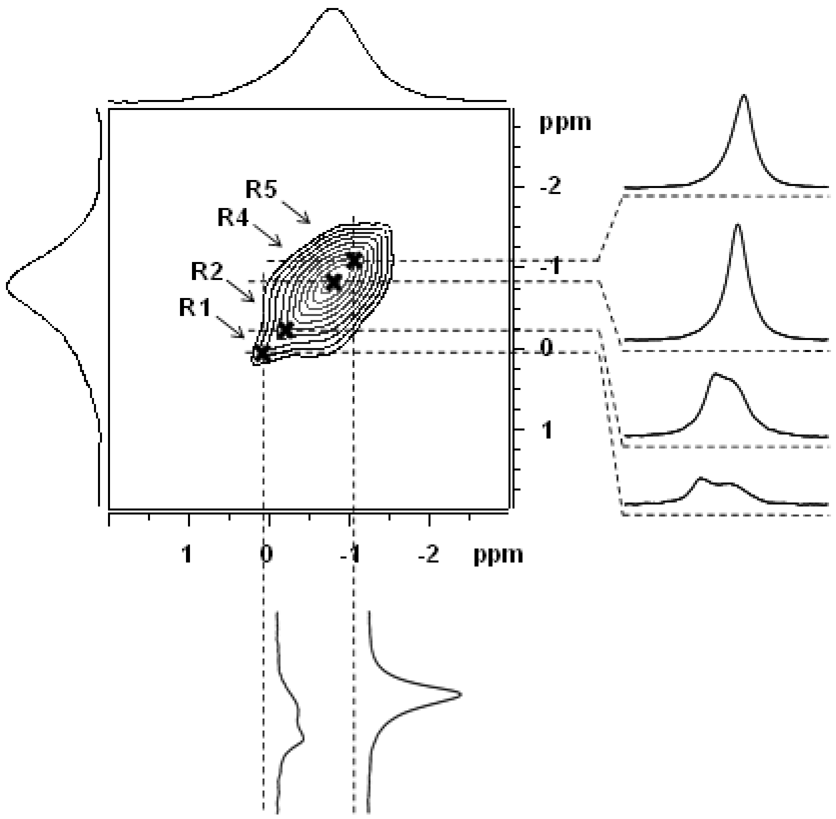

Figure 29. ^{7}Li 2D EXSY NMR spectrum of sample Li-FER/27 with spin-exchange period of 10 ms with skyline projections, selected cross-sections and marked resonances[78]

Different shape of the spectra indicates different positions of Li resonances and proves a hypothesis that ^{7}Li spectra consist of more than two resonances. Careful and detail inspection of non-diagonal cross-peaks in the 2D projection of the ^{7}Li-^{7}Li correlation experiments allows the estimation of the number of ^{7}Li NMR resonances and their ^{7}Li chemical shifts.

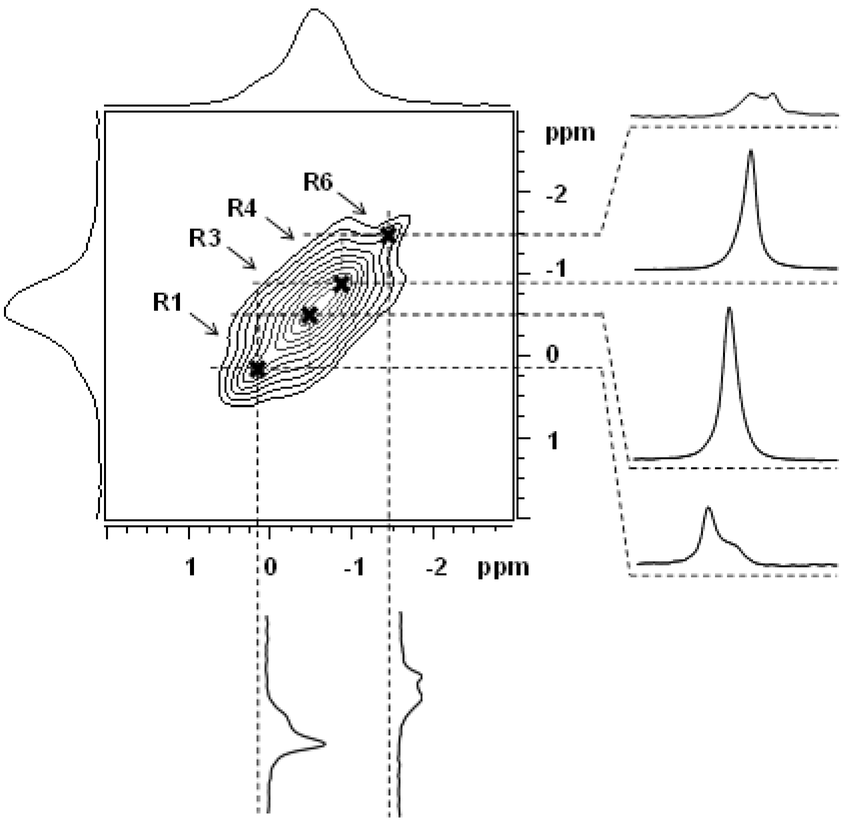

Figure 30. ^{7}Li 2D EXSY NMR spectrum of sample Li-FER/30 with spin-exchange period of 10 ms with skyline projections, selected cross-sections and marked resonances[78]

Six distinguishable resonances, denoted here as R1-6 (with chemical shift descending from the most positive value of R1 to the most negative value of R6), were identified in the ^{7}Li 2D EXSY NMR spectra of the Li-FER samples. Three resonances were found in ^{7}Li-^{7}Li correlation spectra of the sample Li-FER/20 and four in both Li-FER/27 and Li-FER/30. Isotropic chemical shifts of individual lithium resonances obtained from analysis of ^{7}Li-^{7}Li correlation MAS NMR spectra are summarized in Table 1.

6.1.3 Quantitative analysis of Li^{+} distribution

Correlation experiments do not provide quantitative results due to the non-homogenous transfer of magnetization during spin-exchange period. For quantitative analysis of Li^{+} distribution simulations of ^{7}Li MAS NMR spectra using isotropic chemical shifts of individual lithium resonances obtained from analysis of ^{7}Li-^{7}Li correlation MAS NMR spectra were performed (see Figure 31).

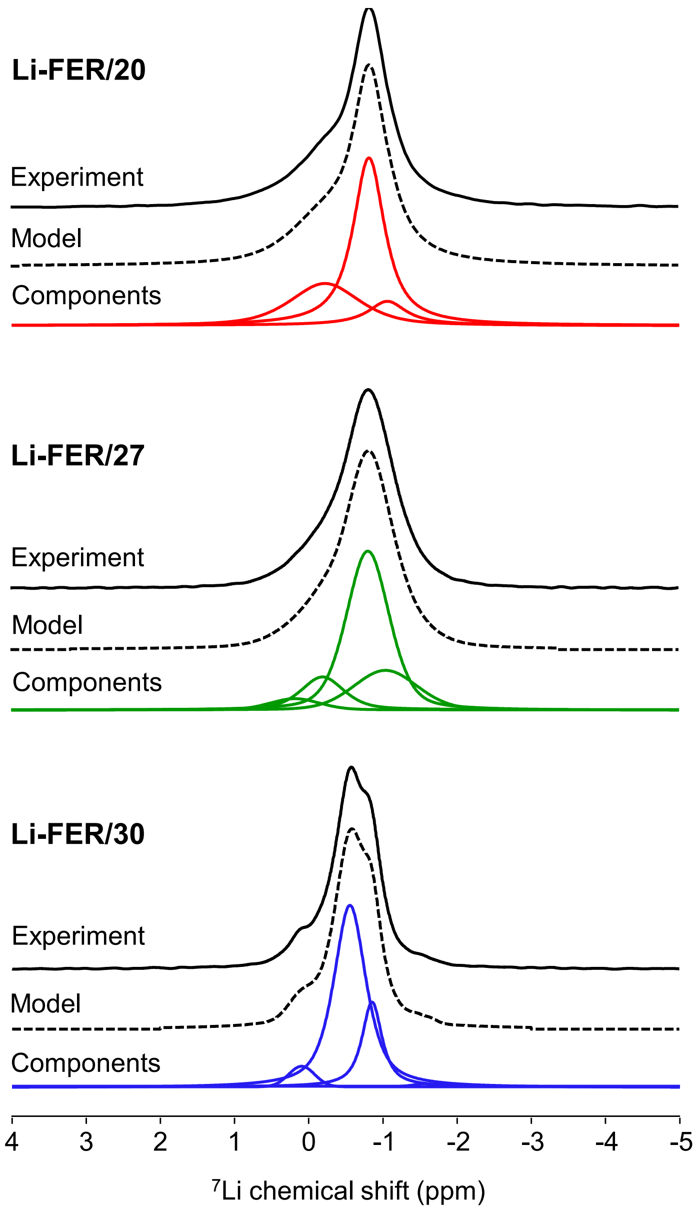

Figure 31. ^{7}Li MAS NMR spectra of Li-FER samples with simulation

Figure 31 clearly demonstrates that simulations using chemical shifts obtained from ^{7}Li-^{7}Li correlation spectra fit perfectly with experimental lineshape. The ^{7}Li chemical shifts of individual lithium resonances and corresponding relative concentration of Li^{+} ions at crystallographically non-equivalent extra-framework positions in Li-FER samples are summarized in Table 1 and graphically displayed in Figure 32.

Table 1. ^{7}Li chemical shift *(δ)* and relative intensity *(I)* of individual Li$^+$ resonances in dehydrated Li-FER samples

sample	^{7}Li NMR resonances											
	R1		R2		R3		R4		R5		R6	
	δ/ppm	*I*/%	*δ*/ppm	*I*/%	*δ*/ppm	*I*/%	*δ*/ppm	*I*/%	*δ*/ppm	*I*/%	*δ*/ppm	*I*/%
Li-FER/20			**-0.23**	40			**-0.80**	50	**-1.07**	10		
Li-FER/27	**0.17**	5	**-0.20**	15			**-0.80**	60	**-1.05**	20		
Li-FER/30	**0.12**	5			**-0.55**	72	**-0.85**	20			**-1.50**	3

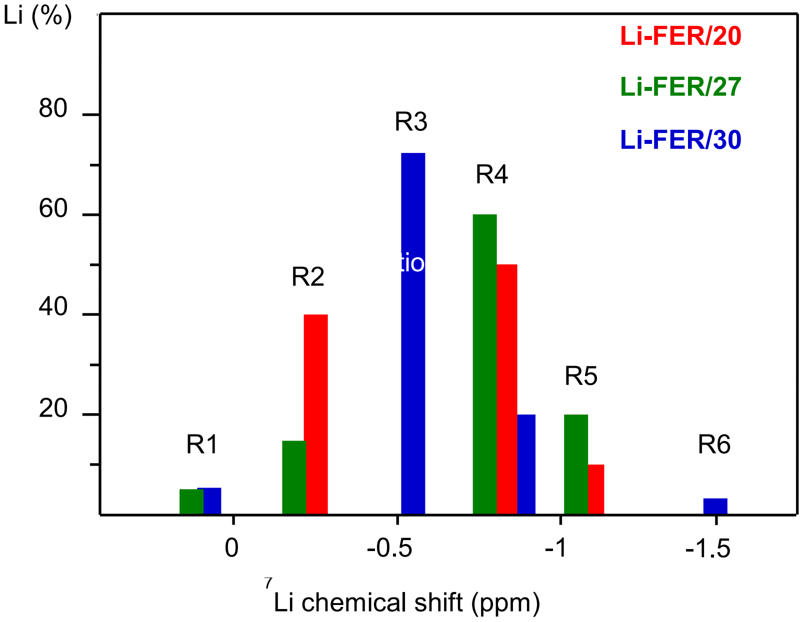

Figure 32. Experimental ^{7}Li chemical shifts and their relative intensities in the spectra of the dehydrated Li-FER samples Li-FER/20 (🟥), Li-FER/27 (🟩), and Li-FER/30

6.1.4 Analysis of Li$^+$ siting

The complexity of the siting of cations in zeolite matrixes and a very high sensitivity of the chemical shift on the local structure of the nucleus environment do not allow empiric or semi-empiric interpretations of MAS NMR spectra of cations in extra-framework positions of zeolites and therefore quantum-chemistry computations are employed. Theoretical computations were made by group of Dr. Štěpán Sklenák (see Ref.[78] for details). Six optimized structures of the low energy Li$^+$ sites (two sites denoted as T1A and T1B for Li$^+$ balancing Al in T1 site, T2A and T2B for Al(T2), T3 for Al(T3), and T4 for Al(T4)) with calculated values of lithium chemical shifts and the relative energies of are shown in Figure 33 and listed in Table 2.

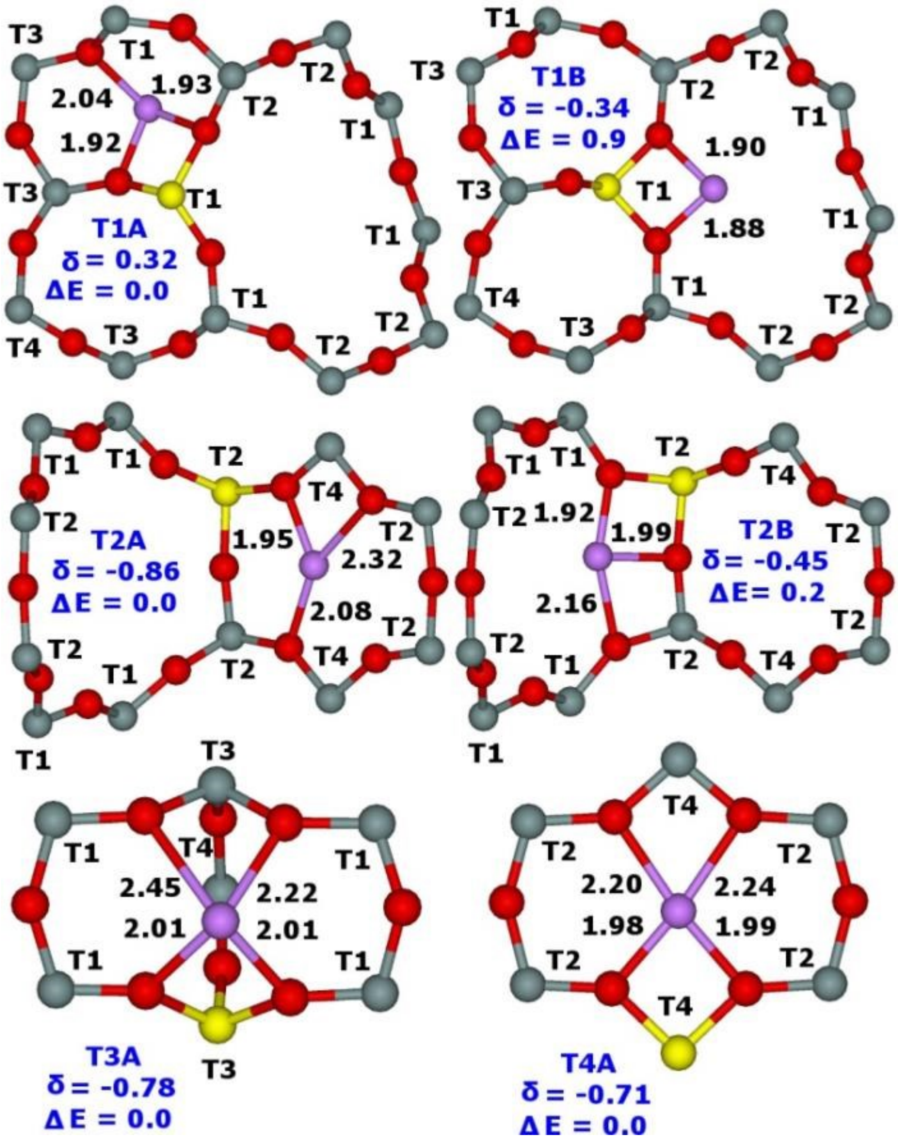

Figure 33. Optimized structures (Li-O distances in Å) with the designations of the T sites of the low energy Li^+ sites, the relative energies in kcal/mol, and the corresponding ^{7}Li chemical shifts in ppm.[7] Silicon atoms are in gray, oxygen atoms in red, aluminum atoms in yellow, and lithium in violet[78]

Table 2. Calculated ^{7}Li chemical shift (δ_{calc}) and relative energies (ΔE) of six optimized low energy Li$^+$ sites

Li$^+$ site	δ_{calc} ppm	ΔE kcal/mol
T1A	**0.32**	0.0
T1B	**-0.34**	0.9
T2A	**-0.86**	0.0
T2B	**-0.45**	0.2
T3	**-0.78**	0.0
T4	**-0.71**	0.0

Figure 34 compares the experimental ^{7}Li chemical shifts with the calculated ones. The patterns of the experimental and predicted ^{7}Li chemical shifts in Figure 34 show significant similarities.

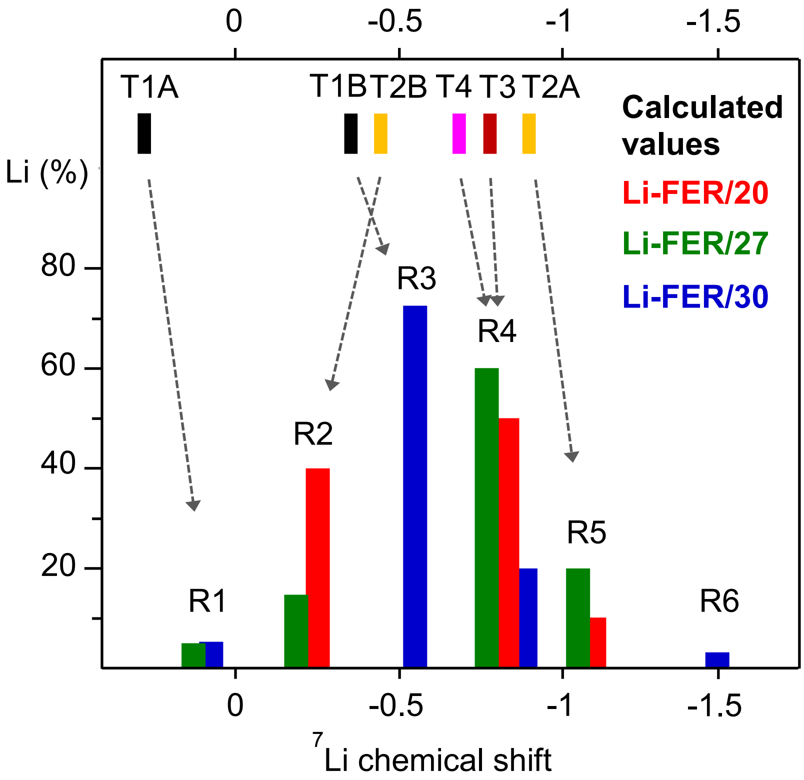

Figure 34. Experimental ^{7}Li chemical shifts of Li$^+$ resonances and their intensities in the spectra of the dehydrated Li-FER samples, ^{7}Li chemical shifts calculated for Li$^+$ ions balancing Al atoms in the T1 – T4 sites, and their assignments to the experimental data. Li-FER/20 (🟥), Li-FER/27 (🟩), and Li-FER/30 (🟦); Li$^+$ balancing Al in the T1 (⬛), T2 (🟨), T3 (🟫), and T4(🟪) sites.

The R5 resonance observed for the Li-FER/20 and Li-FER/27 samples (Table 1) can be safely assigned to the T2A site. Since there are two low energy Li$^+$ sites for Al(T2), the R2 resonance measured for the same samples corresponds to the T2B site. Then, it follows, that the R4 resonance observed in all Li-FER samples belongs to either one of the T3A and T4A sites or to both of them. The calculated ^{7}Li chemical shifts of T3A and T4A are too close to each other to be distinguishable by ^{7}Li MAS NMR spectroscopy. The R1 resonance observed for Li-FER/27 and Li-FER/30 can be safely assigned to the T1A site. There are two more ^{7}Li NMR resonances measured for Li-FER/30 (Table 1). R3 belongs to the T1B site which is the other low energy Li^+ site for Al(T1). Figure 2 shows the assignment of the observed ^{7}Li NMR resonances to the Li^+ sites. The shift deviations are ca ± 0.2 ppm. The remaining very low intensity R6 resonance at -1.50 ppm, which is observed only for Li-FER/30, cannot be assigned to any of the calculated low energy Li^+ sites and its origin is unclear. It can correspond to (i) Li^+ in vicinity of the site formed by close Al atoms, (ii) perturbation of the site by neighbouring defect. The ranges of the observed (without the unassigned R6) and calculated ^{7}Li chemical shifts (1.24 and 1.18 ppm, respectively) are in very good agreement.

There are no experimental data based on diffraction methods regarding the siting of Li^+ in ferrierites. However, the knowledge of the Al siting in the three ferrierite samples used[75] permits a verification of the siting of Li^+ ions obtained in this study. The Al atoms occupy the T sites in the samples (for details see Figure 6 of Ref.[75]) as follows: T2, T3, and T4 in FER/20; T1, T2, T3, and T4 in FER/27; and T1, T3, and T4 in FER/30. Figure 35 compares the relative concentration of Al atoms (in %) corresponding to the T sites obtained from (i) the corresponding Li^+ siting analyzed using ^{7}Li MAS NMR and (ii) ^{27}Al MAS NMR experiments.[75]

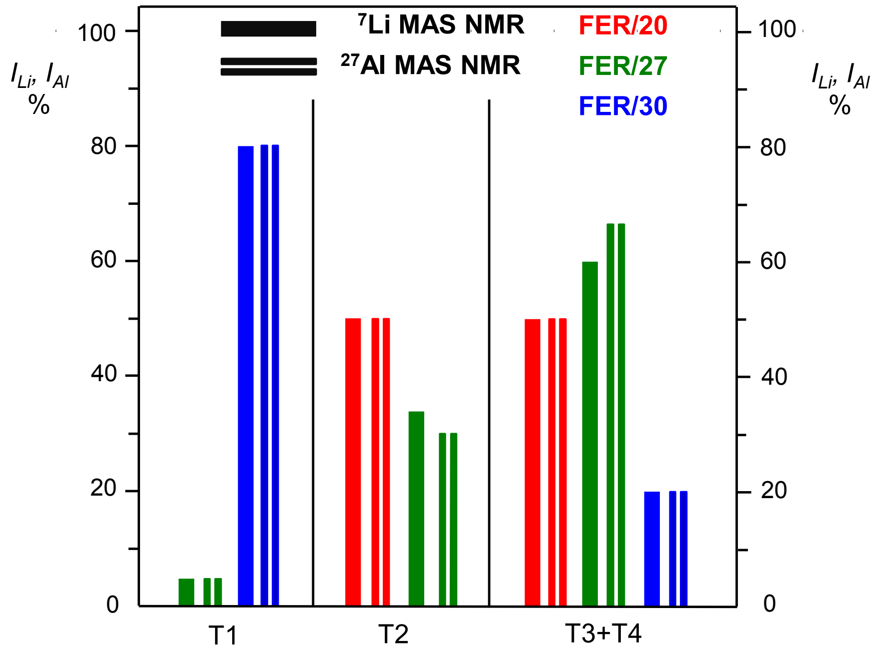

Figure 35. Relative concentration of Al atoms (in %) corresponding to the distinguishable framework T sites obtained from (i) the corresponding Li^+ siting analyzed using ^{7}Li MAS NMR and (ii) ^{27}Al MAS NMR.[75]

The agreement between the results obtained by ^{7}Li and ^{27}Al MAS NMR is very good and confirms the assignment of the experimental ^{7}Li NMR resonances to the Li^+ sites related to Al in the individual T sites. It substantiates that the siting of Li^+ is controlled by the siting of Al atoms in the zeolite framework. Moreover, the agreement supports the reliability of (i) the periodic DFT calculations of the local structure of Li^+ sites using extensive conformational sampling and (ii) DFT cluster computations of the ^{7}Li NMR shielding. Moreover, only the ^{27}Al 3Q MAS NMR experiments allow the distinction between the T3 and T4 sites and reveal that the ^{7}Li R4 resonance observed for all the three samples belongs to Li^+ in both the T3A and T4A sites. Therefore, the combination of ^{7}Li MAS NMR and 27Al 3Q MAS NMR experiments in tandem with DFT calculations is suggested to represent the optimal approach to the analysis of the Al and Li^+ siting in the framework T sites and extra-framework sites, respectively, in Si-rich zeolites.

6.1.5 Summary

Three dehydrated lithium exchanged Si-rich ferrierites were studied by ^{7}Li MAS NMR spectroscopy. One dimensional lineshape contains close overlapping resonances in a narrow range of chemical shifts with negligible quadrupolar broadening. To identify individual resonance high resolution ^{7}Li 2D EXSY MAS NMR spectroscopy had to be applied. Highly reliable periodic DFT calculations were in very good agreement with experimental data allowed interpretation of most of the individual lithium resonances. It was found that Li^{+} balancing Al in one T site can occupy two different crystallographic positions. On the other hand, assignment of such close resonances has to be performed very carefully but still resonances T3 and T4 cannot be distinguished. Results fit well with analysis of Al siting and thus verify proper assignment of Li^{+} resonances. It opens possibility to use Li^{+} as an additional probe of Al siting and shows importance and usefulness of multinuclear NMR approach.

Presented method based on the combination of quantitative 1D ^{7}Li MAS NMR and ^{7}Li 2D EXSY MAS NMR supported by DFT calculations can be, in general, applied to analysis of Li^{+} ions in other zeolites and various crystalline matrixes with a low concentration of Li^{+} ions and also to other NMR-active cations with no or negligible quadrupolar coupling.

6.2 Sodium ssNMR of Na-FER samples

6.2.1 ^{23}Na MAS and MQMAS NMR experiments at 11.7 T

^{23}Na MAS NMR spectra of dehydrated samples Na-FER/20, Na-FER/27 and Na-FER/30 measured in 4 mm and 3.2 mm probe head using single pulse excitation with high power proton decoupling acquired at spinning frequency of 12 and 20 kHz are shown in Figure 36 A and B, respectively. An acquisition time of single spectrum with mediocre signal to noise ratio ranged from 100 to 200 was of approximately 5 hours. ^{23}Na MAS NMR spectra of Na-FER samples are very broad (about 70 ppm) due to the quadrupolar character of sodium that is in contrast to narrow lineshape of lithium MAS NMR spectra. All spectra shows similar lineshape with dominant peak at around -25 ppm with intensive hump on the right at about -45 ppm and a minor shoulder on the left at -10 ppm. Positive effect of faster rotation on the pattern breadth indicates presence of quadrupolar interaction. Individual resonances of quadrupolar nuclei can form various shapes depending on the magnitude (C_Q) and the asymmetry parameter (η_Q) of EFG tensor (see Section 3.2.2.3) and therefore MQMAS experiments had been performed to obtain quadrupolar parameters of individual sodium resonances. 2D ^{23}Na MQMAS NMR spectra of dehydrated Na-FER samples spun in 4 mm o.d. rotors at 12 kHz and in 3.2 mm rotors at 20 kHz are show in the Figure 37 together with skyline projections in isotropic (F_1) and MAS (F_2) dimension. Note the acquisition time of one ^{23}Na MQMAS NMR experiment was of several days.

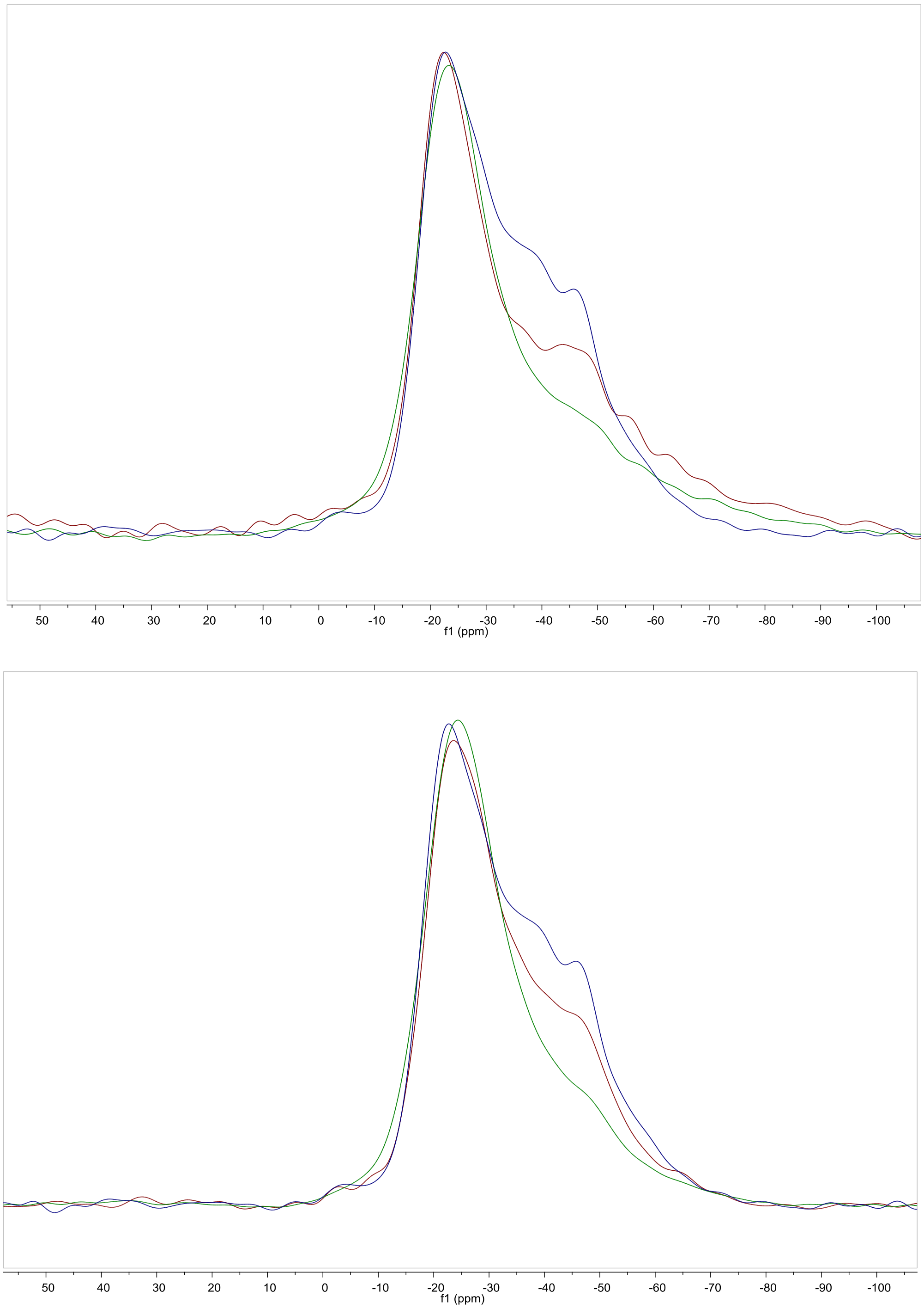

Figure 36. ^{23}Na MAS NMR spectra of samples Na-FER/20 (brown), Na-FER/27 (green) and Na-FER/30 (blue) acquired at 11.7 T in 4 mm probe (ν_{rot}= 12 kHz, top) and 3.2 mm probe (ν_{rot}= 20 kHz, bottom).

Rotation of the sample at higher frequency narrows 1D spectra due to averaging of the first order quadrupolar interaction, that are rotation dependent. Unfortunately, in the case of MQMAS experiments increased rotation did not improve resolution significantly, probably due to the smaller volume of the sample in 3.2 mm cuvette.

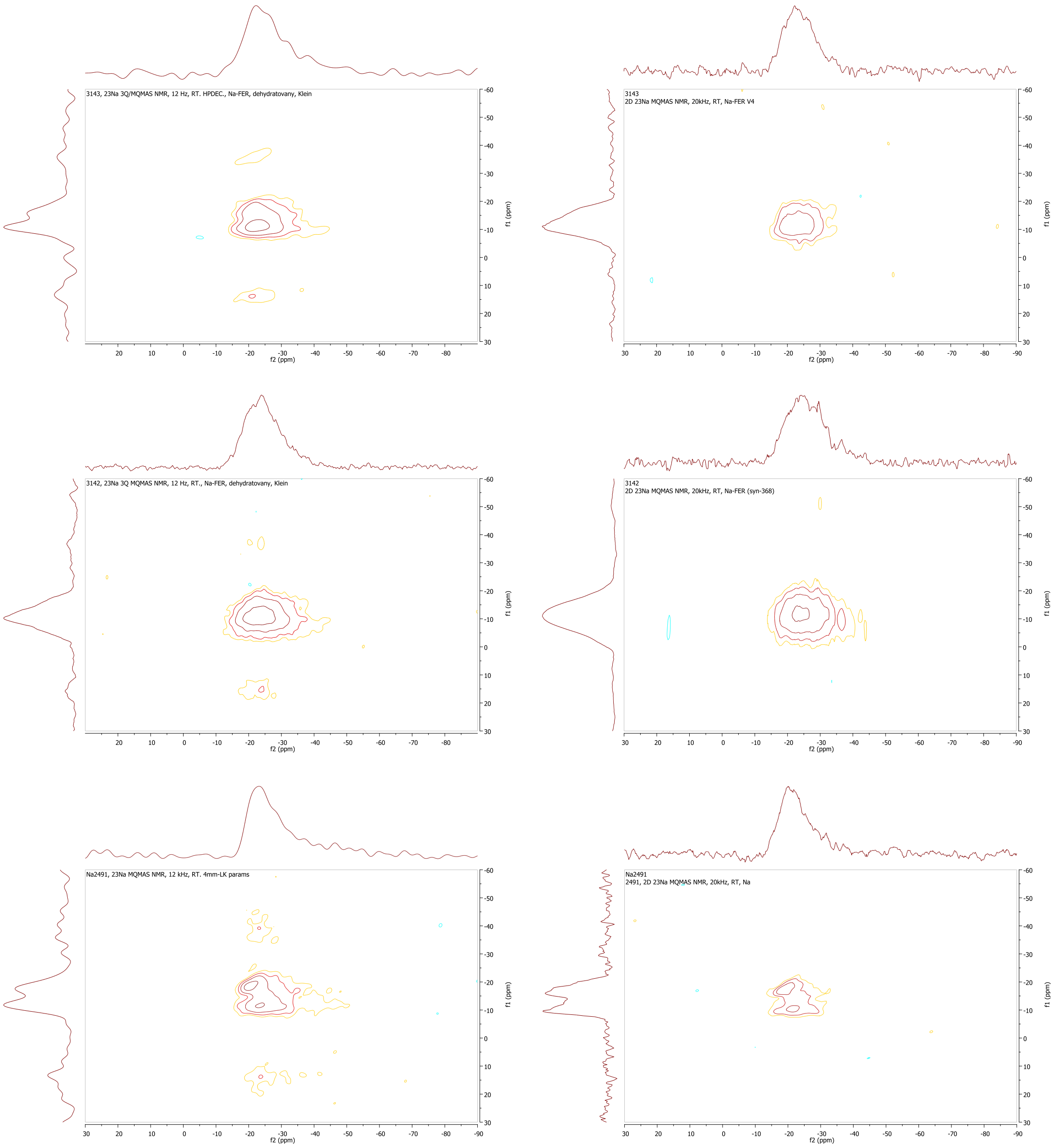

Figure 37. Isotropicaly sheared ^{23}Na MQMAS NMR spectra of dehydrated Na-FER/20 (top), Na-FER/27 (middle) and Na-FER/30 (botton¨m) samples spun in 4 mm o.d. rotors at 12 kHz (left) and in 3.2 mm rotors at 20 kHz (right) with skyline projections in isotropic (F_1) and MAS (F_2) dimensions

The isotopically sheared MQMAS spectra of Na-FER samples acquired using 4 mm and 3.2 mm probes at spinning frequencies of 12 kHz and 20 kHz, respectively, show similar features. Several resonances can be distinguished in 2D MQMAS spectra, but all resonances found in MQMAS spectra corresponds with the main peak in 1D MAS experiments. That is probably due to the lower sensitivity of MQMAS to broader resonances. Even the main peak in 1D MAS NMR spectra looks very similar for all samples and one can suggest it contains only one resonance, the 2D MQMAS experiments reveal that it consist of at least two resonances characterized by different NMR parameters. It demonstrates essential role of MQMAS experiments in NMR spectroscopy of quadrupolar nuclei. Unfortunately, due to the strong quadrupolar broadening and overlapping of the resonances and the fact, that resonances at -45 ppm in MAS spectra were not observed MQMAS spectra, we were not able to obtain NMR parameters of all individual resonances and to perform precise analysis of Na siting. One of the possibilities how to increase spectral resolution is an application stronger magnetic field.

6.2.2 ^{23}Na MAS and MQMAS NMR experiments at 21.1 T

^{23}Na MAS NMR spectra of dehydrated samples Na-FER/20, Na-FER/27 and Na-FER/30 measured at ultra-high magnetic field ($B_0 = 21.1$ T, $\nu_0(^1H) = 900.08$ MHz) in 4 mm probe using single pulse excitation acquired at spinning frequency of 10 kHz are shown in Figure 38.

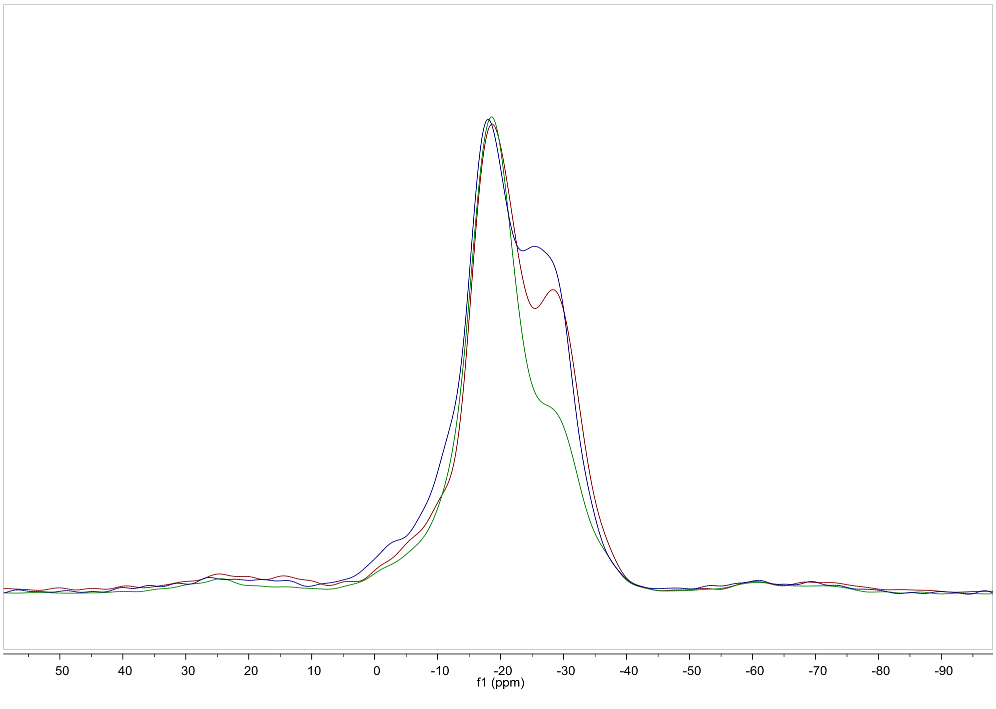

Figure 38. ^{23}Na MAS NMR spectra of samples Na-FER/20 (brown), Na-FER/27 (green) and Na-FER/30 (blue) acquired at 21.1 T in 4 mm probe (ν_{rot}= 10 kHz)

An acquisition time of approximately 35 minutes was required to obtain single/one spectrum with a very good signal to noise ratio of approximately 400. That is significantly better performance compared to results obtained at 11.7 T where inferior quality spectra were collected during 5 hours. A decrease of the breath of the spectra by factor 2 compared to experiments at 11.7 T is caused by a suppression of the quadrupolar interaction by/at higher magnetic field. This effect is clearly visible in 2D ^{23}Na MQMAS NMR spectra (see Figure 39) where the breath of the spectra in isotropic (vertical) dimension remains the same, but in MAS (horizontal) dimension the breath is much smaller. Acquisition time of one MQMAS spectrum was of 5 hours. Even the signal to noise ratio is similar as in the case of MQMAS experiments at 11.7 T, the spectral resolution is better due to the suppression of quadrupolar broadening in MAS (F_2) dimension and also due to the fact, that resonances forming a hump in single pulse spectra are visible in ^{23}Na MQMAS NMR spectra at ultra-high magnetic field. Position of these resonances denotes stronger quadrupolar interaction then the other resonances and that is the reason why it was not observable at lower magnetic field. The effect of external magnetic field strength on ^{23}Na MAS NMR spectra of dehydrated sample Na-FER/20 is demonstrated in Figure 40.

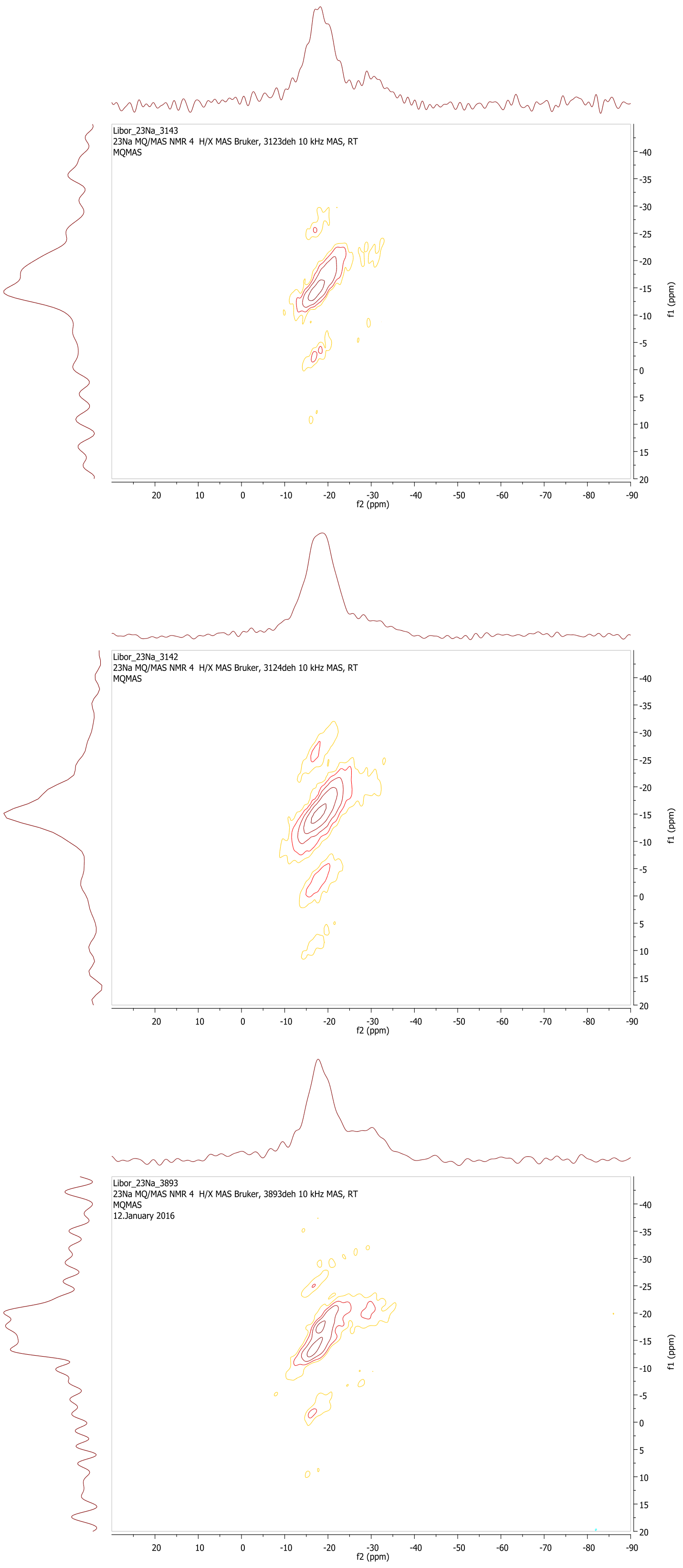

Figure 39. Isotropicaly sheared ^{23}Na MQMAS NMR spectra of samples Na-FER/20 (top), Na-FER/27 (middle) and Na-FER/30 (bottom) acquired at 21.1 T in 4 mm probe (ν_{rot}= 10 kHz) with skyline projections in isotropic (F_1) and MAS (F_2) dimension

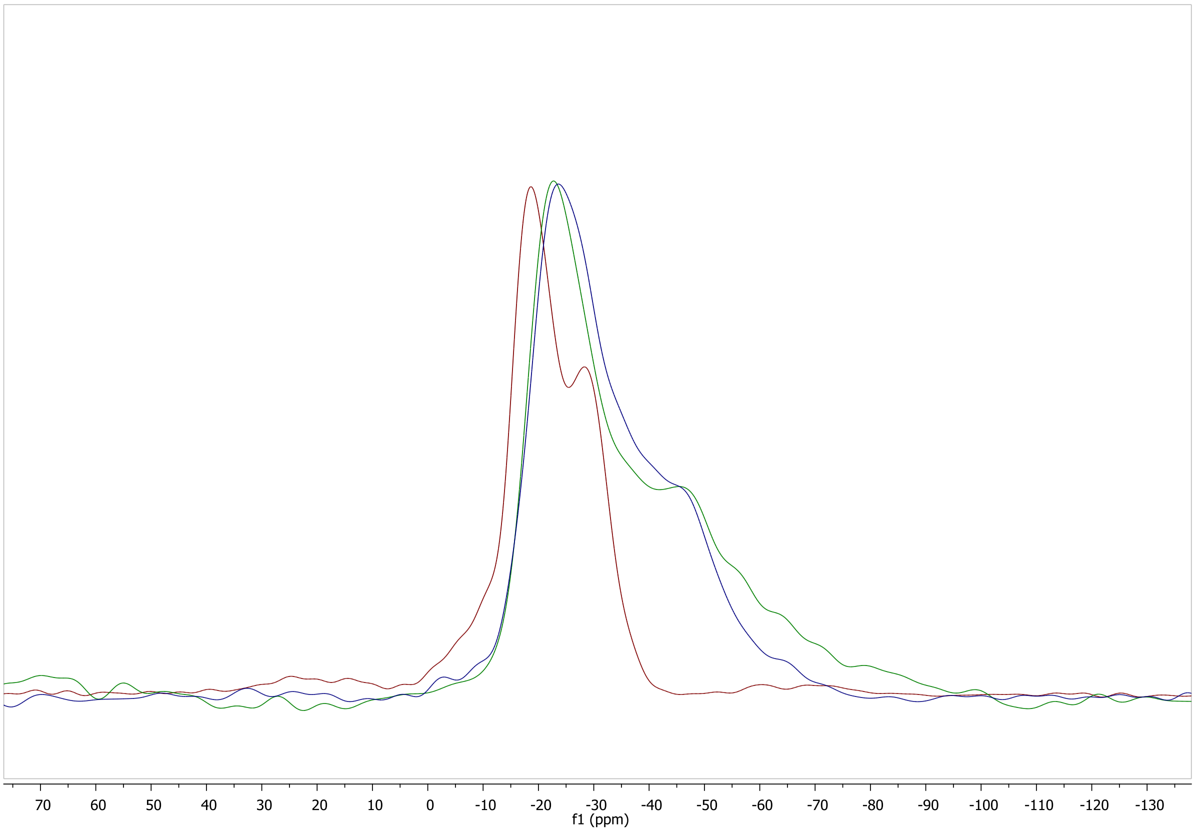

Figure 40. ^{23}Na MAS NMR spectra of the sample Na-FER/20 recorded at 21.1 T (brown), 11.7 T, 4 mm (blue) and 11.7 T, 3.2 mm (green)

6.2.3 Quantitative analysis of Na$^+$ distribution

As mentioned before, there are two methods for extracting NMR parameters of individual resonances from MQMAS spectrum. The traditional one is based on fitting of cross-section traces in the center of gravity of individual resonances and the newer one is based on simultaneous fitting of both MAS and MQMAS spectra. It this work the latter was used since the former can provide inaccurate results especially when spectra consist of several overlapping resonances as in our case). To obtain NMR parameters of individual Na$^+$ resonances in each Na-FER sample, its ^{23}Na MAS and MQMAS NMR spectra acquired at two different magnetic fields (i.e. four spectra for each sample) were simultaneously fitted using dmfit software. Since NMR parameters reflect structure and environment around nuclei in the sample and those parameters are not field dependent, then we should be able to model all four experimental lineshapes using a set of resonances with unique parameters of the same or very similar value for all four models.

At first, number of resonances and their approximate position were suggested and their NMR parameters were estimated by careful inspection of ultra-high field 2D MQMAS NMR spectra. Parameters of individual resonances were then automatically optimized by fitting algorithm and subsequently used for modeling ultra-high field 1D MAS NMR spectrum. When model did not fit experimental lineshape, parameters were adjusted till both 1D and 2D models fit well NMR spectra. In the next step, ^{23}Na MAS and MQMAS NMR spectra recorded at magnetic field of 11.7 T were modeled using resonances with the same parameters to prove correctness of fit. Again, when models did not fit NMR spectra sufficiently, parameters of individual resonances were simultaneously adjusted and optimized step by step until all models fit well experimental lineshapes. This procedure is very exacting, but

Four resonances were identified in the sample Na-FER/20 and Na-FER/27, while six resonances were found in the sample Na-FER/30. ^{23}Na MAS and MQMAS spectra of Na-FER samples together with models are shown in Figure 41, Figure 42 and Figure 43, respectively. NMR parameters of individual sodium resonances are summarized in Table 3. Relative intensities of individual resonances were calculated only from MAS models since MQMAS experiments are not quantitative. ^{23}Na chemical shifts and relative intensities of individual Na$^+$ resonances of Na-FER samples taken from model of ultra-high field MAS NMR spectra are visualized in Figure 44.

Na-FER/20

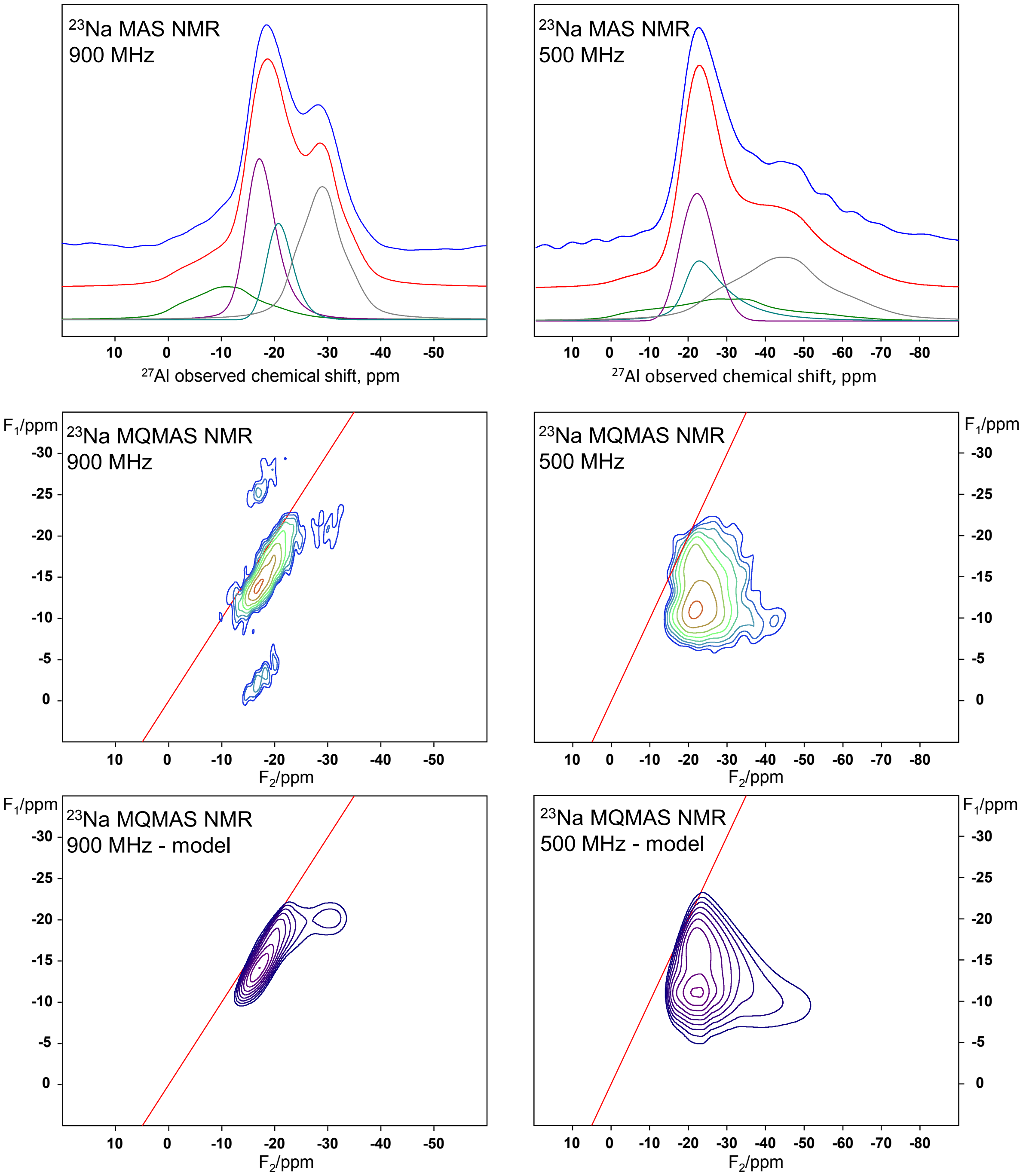

Figure 41. Experimental and modeled ^{23}Na MAS and MQMAS NMR spectra of Na-FER/20 sample recorded at and $B_0 = 21.1$ T (900Hz) and $B_0 = 11.7$ T (500 Hz)

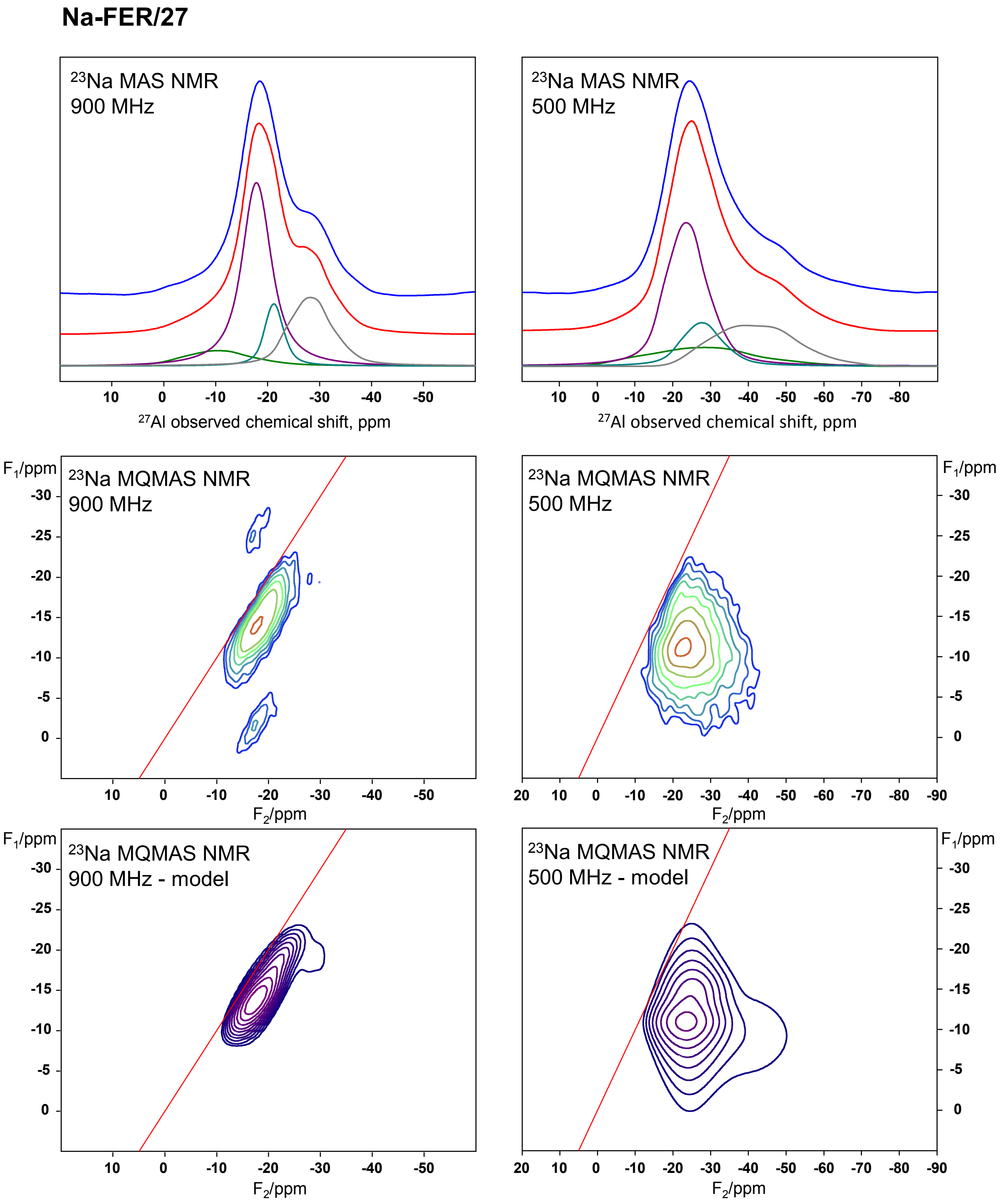

Figure 42. Experimental and modeled ^{23}Na MAS and MQMAS NMR spectra of Na-FER/27 sample recorded at and B_0 = 21.1 T (900Hz) and B_0 = 11.7 T (500 Hz)

Na-FER/30

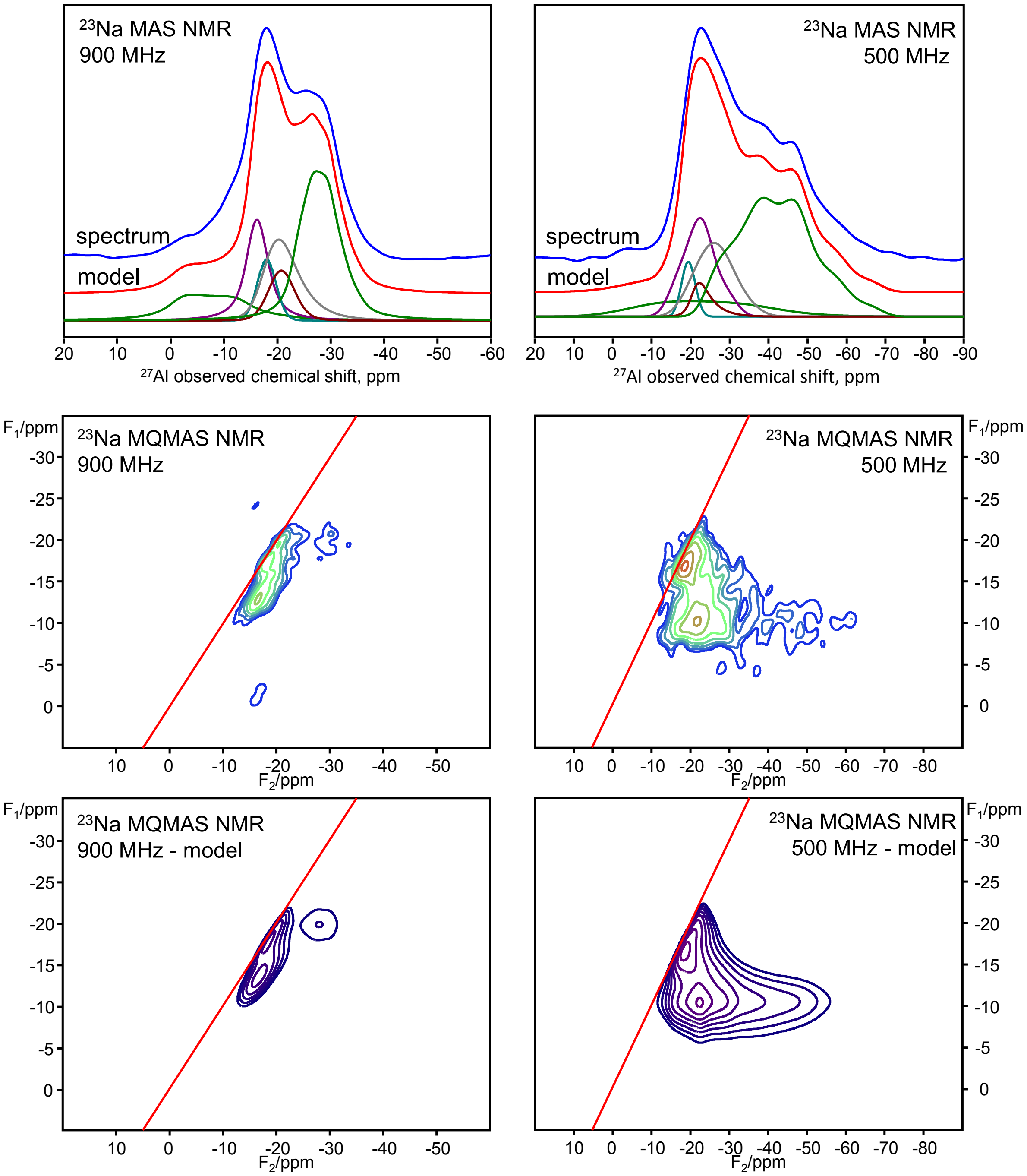

Figure 43. Experimental and modeled ^{23}Na MAS and MQMAS NMR spectra of Na-FER/30 sample recorded at B_0 = 21.1 T (900Hz - left) and B_0 = 11.7 T (500 Hz - right)

Table 3. ^{23}Na chemical shift (δ_{Na}) and relative intensity (*I*) of individual Na$^+$ resonances of Na-FER samples

sample	res.	exp.	δ_{Na}/ppm	C_Q/MHz	η_Q	*I*/%	Na$^+$ site
Na-FER/20	I	MAS 500	0.0	4.2	0.7	17	T2-/T4-6MR
		MQ 500 [a]	n/a	n/a	n/a	n/a	
		MAS 900	0.0	4.7	0.65	15	
		MQ 900 [a]	n/a	n/a	n/a	n/a	
	IIa	MAS 500	-15.5	2.1	0.5	26	T3-8MR
		MQ 500	-15.0	2.1	0.6	-	
		MAS 900	-15.6	2.1	-	31	
		MQ 900	-15.1	2.1	-		
	IIb	MAS 500	-19.2	2.1	-	17	T4-8MR
		MQ 500	-19.2	2.0	-	-	
		MAS 900	-19.2	2.0	-	15	
		MQ 900	-19.3	2.0	-	-	
	III	MAS 500	-22.5	3.6	0.7	40	T2-8MR
		MQ 500	-22.3	3.7	0.6	-	
		MAS 900	-22.5	3.6	0.7	39	
		MQ 900	-24.0	3.6	0.6	-	
Na-FER/27	I	MAS 500	-2.0	4.1	0.6	14	T2-/T4-6MR
		MQ 500 [a]	n/a	n/a	n/a	n/a	
		MAS 900	-1.0	4.4	0.6	10	
		MQ 900 [a]	n/a	n/a	n/a	n/a	
	IIa	MAS 500	-15.5	2.2	0.6	47	T3-8MR
		MQ 500	-15.5	2.2	0.6	-	
		MAS 900	-15.5	2.2	0.6	53	
		MQ 900	-15.3	2.2	-	-	
	IIb	MAS 500	-20.0	2.2	0.6	14	T4-8MR
		MQ 500	-19.3	2.1	0.6	-	
		MAS 900	-19.0	2.1	0.6	11	
		MQ 900	-20.0	2.0	-	-	
	III	MAS 500	-22.0	3.6	0.5	25	T2-8MR
		MQ 500	-20.5	3.5	0.5	-	
		MAS 900	-22.0	3.6	0.6	26	
		MQ 900	-23.0	3.5	0.5	-	
Na-FER/30	I	MAS 500	-0.3	4.1	0.0	10	T2-/T4-6MR
		MQ 500 [a]	n/a	n/a	n/a	n/a	
		MAS 900	2.0	4.7	0.0	13	
		MQ 900 [a]	n/a	n/a	n/a	n/a	
	IIa	MAS 500	-14.5	2.1	0.9	17	T1-8MR2
		MQ 500	-14.5	2.0	0.9	-	
		MAS 900	-14.2	2.0	0.7	16	
		MQ 900	-14.3	2.2	-	-	
	IIb	MAS 500	-17.5	1.1	0.6	4	T3-8MR
		MQ 500	-17.4	1.0	-	-	
		MAS 900	-17.5	1.0	-	7	
		MQ 900	-17.7	1.1	-	-	
	IIc	MAS 500	-18.0	2.3	0.6	15	T1-ALPH
		MQ 500	-17.2	2.3	-	-	
		MAS 900	-18.0	2.3	-	18	
		MQ 900	-17.5	2.2	-	-	
	IId	MAS 500	-20.8	1.3	-	4	T4-8MR
		MQ 500	-20.4	1.2	-	-	
		MAS 900	-20.0	1.3	-	8	
		MQ 900	-20.2	1.3	-	-	
	III	MAS 500	-22.9	3.5	0.55	50	T1-8MR1
		MQ 500	-22.7	3.6	0.55	-	
		MAS 900	-22.5	3.4	0.50	38	
		MQ 900	-23.1	3.4	0.55	-	

[a] Resonance I was not detected in MQMAS

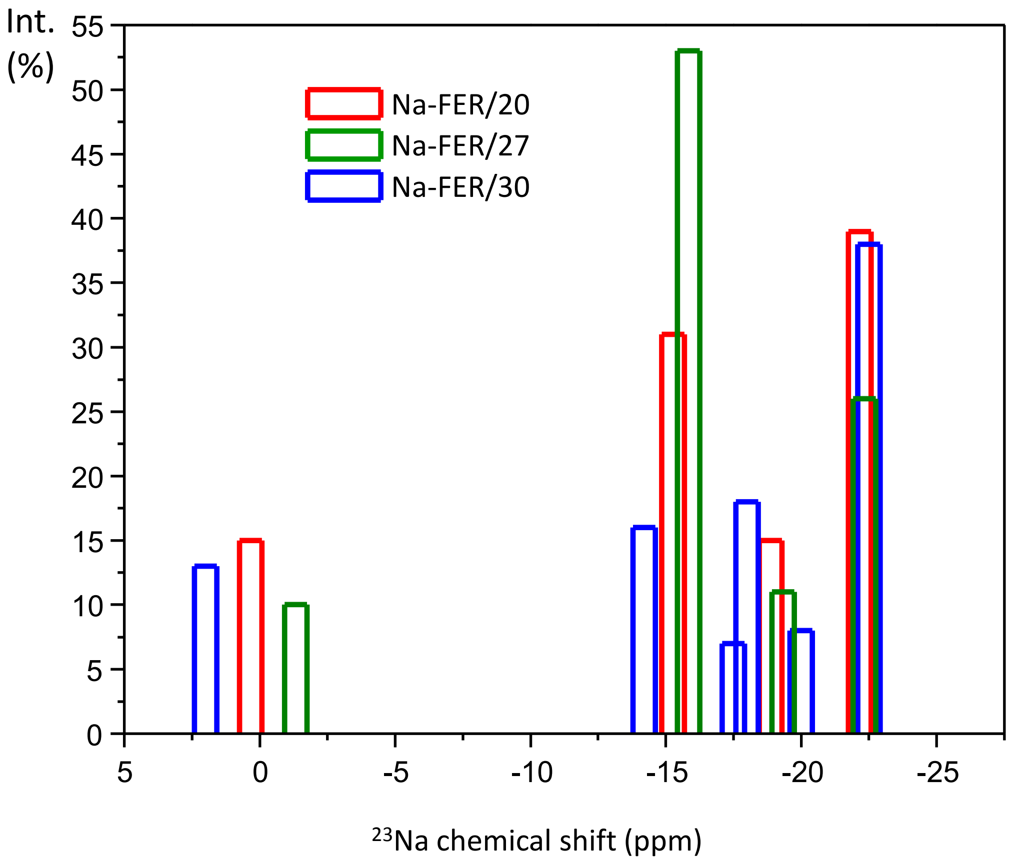

Figure 44. ^{23}Na chemical shift and relative intensity of individual Na$^+$ resonances of Na-FER samples

6.2.4 Analysis of Na$^+$ siting

As in the case of Li$^+$, empirical interpretation of Na$^+$ resonances is not possible. Theoretical computations were made by the group of Dr. Štěpán Sklenák (see Appendix A for details). Calculated NMR parameters of nine low energy sites of Na$^+$ compensating negative charge of Al in different T sites are summarized in

Table 4. Three possible low energy Na$^+$ sites were found for Al in T$_1$ site, two for T$_2$(Al), as same as for T$_3$(Al) and T$_4$(Al). Calculated values of ^{23}Na chemical shift between 0.7 ppm and -19.9 ppm and quadrupolar coupling constant ranging from 2.6 MHz to 5.7 MHz are in very good agreement with experimental ones ranging from 1.0 ppm to -23.5 ppm and from 0.9 MHz to 5.3 MHz, respectively.

Table 4. Calculated ^{23}Na shielding *($\sigma_{Na,calc}$)*, chemical shift *($\delta_{Na,calc}$)*, quadrupolar coupling constant *($C_{Q,calc}$)*, asymmetry parameter *($\eta_{Q,calc}$)*, quadrupolar product *($P_{Q,calc}$)* and relative energies *(ΔE)* of eight optimized low energy Na$^+$ sites

Na$^+$ site	$\sigma_{Na,calc}$ ppm	$\delta_{Na,calc}$ ppm	$C_{Q,calc}$ MHz	η_{calc}	$P_{Q,calc}$ MHz	ΔE kcal.mol^{-1}	
T1-α	583.12	**-14.5**	2.467	0.744	**2.7**	1.8	
T1-8MR2	581.15	**-12.6**	3.02	0.767	**3.3**	1.5	DEFORMED 8MR
T1-8MR1	588.39	**-19.8**	3.666	0.466	**3.8**	0.0	NORMAL 8MR
T2-6MR	570.73	**-2.1**	5.427	0.507	**5.7**	0.0	
T2-8MR	588.53	**-19.9**	3.67	0.714	**4**	1.9	
T3-α	581.48	**-12.9**	2.443	0.632	**2.6**	0.0	
T3-8MR	582.20	**-13.6**	3.008	0.738	**3.3**	2.2	
T4-8MR	587.06	**-18.5**	2.650	0.963	**3.0**	5.9	
T4-MR	67.88	**0.7**	4.852	0.700	**5.2**	0.0	

Based on the comparison of experimental and theoretical values in Figure 45, possible Na-sites were assigned to Na resonances in Table 3. Nevertheless, calculations show, that we are able to distinguish Na in different rings or sites, but not specific Al T site, e.g. that sodium accommodated in one of 8-mr has the same NMR parameters despite Al is in T1 or T3 site. As a consequence, Na^+ cannot be use as a probe of Al siting in the case of ferrierite.

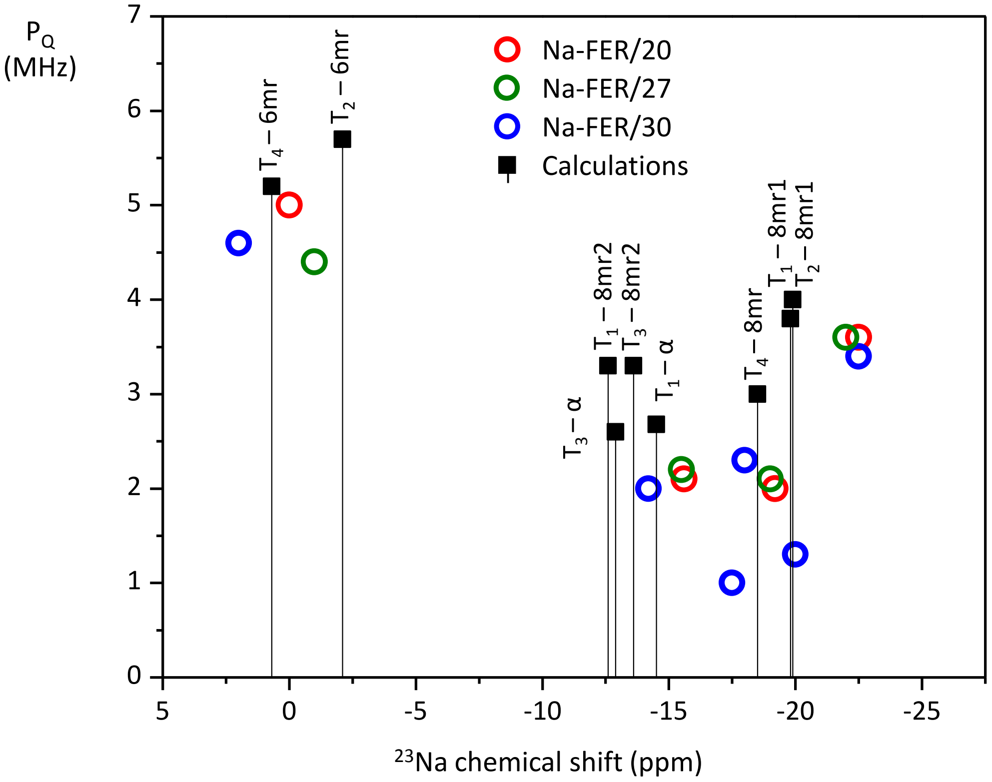

Figure 45. ^{23}Na chemical shift and quadrupolar product of individual resonances of Na-FER samples compared to calculated values of low-energy Na^+ sites.

6.2.5 Summary

^{23}Na MAS and MQMAS NMR spectra of dehydrated Na-FER samples were acquired at both high and ultra-high magnetic field strengths of 11.7 T and 21.1 T, respectively. ^{23}Na NMR experiments at 11.7 T did not allow complete analysis of Na^+ environment in our samples because some resonances found in ^{23}Na MAS NMR spectra were not observed in MQMAS spectra. Moreover, experiments are very time consuming and resulting spectra are very broad due to the strong quadrupolar interaction.

In contrast to ^{23}Na NMR experiments at 11.7 T, measurements performed at ultra-high magnetic field of 21.1 T provide much better results regarding spectral resolution and time consumption. Even the signal to noise ratio of MQMAS experiments at 21.1 T is similar to those at 11.7 T, spectral resolution increased due to the suppression of quadrupolar broadening and quadrupolar induced shift. Moreover, MQMAS spectra revealed presence of resonances that we were not able to observe at 11.7 T.

By careful simultaneous deconvolution (analytical simulation) of MAS and MQMAS spectra recorded at 21.1 T, 4-5 resonances were found in Na-FER samples and their NMR parameters were extracted.

Comparison of quadrupolar parameters obtained at different magnetic field helps to identify individual resonances and guaranteed accurate parameters were obtained.

Theoretical calculations revealed that NMR parameters of sodium cations balancing Al in different T sites while located in the same ring are similar. Thus, Na^+ is not a suitable probe of Al siting in the case of ferrierite, yet ^{23}Na ssNMR can provide information about location of sodium in different rings.

6.3 Structure of cationic sites in dehydrated CHA[a]

The ^{27}Al MAS NMR experiments on hydrated zeolites allowed a determination of the siting of Al atoms in the T sites but the local arrangement of the whole cationic site (i.e., the extra-framework cation and the framework atoms forming the structure of the cationic site including the balanced framework Al atoms) could not have been analyzed. Only a few studies investigated dehydrated zeolites by ^{27}Al MAS NMR spectroscopy and therefore our knowledge in this area is significantly limited.[80,81] Freude et al. demonstrated that it was possible to monitor Al atoms in dehydrated zeolites by ^{27}Al MAS NMR spectroscopy and his results showed a variability of the ^{27}Al MAS NMR spectra and line widths for faujasite and ZSM-5 structures exchanged with Na and H cations.[80-83] Thus, the ^{27}Al NMR spectra of dehydrated zeolites have to contain complex and detailed information regarding the Al siting in the framework and concerning the local structure of the site accommodating the extra-framework cation in a dehydrated zeolite. However, this information has not been utilized yet. This is caused by the absence of understanding the mechanism of the broadening of the spectra and of the parameters controlling its width and shape. There is only a generally accepted hypothesis that narrow ^{27}Al NMR resonances of framework Al atoms in hydrated zeolites are caused by narrowing the broad ^{27}Al NMR resonance (due to the quadrupolar broadening) by averaging the electrostatic field around AlO_4^- tetrahedra due to molecular motion of water molecules. To elucidate an effect of cation on ^{27}Al NMR spectra of zeolites, a set of CHA samples were investigate.

6.3.1 ^{27}Al NMR of CHA Samples

Figure 46 compares the single pulse ^{27}Al MAS NMR spectra of the hydrated M-CHA as well as hydrated M-CHA(deh) (M = Li, Na, and K) samples. The dehydration of the samples is connected with a marked broadening of the ^{27}Al NMR signal. Moreover, this broadening depends on the cation balancing the framework negative charge.

---

[a] This section is based on Ref.(79) Klein, P.; Pashkova, V.; Thomas, H. M.; Whittleton, S. R.; Brus, J.; Kobera, L.; Dedecek, J.; Sklenak, S. Local Structure of Cationic Sites in Dehydrated Zeolites Inferred from 27Al Magic-Angle Spinning NMR and Density Functional Theory Calculations. A Study on Li-, Na-, and K-Chabazite. *The Journal of Physical Chemistry C* **2016,** *120* (26), 14216.

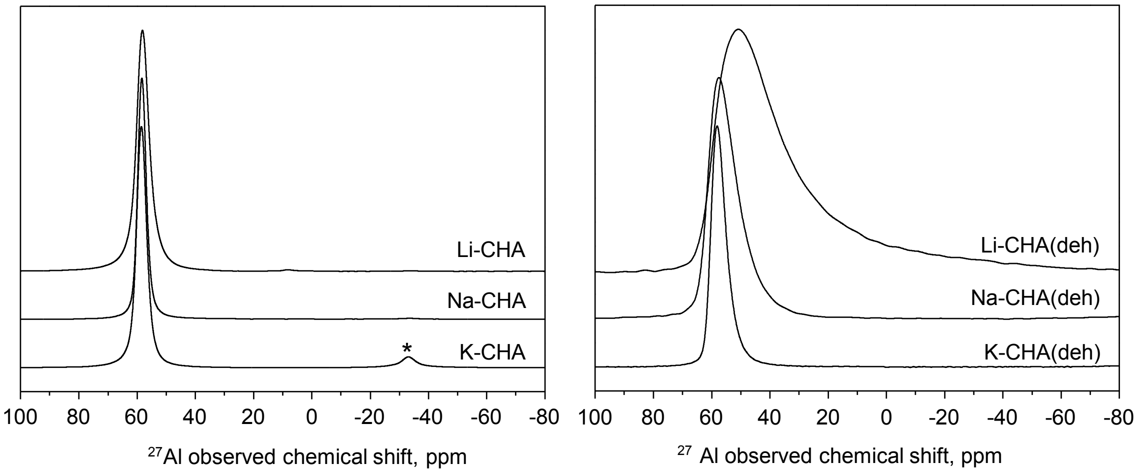

Figure 46. ^{27}Al MAS NMR spectra of hydrated (left) and dehydrated (right) Li-, Na- and K-chabazites

^{27}Al 3Q MAS NMR spectra of the dehydrated M-CHA(deh) samples were collected to investigate the mechanism of line broadening in dehydrated zeolites. Note that the collection of the MQ MAS NMR spectrum of an enormously broad signal requires the acquisition time of several days. Both the single pulse ^{27}Al MAS and isotropically sheared ^{27}Al 3Q MAS spectra of all the dehydrated samples were simultaneously fitted in the dmfit software using "Czjzek simple" model to obtain the ^{27}Al NMR parameters. ^{27}Al MAS and MQMAS NMR spectra of dehydrated Li-CHA(deh) sample together with simulations are shown in Figure 47.

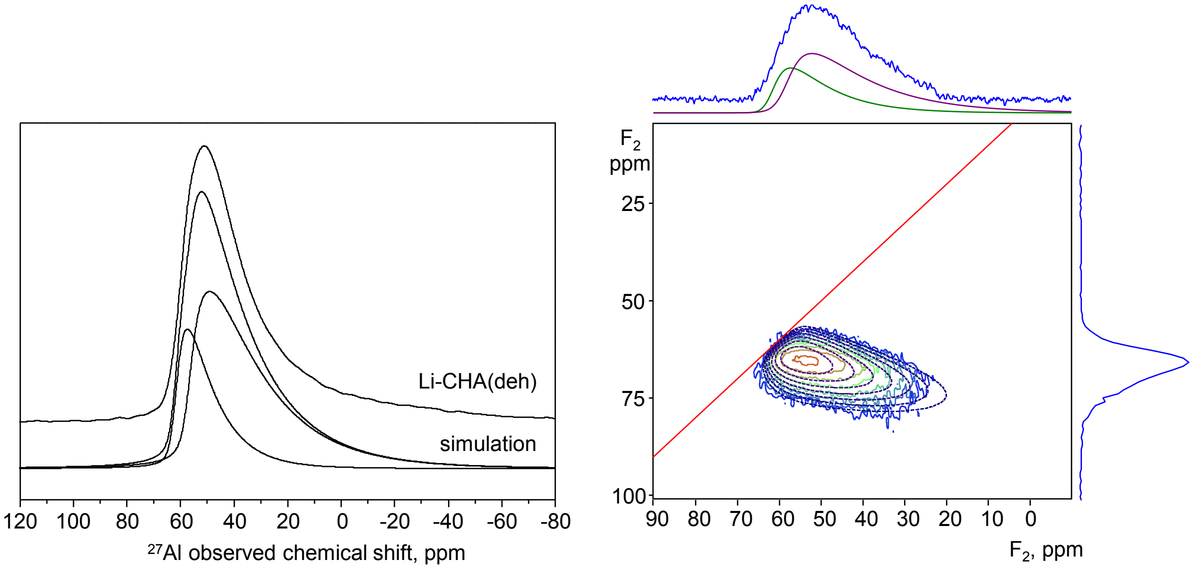

Figure 47. ^{27}Al MAS (left) and MQMAS (right) NMR spectra of dehydrated Li-, Na- and K-chabazites together with simulations

The spectra of the dehydrated Na-CHA and K-CHA samples were simulated using one resonance while two resonances are required for the dehydrated Li-CHA sample. The values of the ^{27}Al isotropic chemical shift and the nuclear quadrupolar coupling parameter P_Q from spectra simulation are shown in Table 5.

Table 5. ^{27}Al chemical shift *(δ),* quadrupolar coupling product *(P_Q)* and relative intensity *(I)* of individual ^{27}Al resonances of CHA samples

sample	resonance	δ/ppm	P_Q/MHz	I/%
Li-CHA(deh)	I	62.0	5.3	35
	II	57.0	7.3	65
Na-CHA(deh)	I	61.3	4.2	100
K-CHA(deh)	I	60.1	2.9	100
Li-CHA	I	60.0	2.4	100
Na-CHA	I	59.5	1.8	100
K-CHA	I	59.5	1.8	100
K-CHA(190K)	I	59.7	2.1	100

The effect of low temperature on the ^{27}Al MAS NMR spectrum of chabazite is revealed in Figure 48 which compares the ^{27}Al MAS NMR spectra of the hydrated K-CHA sample measured at RT and -80° C. The decrease of the temperature is followed by only a negligible broadening of spectrum, see Table 5 which shows the ^{27}Al NMR parameters of the spectra.

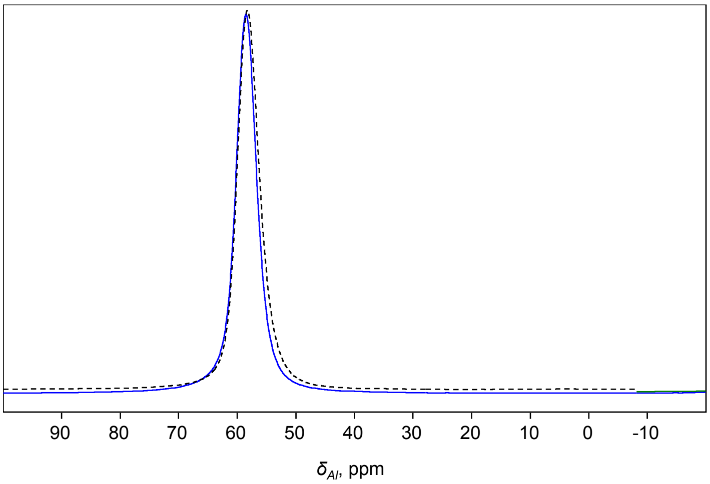

Figure 48. The effect of low temperature on the ^{27}Al MAS NMR spectrum of K-CHA sample. Spectrum recorded at 190 K (solid blue) and at 303 K (dashed)

Figure 46 shows the enormous broadening of the ^{27}Al NMR resonances for the dehydrated samples. The ^{27}Al MAS NMR spectra of the dehydrated M-CHA (M = Li, Na, and K) zeolites significantly differ in their width depending on the cation balancing the negative charge of the AlO_4^- tetrahedra although there is only one crystallographically distinguishable framework T site which could be occupied by Al atoms. The largest broadening (i.e., the largest P_Q values of 5.3 and 7.3 MHz) is observed for the smallest cation Li^+ while the smallest broadening (i.e., the smallest P_Q value of 2.9 MHz) for the largest cation K^+. The broadening for the Na-CHA sample (i.e., the P_Q value of 4.2 MHz) is in between those for the Li-CHA and K-CHA materials. These results indicate (i) a significant role of the cation interaction with the zeolite framework in the broadening of the ^{27}Al MAS NMR signal upon dehydration of the M-CHA samples, (ii) a limited or negligible role of the motion of water molecules in zeolite channels causing "averaging" the local electrostatic field and thus narrowing the ^{27}Al NMR resonances in hydrated zeolites.

6.3.2 Elucidation of effect of extra-framework kation on ^{27}Al NMR spectrum

Calculations of the six models of the cationic sites yielded the optimized structures and the corresponding relative energies of the two cationic sites (M^+ accommodated in six-membered and eight-membered rings), see Figure 49.

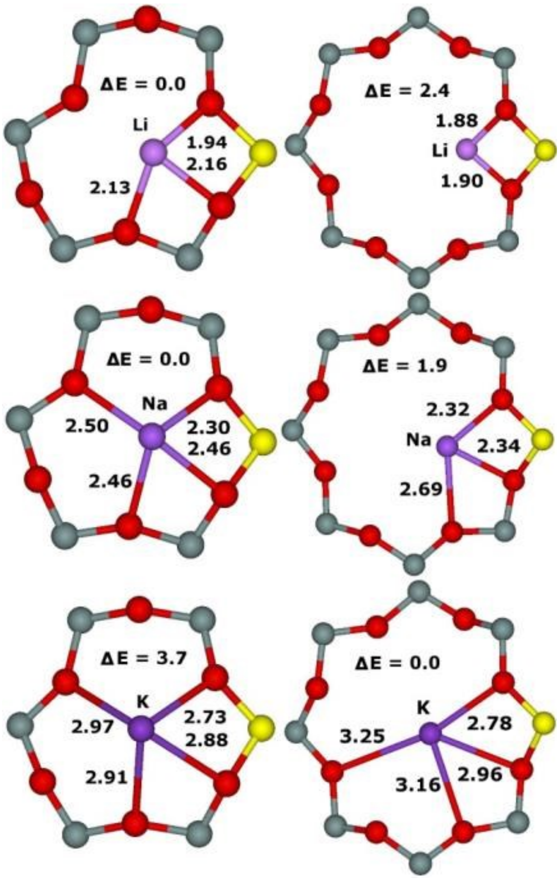

Figure 49. Optimized structures (M–O distances in Å) of the cationic sites of Li^+, Na^+, and K^+ accommodated in 6-, and 8-rings and the relative energies for each M^+ in kcal/mol. Silicon atoms are in gray, oxygen atoms in red, aluminium atoms in yellow[79]

Our computational results show that all three M^+ cations are coordinated to two O atoms of AlO_4^- tetrahedron for both the sites. In addition, there is additional coordination to O atoms of SiO_4: one for Li^+-6-ring and Na^+-8-ring; two for Na^+-6-ring, K^+-6-ring, and K^+-8-ring. The smaller Li^+ and Na^+ cations accommodated in the 6-ring are calculated to be more stable by 2 kcal/mol while the largest K^+ cation prefers the 8-ring by 4 kcal/mol.

Table 6 reveals the ^{27}Al NMR shielding values, the C_Q, η, and P_Q values for the Al atom. The ^{27}Al NMR parameters were also computed for the Al atom of the optimized bare zeolite framework model (Table 6).

Table 6. Relative energies in kcal/mol of the M^+ sites and the ^{27}Al NMR parameters (shielding in ppm, C_Q in MHz, η (dimensionless), and P_Q in MHz) Calculated for the Computational Models[a]

		optimized cationic site							
		with M^{+-}				removed M^{+-}			
cation model	ΔE	shielding	C_Q	η	P_Q[15]	shielding	C_Q	η	P_Q[15]
Li^+-8MR	2.4	505.2	9.3	0.28	9.4	505.8	6.8	0.22	6.9
Li^+-6MR	0.0	509.4	9.5	0.77	10.4	509.5	7.2	0.74	7.8
Na^+-8MR	1.9	505.8	5.9	0.58	6.2	506.7	4.0	0.86	4.5
Na^+-6MR	0.0	508.9	7.5	0.98	8.6	509.5	5.6	0.98	6.4
K^+-8MR	0.0	507.5	4.0	0.73	4.3	507.9	3.0	0.95	3.4
K^+-6MR	3.7	508.9	6.2	0.91	7.0	509.2	4.7	0.85	5.2
		bare framework							
		with M^+				M^+ replaced by charge[b]			
		shielding	C_Q	η	P_Q[15]	shielding	C_Q	η	P_Q[15]
Li^+-8MR		506.0	1.8	0.99	2.1	510.2	3.0	0.91	3.4
Li^+-6MR		507.5	4.7	0.81	5.2	510.0	3.2	0.71	3.5
Na^+-8MR		507.2	2.0	0.75	2.2	510.2	3.0	0.92	3.4
Na^+-6MR		508.1	4.4	0.88	4.9	510.0	3.1	0.70	3.3
K^+-8MR		508.8	2.3	0.78	2.5	510.2	3.0	0.89	3.4
K^+-6MR		508.7	4.0	0.94	4.6	510.1	3.0	0.68	3.2

[a] The NMR parameters calculated for the bare framework model: shielding = 510.2 ppm, C_Q = 3.5 MHz, η = 0.83, Pq = 3.9 MHz. [b] Background charge at the positions of M^+.

Table 5 and Table 6 show that the measured and calculated, respectively, ^{27}Al NMR parameters of the three dehydrated zeolites are in good agreement indicating that both the computational model and the theoretical approach provide realistic results regarding (i) the structure of the cationic sites including the local structure of the AlO_4^- tetrahedra and (ii) the ^{27}Al NMR parameters. The agreement reveals that the significant increase of the quadrupolar interaction, which is the most remarkable feature of the ^{27}Al MAS NMR spectra of dehydrated zeolites, of the ^{27}Al NMR resonances in the dehydrated zeolites occurs due to the strong coordination of the extra-framework M^+ cation in the vicinity of the framework Al atom. Note that the calculations were performed for the silicon-rich chabazite SSZ-13 with one isolated Al atom per unit cell (Si/Al 35) while the ^{27}Al (3Q) MAS NMR spectra were recorded for the aluminum-rich material (Si/Al 2.2) containing many Al-O-Si-O-Al sequences in the zeolite framework and having majority of 6- and 8-rings occupied by extra-framework M^+ cations.

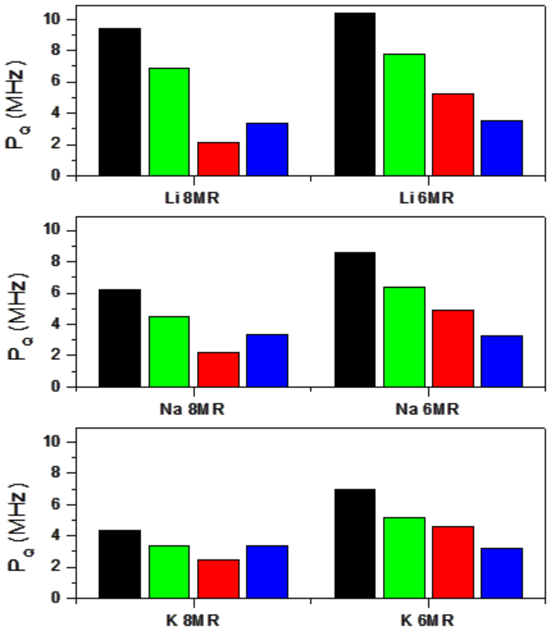

Figure 50. The calculated P_Q values for (i) the Li^+-8-ring, Li^+-6-ring, Na^+-8-ring, Na^+-6-ring, K^+-8-ring, and K^+-6-ring models (black bars), (ii) the six models with the removed M^+ (green bars), (iii) the bare framework model with the added M^+ cations (red bars), and (iv) the bare framework model with the added + background charges (blue bars)[79]

The effect of the binding of M^+ to the zeolite framework upon dehydration on the ^{27}Al NMR parameters is composed of two contributions: (i) the change of the local structure of AlO_4^- (i.e., deformation) caused by the binding of M^+ to the zeolite framework without including the effect of the M^+ cation; (ii) the effect of the M^+ cation with the exclusion of the influence of the change of the local structure of AlO_4^- due to the coordination of M^+ to the zeolite framework. The latter could be further investigated employing the background (point) + charge instead of the M^+ cation. These calculations permit the evaluation of the effect of the + charge of the cation M^+ without including the other effects of the cation M^+.

The calculations of the ^{27}Al NMR parameters for the optimized cationic sites with the removed M^+ cations (Table 6) reveal that the main factor responsible for the enormous broadening of the ^{27}Al NMR resonances of the dehydrated samples is the deformation of the local structure of AlO_4^- due to the binding of M^+ to the zeolite framework. The calculated P_Q values were only slightly smaller by ca 2.6, 2.0, and 1.4 MHz for Li^+, Na^+, and K^+ cations, respectively, than those calculated with the presence of the M^+ cations (Table 6 and Figure 50).

Conversely, the influence of M^+, without considering the deformation of the local structure of AlO_4^- due to the binding of M^+ to the zeolite framework, is significantly smaller. The calculated P_Q values for the optimized bare framework model with the added M^+ cations located in the same positions as in the corresponding cationic sites are significantly smaller (Table 6 and Figure 50). They are close to the P_Q value computed for the bare zeolite framework model with no cation. The P_Q values calculated for M^+ accommodated in the 6-ring are slightly larger than 3.9 MHz while those computed for M^+ located in the 8-ring are slightly smaller. This indicates that the effect of the M^+ cation on the P_Q parameters with the exclusion of the influence of the deformation of the local structure of AlO_4^- can both increase as well as decrease, depending on the M^+ position with respect to AlO_4^-, the values of the P_Q parameter of the ^{27}Al atom of the AlO_4^- tetrahedron which is compensated by the M^+ cation. In addition, our calculations employing the background charge of +1 located at the positions of M^+ reveal a negligible effect of the + charge as the calculated P_Q parameters for all the six models (Table 6) are very close to the P_Q calculated for the bare framework model without any cation. Our results indicate that the four O atoms of the $^{27}AlO_4^-$ tetrahedron shield the ^{27}Al atom and thus minimize the effect of the charge of the cation balancing the negative charge of AlO_4^-. The quadrupolar interaction decreases with the increasing diameter of the monovalent cation balancing the Al atom as the local deformation of the cationic site in the zeolite is less pronounced when accommodating a larger cation.

6.3.3 Summary

Al atoms in frameworks of hydrated zeolites exhibit a tetrahedral coordination that results in an extremely low quadrupolar broadening of the ^{27}Al NMR resonances. Extra-framework cations balancing the negative charge of framework AlO_4^- tetrahedra are solvated, mobile, and do not significantly perturb the structure of the AlO_4^- tetrahedra in hydrated zeolites. A dehydration of zeolites results in a coordination of extra-framework cations to O atoms of the AlO_4^- and SiO_4 tetrahedra followed by their significant deformation leading to a perturbation of the symmetry of AlO_4^- tetrahedron, and therefore, significant broadening of the ^{27}Al NMR signal. The effect of the cation binding consists of two contributions: (i) the deformation of the local structure of AlO_4^- due to the binding of M^+ to the zeolite framework and (ii) the effect of the M^+ cation with the exclusion of the influence of the deformation of the local structure of AlO_4^-. Our results show that the former is responsible for the broadening of the ^{27}Al NMR signals. The quadrupolar interaction decreases with the increasing diameter of the monovalent cation balancing the AlO_4^- tetrahedron as the deformation is less pronounced for larger cations.

The influence of water in hydrated zeolites is limited only to the prevention of strong coordination of the M^+ cation to O atoms of the AlO_4^- tetrahedra but there is no "averaging" effect concerning the local electrostatic field due to a molecular motion of water molecules. Our results show that the ^{27}Al NMR parameters in dehydrated zeolites can be calculated accurately enough to permit the description of the local structure of AlO_4^- tetrahedra in dehydrated zeolites. Moreover, the ^{27}Al NMR parameters can provide information regarding the cation siting in extra-framework positions and the local structure of cationic sites.

7 Conclusions

Presented work demonstrates application of solid-state NMR spectroscopy supported by quantum chemical calculations for analysis of extra-framework sites in zeolites. Quantitative distribution of lithium and sodium cations in crystallographically non-equivalent sites in dehydrated Na- and Li-FER zeolites was determined by combination of advanced techniques of ssNMR. To distinguish crystallographically non-equivalent lithium sites in a narrow range of chemical shifts, a two-dimensional ^{7}Li-^{7}Li correlation EXSY NMR experiment was successfully implemented. Quantitative distribution was subsequently determined by deconvolution of one-dimensional ^{7}Li MAS NMR spectra. Periodic DFT calculations allowed interpretation of most of the individual lithium resonances. It was found that Li^+ balancing Al in one T site can occupy two different crystallographic positions. On the other hand, assignment of close resonances has to be performed very carefully but still resonances T3 and T4 cannot be distinguished. Sound agreement between results of Li^+ and Al siting opens possibility to use Li^+ as an additional probe of Al siting.

To obtain NMR parameters of broad and overlapping sodium signals in dehydrated Na-FER samples, simultaneous analytical simulation of the ^{23}Na MAS and ^{23}Na MQMAS NMR spectra measured on two different magnetic fields (high and ultra-high) had to be performed. Theoretical calculations revealed that NMR parameters of sodium cations balancing Al in different T sites while located in the same ring are similar. Thus, Na^+ is not a suitable probe of Al siting in the case of ferrierite, yet ^{23}Na ssNMR can provide information about location of sodium in different rings.

It was shown, that both lithium and sodium ssNMR provide useful information about distribution of extra-framework cations. On the other hand, various cationic sites in silicon-rich zeolites have the same chemical environment, so the difference between NMR interaction tensors is only due to the subtle changes of bond lengths and angles. Therefore, some positions would not have been distinguished without analysis of Al siting in the framework. It demonstrates importance of multinuclear approach and thorough analysis of both Al and cation siting for characterization of zeolite catalyst.

Reliability of quantum chemical calculations in predicting structure of extra-framework sites in zeolites has been verified. Calculated NMR parameters are in good agreement with experimental values and allow interpretation of NMR spectra. We suppose that theoretical calculation can be utilized for predicting of cations NMR inactive or difficult to measure (e.g. Cu^+, Fe^{3+}).

To test possibility of indirect characterization of siting of monovalent cations, ^{27}Al MAS and MQMAS NMR spectra of hydrated and dehydrated Li-, Na- and K-CHA samples were recorded. Upon dehydration of the samples, marked broadening of ^{27}Al MAS NMR spectra was observed. Broadening caused by quadrupolar interaction increased with decreasing ionic radius. Sound agreement between experiment and calculations revealed that observed quadrupolar broadening is rather due to the deformation of AlO_4^- tetrahedron by coordination of cation, than due to the effect of positive charge of the cation. Moreover, NMR invisible potassium cation can be identified in ^{27}Al MAS NMR spectrum of dehydrated CHA by Al resonance with magnitude of quadrupolar interaction of about 3 MHz.

8 References

(1) Davis, S.; Inoguchi, Y. *Chemical Economics Handbook, Report, Zeolites*; SRI Consulting: Colorado, 2009.

(2) Csicsery, S. M. Shape-selective catalysis in zeolites. *Zeolites* **1984,** *4* (3), 202.

(3) Vermeiren, W.; Gilson, J. P. Impact of Zeolites on the Petroleum and Petrochemical Industry. *Topics in Catalysis* **2009,** *52* (9), 1131.

(4) Dědeček, J.; Sobalík, Z.; Wichterlová, B. Siting and Distribution of Framework Aluminium Atoms in Silicon-Rich Zeolites and Impact on Catalysis. *Catalysis Reviews* **2012,** *54* (2), 135.

(5) Vogt, E. T. C.; Weckhuysen, B. M. Fluid catalytic cracking: recent developments on the grand old lady of zeolite catalysis. *Chemical Society Reviews* **2015,** *44* (20), 7342.

(6) Olsbye, U.; Svelle, S.; Lillerud, K. P.; Wei, Z. H.; Chen, Y. Y.; Li, J. F.; Wang, J. G.; Fan, W. B. The formation and degradation of active species during methanol conversion over protonated zeotype catalysts. *Chemical Society Reviews* **2015,** *44* (20), 7155.

(7) Primo, A.; Garcia, H. Zeolites as catalysts in oil refining. *Chemical Society Reviews* **2014,** *43* (22), 7548.

(8) Olsbye, U.; Svelle, S.; Bjørgen, M.; Beato, P.; Janssens, T. V. W.; Joensen, F.; Bordiga, S.; Lillerud, K. P. Conversion of Methanol to Hydrocarbons: How Zeolite Cavity and Pore Size Controls Product Selectivity. **2012,** *51* (24), 5810.

(9) Perego, C.; Carati, A.; Ingallina, P.; Mantegazza, M. A.; Bellussi, G. Production of titanium containing molecular sieves and their application in catalysis. *Applied Catalysis A: General* **2001,** *221*, 63.

(10) Xia, C.; Peng, X.; Zhang, Y.; Wang, B.; Lin, M.; Zhu, B.; Luo, Y.; Shu, X. In *Green Chemical Processing and Synthesis*, 2017, DOI:10.5772/intechopen.68389 10.5772/intechopen.68389.

(11) Pirutko, L. V.; Chernyavsky, V. S.; Uriarte, A. K.; Panov, G. I. Oxidation of benzene to phenol by nitrous oxide: Activity of iron in zeolite matrices of various composition. *Applied Catalysis A: General* **2002,** *227* (1), 143.

(12) Panov, G. I.; Kharitonov, A. S.; Sobolev, V. I. Oxidative hydroxylation using dinitrogen monoxide: a possible route for organic synthesis over zeolites. *Applied Catalysis A: General* **1993,** *98* (1), 1.

(13) Skalska, K.; Miller, J. S.; Ledakowicz, S. Trends in NOx abatement: A review. *Science of The Total Environment 408* (19), 3976.

(14) Pérez-Ramírez, J.; Kapteijn, F.; Schöffel, K.; Moulijn, J. A. Formation and control of N2O in nitric acid production: Where do we stand today? *Applied Catalysis B: Environmental* **2003,** *44* (2), 117.

(15) Beale, A. M.; Gao, F.; Lezcano-Gonzalez, I.; Peden, C. H. F.; Szanyi, J. Recent advances in automotive catalysis for NOx emission control by small-pore microporous materials. *Chemical Society Reviews* **2015,** *44* (20), 7371.

(16) Espeel In *Catalysis and zeolites*; Weitkamp;Puppe, Eds.; Springer: Berlin, 1999.

(17) Corma, A.; García, H. Lewis Acids: From Conventional Homogeneous to Green Homogeneous and Heterogeneous Catalysis. *Chemical Reviews* **2003,** *103* (11), 4307.

(18) Ennaert, T.; Van Aelst, J.; Dijkmans, J.; De Clercq, R.; Schutyser, W.; Dusselier, M.; Verboekend, D.; Sels, B. F. Potential and challenges of zeolite chemistry in the catalytic conversion of biomass. *Chemical Society Reviews* **2016,** *45* (3), 584.

(19) Tang, P.; Zhu, Q.; Wu, Z.; Ma, D. Methane activation: the past and future. *Energy & Environmental Science* **2014,** *7* (8), 2580.

(20) Sakakura, T.; Choi, J.-C.; Yasuda, H. Transformation of Carbon Dioxide. *Chemical Reviews* **2007,** *107* (6), 2365.

(21) Lim, K. H.; Grey, C. P. Characterization of Extra-Framework Cation Positions in Zeolites NaX and NaY with Very Fast 23Na MAS and Multiple Quantum MAS NMR Spectroscopy. *Journal of the American Chemical Society* **2000,** *122* (40), 9768.

(22) Mortier, W. J.; Butterworths: Guildford, 1982.

(23) Olson, D. H.; Khosrovani, N.; Peters, A. W.; Toby, B. H. Crystal Structure of Dehydrated CsZSM-5 (5.8Al): Evidence for Nonrandom Aluminum Distribution. *The Journal of Physical Chemistry B* **2000,** *104* (20), 4844.

(24) Mentzen, B. F. Crystallographic Determination of the Positions of the Monovalent H, Li, Na, K, Rb, and Tl Cations in Fully Dehydrated MFI Type Zeolites. *The Journal of Physical Chemistry C* **2007,** *111* (51), 18932.

(25) Dalconi, M. C.; Alberti, A.; Cruciani, G.; Ciambelli, P.; Fonda, E. Siting and coordination of cobalt in ferrierite: XRD and EXAFS studies at different Co loadings. *Microporous and Mesoporous Materials* **2003,** *62* (3), 191.

(26) Dalconi, M. C.; Cruciani, G.; Alberti, A.; Ciambelli, P.; Rapacciuolo, M. T. Ni2+ ion sites in hydrated and dehydrated forms of Ni-exchanged zeolite ferrierite. *Microporous and Mesoporous Materials* **2000,** *39* (3), 423.

(27) Kim, C. W.; Heo, N. H.; Seff, K. Framework Sites Preferred by Aluminum in Zeolite ZSM-5. Structure of a Fully Dehydrated, Fully Cs+-Exchanged ZSM-5 Crystal (MFI, Si/Al = 24). *The Journal of Physical Chemistry C* **2011,** *115* (50), 24823.

(28) Dědeček, J.; Kaucký, D.; Wichterlová, B. Co2+ ion siting in pentasil-containing zeolites, part 3.: Co2+ ion sites and their occupation in ZSM-5: a VIS diffuse reflectance spectroscopy study. *Microporous and Mesoporous Materials* **2000,** *35 - 36*, 483.

(29) Kaucký, D.; Dědeček, J.; Wichterlová, B. Co2+ ion siting in pentasil-containing zeolites: II. Co2+ ion sites and their occupation in ferrierite. A VIS diffuse reflectance spectroscopy study. *Microporous and Mesoporous Materials* **1999,** *31*, 75.

(30) Nachtigall, P.; Delgado, M. R.; Nachtigallova, D.; Arean, C. O. The nature of cationic adsorption sites in alkaline zeolites—single, dual and multiple cation sites. *Physical Chemistry Chemical Physics* **2012,** *14* (5), 1552.

(31) Depmeier, W. In *Molecular Sieves: Science and Technology*; Karge, H. G.;Wietkamp, J., Eds.; Springer-Verlag: Berlin, 2001; Vol. 2.

(32) Petrovic, I.; Navrotsky, A.; Davis, M. E.; Zones, S. I. Thermochemical study of the stability of frameworks in high silica zeolites. *Chemistry of Materials* **1993,** *5* (12), 1805.

(33) Yoshikawa, M.; Wagner, P.; Lovallo, M.; Tsuji, K.; Takewaki, T.; Chen, C.-Y.; Beck, L. W.; Jones, C.; Tsapatsis, M.; Zones, S. I.et al. Synthesis, Characterization, and Structure Solution of CIT-5, a New, High-Silica, Extra-Large-Pore Molecular Sieve. *The Journal of Physical Chemistry B* **1998,** *102* (37), 7139.

(34) McCusker, L. B.; Grosse-Kunstleve, R. W.; Baerlocher, C.; Yoshikawa, M.; Davis, M. E. Synthesis optimization and structure analysis of the zincosilicate molecular sieve VPI-9. *Microporous Materials* **1996,** *6* (5â€“6), 295.

(35) Weitkamp, J. Zeolites and catalysis. *Solid State Ionics* **2000,** *131* (1â€“2), 175.

(36) Baerlocher, C.; McCusker, L. B.

(37) Vaughan, P. A. The crystal structure of the zeolite ferrierite. **1966,** *21* (6), 983.

(38) Loewenstein, W. The distribution of aluminum in the tetrahedra of silicates and aluminates. *American Mineralogist* **1954,** *39*, 92.

(39) Sklenak, S.; Dedecek, J.; Li, C. B.; Wichterlova, B.; Gabova, V.; Sierka, M.; Sauer, J. Aluminum siting in silicon-rich zeolite frameworks: A combined high-resolution Al-27 NMR spectroscopy and quantum mechanics/molecular mechanics study of ZSM-5. *Angewandte Chemie-International Edition* **2007,** *46* (38), 7286.

(40) Sklenak, S.; Dedecek, J.; Li, C.; Wichterlova, B.; Gabova, V.; Sierka, M.; Sauer, J. Aluminium siting in the ZSM-5 framework by combination of high resolution 27Al NMR and DFT/MM calculations. *Physical Chemistry Chemical Physics* **2009,** *11* (8), 1237.

(41) Pinar, A. B.; Márquez-Álvarez, C.; Grande-Casas, M.; Pérez-Pariente, J. Template-controlled acidity and catalytic activity of ferrierite crystals. *Journal of Catalysis* **2009,** *263* (2), 258.

(42) Pinar, A. B.; Verel, R.; Pérez-Pariente, J.; van Bokhoven, J. A. Direct evidence of the effect of synthesis conditions on aluminum siting in zeolite ferrierite: A 27Al MQ MAS NMR study. *Microporous and Mesoporous Materials* **2014,** *193*, 111.

(43) Dědeček, J.; Čapek, L.; Wichterlová, B. Nature of active sites in decane-SCR-NOx and NO decomposition over Cu-ZSM-5 zeolites. *Applied Catalysis A: General* **2006,** *307* (1), 156.

(44) Sklenak, S.; Andrikopoulos, P. C.; Boekfa, B.; Jansang, B.; Nováková, J.; Benco, L.; Bucko, T.; Hafner, J.; Dědeček, J.; Sobalík, Z. N2O decomposition over Fe-zeolites: Structure of the active sites and the origin of the distinct reactivity of Fe-ferrierite, Fe-ZSM-5, and Fe-beta. A combined periodic DFT and multispectral study. *Journal of Catalysis 272* (2), 262.

(45) Hunger, M. In *Zeolite Characterization and Catalysis: A Tutorial*; Chester, A. W.;Derouane, E. G., Eds.; Springer Netherlands: Dordrecht, 2009, DOI:10.1007/978-1-4020-9678-5_2 10.1007/978-1-4020-9678-5_2.

(46) Harris, R. K. *Nuclear magnetic resonance spectroscopy*; Longman: Essen, 1986.

(47) Slichter, C. P. *Principles of magnetic resonance*; Springer-Verlag: Berlin, Heidelberg, 1996.

(48) Freeman, R. *Nuclear magnetic resonance*; Longman: Essen, 1997.

(49) Andrew, E. R.; Bradbury, A.; Eades, R. G. NUCLEAR MAGNETIC RESONANCE SPECTRA FROM A CRYSTAL ROTATED AT HIGH SPEED. *Nature* **1958,** *182* (4650), 1659.

(50) MacKenzie, K. J. D.; Smith, M. E. *Multinuclear Solid-State NMR of Inorganic Materials*; Pergamon, 2002.

(51) Nelson, J. H. *Nuclear Magnetic Resonance Spectroscopy*; Prentice Hall, 2003.

(52) Mehring, M. *Principles of high-resolution NMR in solids*; Springer: Berlin, 1983.

(53) Haeberlen, U. *High Resolution NMR in Solids Selective Averaging: Supplement 1 Advances in Magnetic Resonance*; Elsevier Science, 2012.

(54) Duer, M. J. *Solid State NMR Spectroscopy: Principles and Applications*; Wiley, 2008.

(55) Cowan, B. *Nuclear Magnetic Resonance and Relaxation*; Cambridge University Press, 2005.

(56) Hahn, E. L. Spin Echoes. *Physical Review* **1950,** *80* (4), 580.

(57) Frydman, L.; Harwood, J. S. Isotropic Spectra of Half-Integer Quadrupolar Spins from Bidimensional Magic-Angle Spinning NMR. *Journal of the American Chemical Society* **1995,** *117* (19), 5367.

(58) Medek, A.; Harwood, J. S.; Frydman, L. Multiple-Quantum Magic-Angle Spinning NMR: A New Method for the Study of Quadrupolar Nuclei in Solids. *Journal of the American Chemical Society* **1995,** *117* (51), 12779.

(59) Amoureux, J.-P.; Fernandez, C.; Steuernagel, S. ZFiltering in MQMAS NMR. *Journal of Magnetic Resonance, Series A* **1996,** *123* (1), 116.

(60) Rocha, J.; Morais, C. M.; Fernandez, C. In *New Techniques in Solid-State Nmr*; Klinowski, J., Ed., 2005; Vol. 246.

(61) Massiot, D.; Fayon, F.; Capron, M.; King, I.; Le Calvé, S.; Alonso, B.; Durand, J.-O.; Bujoli, B.; Gan, Z.; Hoatson, G. Modelling one- and two-dimensional solid-state NMR spectra. **2002,** *40* (1), 70.

(62) Bak, M.; Rasmussen, J. T.; Nielsen, N. C. SIMPSON: A general simulation program for solid-state NMR spectroscopy. *Journal of Magnetic Resonance* **2011,** *213* (2), 366.

(63) Clark Stewart, J.; Segall Matthew, D.; Pickard Chris, J.; Hasnip Phil, J.; Probert Matt, I. J.; Refson, K.; Payne Mike, C. In *Zeitschrift für Kristallographie - Crystalline Materials*, 2005; Vol. 220.

(64) Bonhomme, C.; Gervais, C.; Babonneau, F.; Coelho, C.; Pourpoint, F.; Azaïs, T.; Ashbrook, S. E.; Griffin, J. M.; Yates, J. R.; Mauri, F.et al. First-Principles Calculation of NMR Parameters Using the Gauge Including Projector Augmented Wave Method: A Chemist's Point of View. *Chemical Reviews* **2012,** *112* (11), 5733.

(65) Engelhardt, G. In *Studies in surface science and catalysis*; Van Bekkum, H.;Flanigen, E. M.;Jacobs, P. A.;Jansen, J. C., Eds.; Elsevier: Amsterdam, 2001; Vol. 137.

(66) Rocha, J.; Carr, S. W.; Klinowski, J. AL-27 QUADRUPOLE NUTATION AND H-1-AL-27 CROSS-POLARIZATION SOLID-STATE NMR-STUDIES OF ULTRASTABLE ZEOLITE-Y WITH FAST MAGIC-ANGLE SPINNING. *Chemical Physics Letters* **1991,** *187* (4), 401.

(67) Sklenak, S.; Dedecek, J.; Li, C. B.; Gao, F.; Jansang, B.; Boekfa, B.; Wichterlova, B.; Sauer, J. ALUMINUM SITING IN THE ZSM-22 AND THETA-1 ZEOLITES REVISITED: A QM/MM STUDY. *Collection of Czechoslovak Chemical Communications* **2008,** *73* (6-7), 909.

(68) Dědeček, J.; Sklenak, S.; Li, C.; Wichterlová, B.; Gábová, V.; Brus, J.; Sierka, M.; Sauer, J. Effect of Al−Si−Al and Al−Si−Si−Al Pairs in the ZSM-5 Zeolite Framework on the 27Al NMR Spectra. A Combined High-Resolution 27Al NMR and DFT/MM Study. *The Journal of Physical Chemistry C* **2009,** *113* (4), 1447.

(69) Pyykko, P. Spectroscopic nuclear quadrupole moments. *Molecular Physics* **2001,** *99* (19), 1617.

(70) Hunger, M.; Engelhardt, G.; Koller, H.; Weitkamp, J. CHARACTERIZATION OF SODIUM-CATIONS IN DEHYDRATED FAUJASITES AND ZEOLITE EMT BY NA-23 DOR, 2D-NUTATION, AND MAS NMR. *Solid State Nuclear Magnetic Resonance* **1993,** *2* (3), 111.

(71) Feuerstein, M.; Hunger, M.; Engelhardt, G.; Amoureux, J. P. Characterisation of sodium cations in dehydrated zeolite NaX by Na-23 NMR spectroscopy. *Solid State Nuclear Magnetic Resonance* **1996,** *7* (2), 95.

(72) Ganapathy, S.; Das, T. K.; Vetrivel, R.; Ray, S. S.; Sen, T.; Sivasanker, S.; Delevoye, L.; Fernandez, C.; Amoureux, J. P. Anisotropic Chemical Shielding, M-Site Ordering, and Characterization of Extraframework Cations in ETS-10 Studied through MAS/MQ-MAS NMR and Molecular Modeling Techniques. *Journal of the American Chemical Society* **1998,** *120* (19), 4752.

(73) Hunger, M.; Sarv, P.; Samoson, A. Two-dimensional triple-quantum Na-23 MAS NMR spectroscopy of sodium cations in dehydrated zeolites. *Solid State Nuclear Magnetic Resonance* **1997,** *9* (2-4), 115.

(74) Caldarelli, S.; Buchholz, A.; Hunger, M. Investigation of Sodium Cations in Dehydrated Zeolites LSX, X, and Y by 23Na Off-Resonance RIACT Triple-Quantum and High-Speed MAS NMR Spectroscopy. *Journal of the American Chemical Society* **2001,** *123* (29), 7118.

(75) Dedecek, J.; Lucero, M. J.; Li, C.; Gao, F.; Klein, P.; Urbanova, M.; Tvaruzkova, Z.; Sazama, P.; Sklenak, S. Complex Analysis of the Aluminum Siting in the Framework of Silicon-Rich Zeolites. A Case Study on Ferrierites. *Journal of Physical Chemistry C* **2011,** *115* (22), 11056.

(76) Dedecek, J.; Wichterlova, B.; Kubat, P. Siting of the Cu+ ions in dehydrated ion exchanged synthetic and natural chabasites: a Cu+ photoluminescence study. *Microporous and Mesoporous Materials* **1999,** *32* (1-2), 63.

(77) Gee, B.; Janssen, M.; Eckert, H. Local cation environments in mixed alkali silicate glasses studied by multinuclear single and double resonance magic-angle spinning NMR. *Journal of Non-Crystalline Solids* **1997,** *215* (1), 41.

(78) Klein, P.; Dedecek, J.; Thomas, H. M.; Whittleton, S. R.; Pashkova, V.; Brus, J.; Kobera, L.; Sklenak, S. NMR crystallography of monovalent cations in inorganic matrixes: Li+ siting and the local structure of Li+ sites in ferrierites. *Chemical Communications* **2015,** *51* (43), 8962.

(79) Klein, P.; Pashkova, V.; Thomas, H. M.; Whittleton, S. R.; Brus, J.; Kobera, L.; Dedecek, J.; Sklenak, S. Local Structure of Cationic Sites in Dehydrated Zeolites Inferred from 27Al Magic-Angle Spinning NMR and Density Functional Theory Calculations. A Study on Li-, Na-, and K-Chabazite. *The Journal of Physical Chemistry C* **2016,** *120* (26), 14216.

(80) Ernst, H.; Freude, D.; Wolf, I. MULTINUCLEAR SOLID-STATE NMR-STUDIES OF BRONSTED SITES IN ZEOLITES. *Chemical Physics Letters* **1993,** *212* (6), 588.

(81) Freude, D.; Ernst, H.; Wolf, I. SOLID-STATE NUCLEAR-MAGNETIC-RESONANCE STUDIES OF ACID SITES IN ZEOLITES. *Solid State Nuclear Magnetic Resonance* **1994,** *3* (5), 271.

(82) Jiao, J.; Altwasser, S.; Wang, W.; Weitkamp, J.; Hunger, M. State of aluminum in dealuminated, nonhydrated zeolites Y investigated by multinuclear solid-state NMR spectroscopy. *Journal of Physical Chemistry B* **2004,** *108* (38), 14305.

(83) Jiao, J.; Kanellopoulos, J.; Wang, W.; Ray, S. S.; Foerster, H.; Freude, D.; Hunger, M. Characterization of framework and extra-framework aluminum species in non-hydrated zeolites Y by Al-27 spin-echo, high-speed MAS, and MQMAS NMR spectroscopy at B-0=9.4 to 17.6 T. *Physical Chemistry Chemical Physics* **2005,** *7* (17), 3221.

9 List of Published Works

Publications related to the subject of dissertation:

Dedecek, J., Lucero, M. J., Li, C., Gao, F., Klein, P., Urbanova, M., Tvaruzkova, Z., Sazama, P., Sklenak, S. Complex Analysis of the Aluminum Siting in the Framework of Silicon-Rich Zeolites. A Case Study on Ferrierites. *Journal of Physical Chemistry C,* 2011, 115, 22, 11056-11064.

Klein P., Dedecek J., Thomas H.M., Whittleton S.R., Pashkova V., Brus J., Kobera L., Sklenak S., NMR crystallography of monovalent cations in inorganic matrixes: Li+ siting and the local structure of Li+ sites in ferrierites, *Chemical Communications*, 51 (43), 8962-8965, 2015

Klein P., Pashkova V., Thomas H.M., Whittleton S.R., Brus J., Kobera L., Dedecek J., Sklenak S., Local Structure of Cationic Sites in Dehydrated Zeolites Inferred from ^{27}Al Magic-Angle Spinning NMR and Density Functional Theory Calculations. A Study on Li-, Na-, and K-Chabazite, *Journal of Physical Chemistry C*, 120, 26, 14216–14225, 2016

Further publications:

Synthesis of ZSM-5 Zeolites with Defined Distribution of Al Atoms in the Framework and Multinuclear MAS NMR Analysis of the Control of Al Distribution, Jiri Dedecek, Vendula Balgová, Veronika Pashkova, Petr Klein, Blanka Wichterlová,
Chemistry of Materials 24 (16), 3231-3239, 2012

Alkali-bonded ceramics with hierarchical tailored porosity, E. Landi, V. Medri, E. Papa, J. Dedecek, P. Klein, P. Benito, A. Vaccari,
Applied Clay Science 73, 56-64, 2013

Acid and redox activity of template-free Al-rich H-BEA* and Fe-BEA* zeolites, Petr Sazama, Blanka Wichterlová, Štěpán Sklenák, Vasile I. Parvulescu, Natalia Candu, Galina Sádovská, Jiří Dědeček, Petr Klein, Veronika Pashkova, Petr Šťastný,
Journal of Catalysis, 318, 22-33, 2014

Biaxial Q-shearing of 27 Al 3QMAS NMR spectra: Insight into the structural disorder of framework aluminosilicates, L. Kobera, J. Brus, P. Klein, J. Dedecek, M. Urbanova, *Solid state nuclear magnetic resonance* 57, 29-38, 2014

Tailoring of the structure of Fe-cationic species in Fe-ZSM-5 by distribution of Al atoms in the framework for N2O decomposition and NH 3-SCR-NOx, Petr Sazama, Blanka Wichterlová, Edyta Tábor, Petr Šťastný, Naveen K Sathu, Zdeněk Sobalík, Jiří Dědeček, Štěpán Sklenák, Petr Klein, Alena Vondrová,
Journal of Catalysis 312, 123-138, 2014

Incorporation of Al at ZSM-5 in hydrothermal synthesis. Tuning of Al pairs in the framework, V. Pashkova, P. Klein, J. Dedecek, V. Tokarová, B. Wichterlová, *Microporous and Mesoporous Materials*, 202, 138-146, 2015

Structure of Framework Aluminum Lewis Sites and Perturbed Aluminum Atoms in Zeolites as Determined by 27Al 1H REDOR (3Q) MAS NMR Spectroscopy and DFT/Molecular Mechanics, Jiří Brus, Libor Kobera, Wolfgang Schoefberger, Martina Urbanová, Petr Klein, Petr Sazama, Edyta Tabor, Stepan Sklenak, Anna V Fishchuk, Jiří Dědeček, *Angewandte Chemie International Edition*, 54 (2), 541-545, 2015

Al-rich beta zeolites. Distribution of Al atoms in the framework and related protonic and metal-ion species, P Sazama, E Tabor, P Klein, B Wichterlova, S Sklenak, L Mokrzycki, V Pashkova, M Ogura, J Dedecek
Journal of Catalysis 333, 102-114

Location of Framework Al Atoms in the Channels of ZSM-5: Effect of the (Hydrothermal) Synthesis
V Pashkova, S Sklenak, P Klein, M Urbanova, J Dědeček
Chemistry–A European Journal 22 (12), 3937-3941

Remarkably enhanced density and specific activity of active sites in Al-rich Cu-, Fe-and Co-beta zeolites for selective catalytic reduction of NOx
P Sazama, R Pilar, L Mokrzycki, A Vondrova, D Kaucky, J Plsek, Stepan Sklenak, Petr Stastny, Petr Klein
Applied Catalysis B: Environmental 189, 65-74

Superior activity of non-interacting close acidic protons in Al-rich Pt/H-*BEA zeolite in isomerization of *n*-hexane
P Sazama, D Kaucky, J Moravkova, R Pilar, P Klein, J Pastvova, E Tabor, S Sklenak, I Jakubec, L Mokrzycki
Applied Catalysis A: General 533, 28-37

TNU-9 Zeolite: Aluminum Distribution and Extra-Framework Sites of Divalent Cations, R Karcz, J Dedecek, B Supronowicz, HM Thomas, P Klein, E Tabor, P Sazama, V Pashkova, S Sklenak
Chemistry–A European Journal 23 (37), 8857-8870

Effect of Enhanced Accessibility of Acid Sites in Micromesoporous Mordenite Zeolites on Hydroisomerization of *n*-Hexane
J Pastvova, D Kaucky, J Moravkova, J Rathousky, S Sklenak, M Vorokhta, L Brabec, R Pilar, I Jakubec, E Tabor, P Klein, P Sazama
ACS Catalysis 7 (9), 5781-5795

Catalytic Properties of 3D Graphene-Like Microporous Carbons Synthesized in a Zeolite Template,P Sazama, J Pastvova, C Rizescu, A Tirsoaga, VI Parvulescu, H Garcia, L Kobera, J Seidel, J Rathousky, P Klein, I Jirka, J Moravkova, V Blechta
ACS Catalysis 8 (3), 1779-1789

10 Appendices

Appendix A: Na-FER Computational Models and Methods

Structural Models

Five models, possessing the P1 symmetry, featuring one Al/Si substitution in the framework T1a,[1] T1b,[1] T2, T3, and T4 sites[1] and one Na^+ cation compensating the corresponding negative charge of AlO_4^- were employed. The models were composed of a super cell consisting of two unit cells (Si/Al 71) along the c dimension. The starting structure of the all-silica zeolite framework (no Na^+) was downloaded from the zeolite structural database.[2] All possible symmetrically non-equivalent Na^+ sites with Na^+ ions coordinated to two oxygen atoms of one AlO_4^- tetrahedron (with the $Na\text{-}O_{Al}$ distances of some 2.4 Å) for each of the five models were used as the starting structures.

Electronic Structure Calculations

The CP2K suite of software[3] was employed using the BLYP functional,[4] GTH pseudopotentials,[5] and the TZV2P-GTH basis set. The energy cutoff of 1120 Ry was used.

Molecular Dynamics

Molecular dynamics (MD) simulations were performed as implemented in the QUICKSTEP program,[6] a part of the CP2K suite of software.[3] Born-Oppenheimer MD simulations of 3000 - 8000 fs durations were performed in the canonical ensemble, with a time step of 1.0 fs and a mean temperature of 400 K regulated using a chain of Nose-Hoover thermostats. The duration of the MD simulation depended on the number of steps needed to equilibrate the calculated system. When the calculated systems were equilibrated, the structures of ten distinct ″snapshots″ were collected from each molecular dynamics simulation and optimized. The most stable structures of all distinct Na^+ sites for all five models (i.e., Al in all the five framework T sites) were used for subsequent NMR computations.

Geometry Optimizations

The lattice parameters and the atomic positions were optimized employing conjugate-gradient algorithm minimization of energies and forces as implemented in the QUICKSTEP program,[6] a part of the CP2K suite of software.[3]

Calculations of ^{23}Na NMR Shielding

Clusters of seven coordination shells around the Al atom (Al-O-Si-O-Si-O-Si-O-H_{link}) and the Na^+ ion were extracted from the optimized structures. Due to the presence of silicate rings in the framework of ferrierite, the created seven-shell clusters contained pairs of very close H_{link} atoms. Since the close H_{link} atoms represented the same Si atom, they were replaced by the corresponding $Si(OH_{link})_2$ moiety. This was repeated until the cluster contained no such pairs. The ^{23}Na NMR shielding values were calculated by the gauge independent atomic orbital method (GIAO)[7] using Gaussian09,[8] the B3LYP functional,[4b, 9] and the pcS basis sets of Jensen;[10] pcS-4 for the Na and Al atoms and pcS-1 for all the other atoms. The calculated ^{23}Na NMR shielding values were converted to ^{23}Na chemical shifts using the calculated shielding of 568.6 ppm for $Na^+(H_2O)_6$ (^{23}Na chemical shift is 0.00 ppm by definition).[11] The geometry of $Na^+(H_2O)_6$ was optimized at B3LYP/cc-pVQZ and subsequently the ^{23}Na NMR shielding of 568.6 ppm was obtained at B3LYP/pcS-4 for the Na atom and pcS-1 for the O and H atoms.

References

[1] J. Dedecek, M. J. Lucero, C. Li, F. Gao, P. Klein, M. Urbanova, Z. Tvaruzkova, P. Sazama, S. Sklenak, *Journal of Physical Chemistry C* **2011**, *115*, 11056-11064.

[2] http://www.iza-structure.org/databases*; Space group: Immm; Cell parameters: a = 19.018 Å, b = 14.303 Å, c = 7.541 Å.*

[3] *The CP2K developers group,* http://cp2k.org/.

[4] (a) A. D. Becke, *Physical Review A* **1988**, *38*, 3098-3100; (b) C. T. Lee, W. T. Yang, R. G. Parr, *Physical Review B* **1988**, *37*, 785-789.

[5] aC. Hartwigsen, S. Goedecker, J. Hutter, *Physical Review B* **1998**, *58*, 3641-3662; bM. Krack, *Theoretical Chemistry Accounts* **2005**, *114*, 145-152.

[6] J. VandeVondele, M. Krack, F. Mohamed, M. Parrinello, T. Chassaing, J. Hutter, *Computer Physics Communications* **2005**, *167*, 103-128.

[7] K. Wolinski, J. F. Hinton, P. Pulay, *Journal of the American Chemical Society* **1990**, *112*, 8251-8260.

[8] M. J. Frisch, et al., Gaussian 09, Revision C.01, Gaussian, Inc., Wallingford CT, 2011.

[9] A. D. Becke, *Journal of Chemical Physics* **1993**, *98*, 5648-5652.

[10] F. Jensen, *Journal of Chemical Theory and Computation* **2008**, *4*, 719-727.

[11] J. Mahler, I. Persson, *Inorganic Chemistry* **2012**, *51*, 425-438.